UNIVERSITY OF CALIFORNIA SAN DIEGO

Synthesis and Self-Assembly of Polymer-Grafted Metal-Organic Frameworks

A Dissertation submitted in partial satisfaction of the requirements
for the degree Doctor of Philosophy

in

Chemistry

by

Kyle Barcus

Committee in charge:

Professor Seth M. Cohen, Chair
Professor Darren J. Lipomi
Professor Andrea R. Tao
Professor F. Akif Tezcan
Professor Haim Weizman

2024

The Dissertation of Kyle Barcus is approved, and it is acceptable in quality and form for publication on microfilm and electronically.

University of California San Diego

2024

TABLE OF CONTENTS

LIST OF FIGURES

LIST OF SCHEMES

LIST OF TABLES

ACKNOWLEDGEMENTS

First, I would like to acknowledge my advisor, Professor Seth M. Cohen, for his excellent mentorship and support throughout my graduate studies. Seth is the embodiment of efficiency. His dedication to his family, our lab, and his own aspirations and goals is so effortlessly balanced and his focus so singular that it was as inspiring as it was intimidating. He never asked more of his students than he did of himself, which would be more comforting if he wasn't able to easily write a grant in a day or edit a manuscript in an hour. His leadership was on full display when he not only became a project manager at DARPA, which is not exactly a part-time job, but did so five months before the entire country shut down due to a global pandemic. Under these conditions, a normal advisor would have had to make some tough decisions. But Seth, seemingly transcendent of any human limitations, just simply did both jobs better than most could have done either one. Then continued to do so for four entire years. It both defies explanation and defines Seth as a person. But he never took himself too seriously and truly loves his lab and his students. Working with Seth has had a profound impact on not just my own research and studies, but on how I view leadership and responsibility. Thank you Seth for such a memorable five years.

I would also like to thank my fellow lab members who helped create such an encouraging and positive lab culture. My mentor, Sergio Ayala, laid the foundation of polymer research in the lab that my projects stood up from. He was a great teacher and an even better friend. From my cohort, Mark Kalaj and Ryjul Stokes were all I could ask for from a colleague and I am forever grateful for their support and how their own excellence pushed me to achieve all that I did. Finally, I want to thank my undergraduate student, Austin Wang. He took a project almost entirely by himself from conception to publication and within a year finished his

undergraduate work with a first author publication in JACS. He has begun his own graduate research career now and I look forward to watching him grow into a successful scientist.

I especially want to thank Professor Phil Costanzo for his mentorship in my undergraduate research at California State University, San Luis Obispo. He was a significant influence in my decision to pursue graduate school and his passion for teaching and research were formative in my interest in polymer chemistry and chemical education. His trust in his students to pursue undergraduate research with minimal supervision and caring understanding helped all of us to learn from mistakes and gain confidence in our abilities and our own independence. Because of his teaching and leadership many of the students in his lab, myself included, were able to get a running start into graduate school and I attribute a significant amount of my own success to this.

I would also like to thank my close and extended family for their support and encouragement. With very few members of my family having received a college degree at all, I greatly appreciated returning home to such a grounded and happy family. In the long years of research, it is easy to become institutionalized and to forget that most of the world does not care where or how often you publish, how impressive your research is, or what you even do at all. My favorite part of coming home to family is that I was rarely if ever asked about the details of my work, only how I was doing. Home was a place I could truly relax, and I always returned to lab with the serene feeling that, no matter the time or reason, I had a place I could return to with people who would always love me unconditionally. To my parents, Christina Barcus and Brian Barcus, you were my first teachers, and the work I have accomplished here is due more to your influence than any other.

Finally, I wish to thank my amazing wife Andrea Kim for your amazing support and love throughout my time here. While I will leave this place with many gifts, my memories of you are the ones I cherish the most. Now it is my time to return the favor and support you in your studies. I love you and am so happy knowing the rest of my life will be spent with you.

Chapter 2, in part, is a reprint of the material, "Free-standing metal–organic framework (MOF) monolayers by self-assembly of polymer-grafted nanoparticles" *Chem. Sci.* **2020**, 11, 8433-8437. The dissertation author was the primary author of this manuscript and gratefully acknowledges the contributions of its coauthor Seth M. Cohen.

Chapter 3, in part, is a reprint of the material "Influence of Polymer Characteristics on the Self-Assembly of Polymer-Grafted Metal–Organic Framework Particles" *ACS Nano*. **2022**, *16*, 18168-18177. The dissertation author was the primary author of this manuscript and gratefully acknowledges the contributions of coauthors Po-An Lin, Yilong Zhou, Gaurav Arya, and Seth M. Cohen.

Chapter 4, in part, is a reprint of the material "Quantifying Ligand Binding to the Surface of Metal-Organic Frameworks" J. Am. Chem. Soc. **2023**, *145*, 16821-16827. The dissertation author was the primary author of this manuscript and gratefully acknowledges the contributions of coauthors Austin Wang and Seth M. Cohen.

VITA

Education

2017 Bachelor of Science in Biochemistry, Cal Poly San Luis Obispo

2024 Doctor of Philosophy in Chemistry, University of California San Diego

PUBLICATIONS

Kyle S. Barcus, Austin Wang, Seth M. Cohen. "Quantifying Ligand Binding to the Surface of Metal-Organic Frameworks." *J. Am. Chem. Soc.* **2023**, *145, 16821-16827*.

Kyle S. Barcus, Po-An Lin, Gaurav Arya, Seth M. Cohen. "The Influence of Polymer Characteristics on the Self-Assembly of Polymer-Grafted MOF Particles." *ACS Nano.* **2022**, *16,* 18168-18177.

Jin Yeong Kim, **Kyle S. Barcus**, Seth M. Cohen. "Controlled Two-Dimensional Alignment of Metal–Organic Frameworks in Polymer Films." *J. Am. Chem. Soc.* **2021**, *143,* 3703–3706.

Kyle S. Barcus, Seth M. Cohen. "Free-standing metal–organic framework (MOF) monolayers by self-assembly of polymer-grafted nanoparticles." *Chem. Sci.*, **2020**, *11*, 8433-8437.

Yuji Katayama, Mark Kalaj, **Kyle S. Barcus,** Seth M. Cohen "Self-Assembly of Metal–Organic Framework (MOF) Nanoparticle Monolayers and Free-Standing Multilayers." *J. Am. Chem. Soc.* **2019**, *141*, 20000-20003.

Mark Kalaj, Kyle C. Bentz, Sergio Ayala Jr., **Kyle S. Barcus**, Joey M. Palomba, Yuji Katayama, Seth M. Cohen. "MOF-Polymer Hybrid Materials: From Simple Composites to Tailored Architectures." *Chem. Rev.* **2020**, *120*, 8267–8302.

Mark Kalaj, Mohammad R. Momeni, Kyle C. Bentz, **Kyle S. Barcus**, Joseph M. Palomba, Francesco Paesani, and Seth M. Cohen. "Halogen bonding in UiO-66 frameworks promotes superior chemical warfare agent simulant degradation." *Chem. Comm.*, **2019**, *55*, 3481-3484.

ABSTRACT OF THE DISSERTATION

Synthesis and Self-Assembly of Polymer-Grafted Metal-Organic Frameworks

by

Kyle Barcus

Doctor of Philosophy in Chemistry

University of California San Diego, 2024

Professor Seth M. Cohen, Chair

Metal-organic frameworks (MOFs) are crystalline, porous materials with unique properties valued for applications in chemical storage, separation, and catalysis. While MOFs have shown great potential for these applications, a major shortcoming of these materials is their inherently crystalline nature, which limits their processability into the form factors required for these applications. To overcome this issue, MOFs have been combined with polymers in order to form composites that incorporate the flexibility and processability of

polymers while retaining the properties of the MOF material. However, incompatibilities between the MOF surface and the polymer matrix can result in defects and mechanical failure. Lowering the MOF loading to circumvent this greatly diminishes or negates the contribution of the MOF to the material properties. Therefore, a method is needed to formulate composites that allows for high MOF loading while retaining the desirable properties of the polymer.

To develop a solution to this issue, Chapter 2 describes the preparation of polymer-coated MOFs using surface-initiated controlled radical polymerization (SI-CRP) from coordinating initiators. This method allows for the preparation of single nanoparticle composites, with the polymer directly attached to the MOF surface. The resulting particles were then self-assembled into monolayers at the air-water interface that were found to be free-standing when removed from the water surface. This method was found to be generalizable to several other MOFs, providing a platform for polymer-MOF composites with intrinsically high loadings of MOF particles.

Chapter 3 systematically studies the different factors of polymer-grafted MOFs on both the particle self-assembly and the physical properties of the resulting monolayers. The effect of particle size, polymer length, and polymer composition were systematically varied. Monolayers of exceptional flexibility and toughness were found using poly(methyl acrylate). Additionally, the self-assembly of particles into ordered structures was studied both experimentally and computationally to be a result of particle size, polymer grafting density, and polymer hydrophobicity.

Chapter 4 analyzes the coordination of different ligands to the surface of MOFs. Using a fluorescent dye containing a coordinating ligand, the amount of ligand present on the MOF surface can be determined using UV-visible spectroscopy. Furthermore, the stability of this

coordination can be easily measured by analyzing the amount of dye that disassociates from the surface under various conditions. This feature was used as a diagnostic to determine the binding strength of several classes of ligands to different MOFs and provides a simple platform for the analysis of MOF surface coordination.

Chapter 1: Introduction to Metal-Organic Frameworks and Polymer Composites

1.1 Metal-Organic Frameworks

Metal-organic frameworks (MOFs) are a class of crystalline, porous coordination materials known for their high-surface area, defined pore size, and range of chemical functionality.[1-4] Comprised of inorganic secondary building units (SBUs) and multitopic organic ligands, the structure of MOFs can be finely-tuned towards a wide variety of applications including gas storage, catalysis, sensing, and drug delivery.[5-8]

The vast array of possible metal and organic ligand combinations has resulted in thousands of MOFs being reported since their initial description.[9-10] To list some examples, the prototypical ligand 1,4-benzenedicarboxylic acid (H_2bdc) when combined with a Zn(II) metal salt forms one of the first discovered MOFs termed IRMOF-1 (IRMOF = isoreticular MOF), with Zn_4O SBU connected by six ligands (Figure 1.1).[11] However, changing the metal to a Zr(IV) salt while retaining the same ligand(H_2bdc), yields UiO-66 (UiO = University of Oslo), which consists of a Zr_6O_8 SBU connected by twelve ligands (Figure 1.1).[12] These two MOFs differ not only in their connectivity, but have different physical properties as well. Whereas IRMOF-1 is unstable to atmospheric moisture and rapidly loses crystallinity, UiO-66 is highly stable in water due to its higher connectivity and the strong coordination between the Zr(IV) SBUs and the carboxylate ligand. This general concept of metal-ligand combinations forms the basis for MOF design, and by extension, variations to the ligand length and connectivity can result in new MOF structures. For example, isoreticular ('same-net') MOFs can be prepared using extended ligands with the same connectivity, such that biphenyl-4,4'-dicarboxylic acid (H_2bpdc) combined with a Zr(IV) salt forms a derivative of UiO-66 with larger pores termed UiO-67 (Figure 1.1).[12] Finally, substituting the ditopic H_2bdc with the tritopic 1,3,5-benzenetricarboxylic acid (H_3btc) forms another Zr(IV) MOF, MOF-808 (Figure 1.1).[13] These classic examples of MOFs are only a small

fraction of the structures that have been prepared to date, and a vast array of theoretically possible MOFs with unique properties remain to be synthesized.

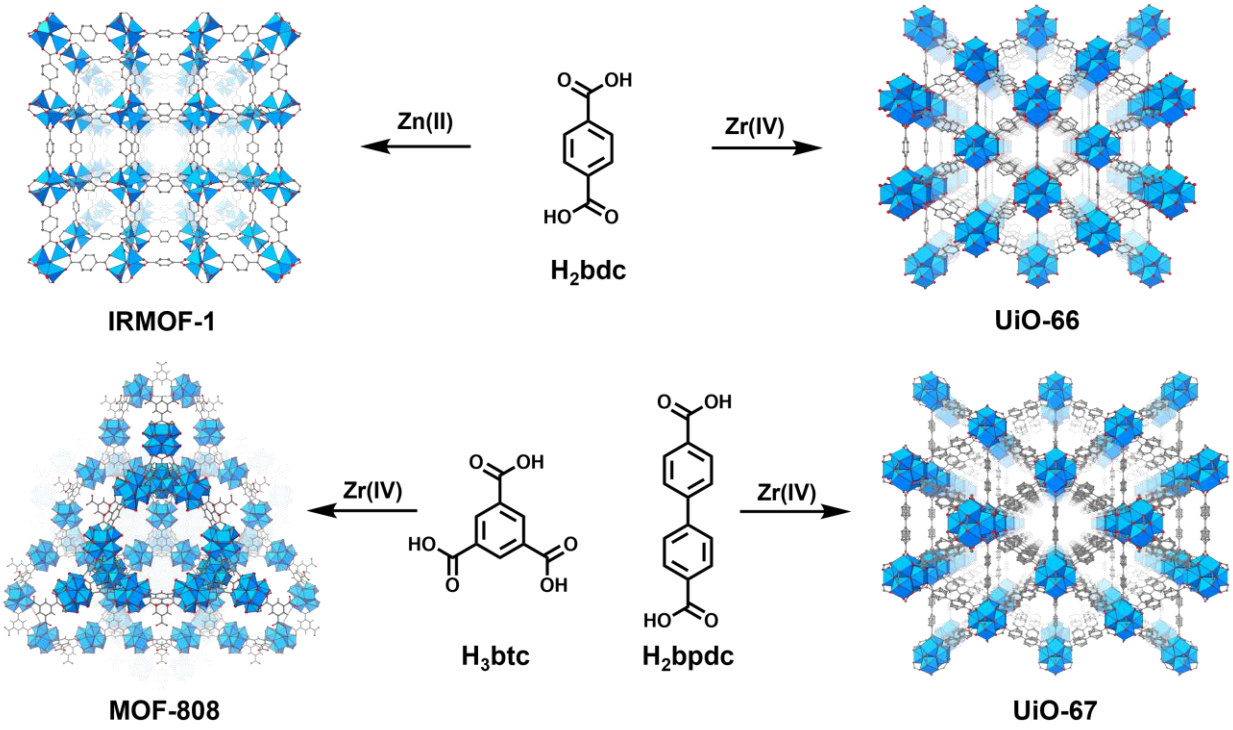

Figure 1.1. Chemical representation of MOFs as a combination of multitopic organic linkers and inorganic secondary building units (SBUs). *Top*: Structures of MOFs derived from H_2bdc with either Zn(II) or Zr(IV) SBUs to produce IRMOF-1 or UiO-66, respectively. *Bottom*: Structures of two MOFs derived from Zr(IV) SBUs. The tritopic H_3btc ligand forms MOF-808 while the extended H_2bpdc ligand forms the isoreticular expanded form of UiO-66, termed UiO-67.

The introduction of functional groups on the organic linkers of MOFs allows for further modifications of MOF physical and chemical properties. While some chemical functionalities can be introduced prior to the MOF synthesis, these are only tolerated by a limited set of MOFs while bulky or reactive groups usually preclude MOF formation entirely. Early reports from Yaghi and coworkers demonstrated that IRMOF-1 could be synthesized with H_2bdc ligands modified with amino, alkyl, and halogen functional groups (Figure 1.2).[11, 14] Encouraged by these results,

modified H_2bdc ligands were shown to be compatible with a variety of other MOFs prepared with different metal precursors such as Al(III), Fe(III), and Zr(IV).[15-17] These findings inspired the development of further modification by covalent postsynthetic modification (PSM), wherein a MOF with a reactive functional group on the linker is treated with an external reagent that undergoes covalent bond formation with the MOF ligand (Figure 1.2).[18-19] Covalent PSM was first demonstrated in extended coordination polymers similar to MOFs.[20-21] However, it was not until 2007 that Cohen and coworkers formalized the concept of 'postsynthetic modification' by demonstrating the successful modification of the amine derivative of IRMOF-1 (IRMOF-3) by the introduction of acetic anhydride to form the acetamide derivative on the MOF linker (Figure 1.2).[22] This simple and intuitive methodology resulted in a large number of further modifications to impart new properties into MOFs, such as improved aqueous stability, catalytic reactivity, and size selective permeation.[23-25] The development of PSM has been widely adopted by the field of MOF chemistry as a method to introduce functional groups incompatible with MOF synthesis conditions.[26]

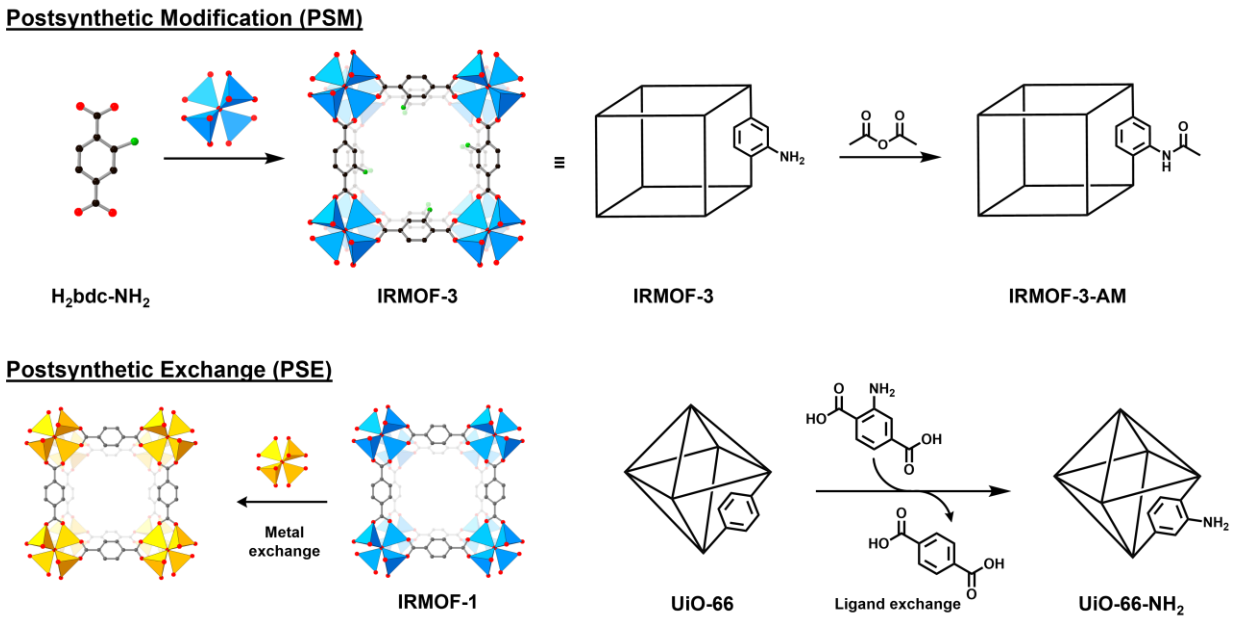

Figure 1.2. Schematic representation of postsynthetic modification (PSM) of IRMOF-3 with acetic anhydride (*top*), and postsynthetic exchange (PSE) of either the metal SBU of IRMOF-1 or the ligands of UiO-66 (*bottom*). Simplified geometric diagrams of MOF structures are shown on the right.

A comparable method to introduce new chemical functionalities in a postsynthetic manner involves the exchange of the organic linkers or metals within the structure MOF, termed postsynthetic exchange (PSE) (Figure 1.2).[27-29] The exchange of organic linkers in MOFs occurs as a result of the dynamic nature of the coordination bond of the linker and the metal SBU.[30-32] For example, the introduction of excess H_2bdc-NH_2 results in ligand exchange with the native H_2bdc ligand of MOFs IRMOF-1 and UiO-66 to form the amine version of these MOFs. Similarly, the Zn(II) ions in the metal cluster of IRMOF-1 have been partially exchanged by PSE with Ni(II) and Co(II) (Figure 1.2).[31, 33] Both PSM and PSE further expand the potential of MOFs to be modified for new applications.

Surface-Selective Postsynthetic Modification of MOFs. The postsynthetic modification of the external surfaces of MOF particles is critical to many of their potential applications,

particularly in biological applications such as drug delivery where colloidal stability is a fundamental necessity.[34-36] Modifications around the pore openings can also introduce selective uptake into the interior, leading to higher performance separations or improved stability in aqueous solutions. Due to porous structure of MOFs, it is challenging to achieve selective reactivity for interior versus exterior functional groups, and standard PSM methods are non-selective in that they generally result in homogenously distributed modification throughout the MOF. This challenge is further compounded by the lack of characterization methods available to quantitatively distinguish surface-specific chemical features from those in the interior.

The method most used to functionalize MOF surfaces with small molecules relies on coordinative PSM, taking advantage of the exposed metal sites of SBUs on the MOF surface. An early study by Kitagawa and coworkers cleverly demonstrated the validity of this method.[37] They prepared the asymmetric MOF $[Zn_2(1,4\text{-bdc})_2(dabco)]_n$ (dabco = 1,4-diazabicyclo[2.2.2]octane), which consists of two-dimensional sheets of the $Zn_2(1,4\text{-bdc})_2$ paddlewheel MOF pillared by the diamine ligand into a three-dimensional structure (Figure 1.3). As a result of this unique chemical structure, the cubic crystals have four faces terminated by carboxylate ligands while the other two are terminated by amines. By treating these crystals with a fluorescent dye containing a carboxylic acid, they observed by fluorescent microscopy that coordination of the dye was restricted to the crystal surfaces terminated by carboxylates, and no modification of the interior or amine-terminated facets occurred. Since this work, several groups have published research using coordination as a method for selective surface modification, and further advancements in this area show significant promise in advancing MOFs for many applications.[38-41]

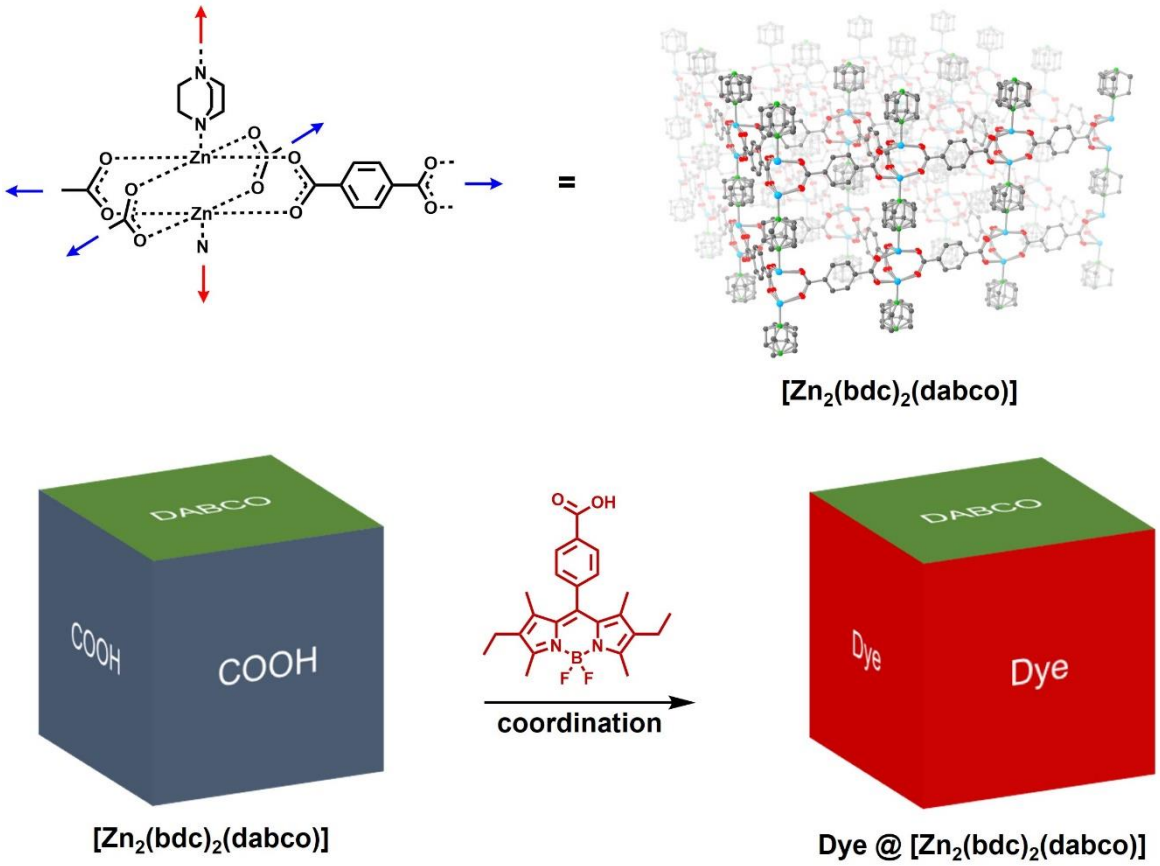

Figure 1.3. Chemical representation of the pillared-layered structure of the MOF $[Zn_2(1,4\text{-bdc})_2(dabco)]_n$ (*top*) and the selective modification of the COOH-terminated facets of the cubic crystals with a fluorescent dye (*bottom*).

1.2 Hybridization of MOFs and Polymers into Composite Materials

Significant progress has been made in the synthesis, properties, and applications of MOFs at the fundamental level. However, the inherent crystallinity of MOFs results in a powder form that poses a major challenge for the subsequent material handling and processing required for commercial implementation.[42-43] In contrast, polymeric materials are ubiquitous in modern technologies due to the simplicity of processing into various form factors (e.g., films and fibers), as well as properties such as ductility, viscoelasticity, and durability. This has led to a growing field of research to develop methodologies which combine MOFs and polymers into hybridized materials to achieve composites which display the advantageous properties of both materials.[44-45]

One of the simplest forms of these composites involves the direct mixing and dispersion of MOFs into a polymer matrix to create form factors such as hollow fibers, foams, or films known as mixed-matrix membranes (MMMs) (Figure 1.4).[46] However, incompatibility between the two phases may result in defects and low particle loading that diminish the contribution of the MOF filler to the material properties.[47-48] Several methods have been devised to improve the MOF/polymer interactions including controlling the particle size, chemical modification of the MOF surface, and covalent crosslinking of the MOF and polymer through chemical bond formation. Of these methods, the postsynthetic polymerization (PSP) of the MOF with polymers provides one route to create homogenous composites.

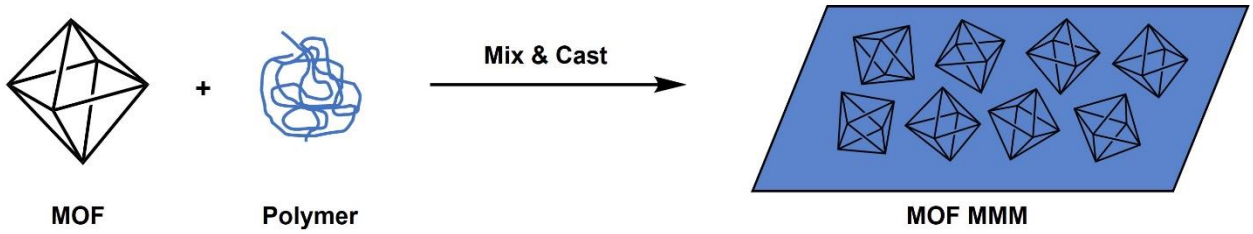

Figure 1.4. Schematic representation of MOF mixed-matrix membranes (MMMs).

Zhang et al. pioneered one of the first demonstrations of PSP through the functionalization of the reactive amine functional group on UiO-66-NH_2 to methacrylamides (UiO-66-NH-Met) (Figure 1.5a).[49] This modified MOF was mixed with the monomer butyl methacrylate and a photoinitiator before being cast into a Teflon mold. The polymerization was initiated by exposure to UV light, which incorporated the methacrylamide groups on the MOF into the growing polymer chains, thereby forming a cross-linked, standalone membrane. Surface area measurements of the membrane showed significant gas uptake, demonstrating that the MOF retained porosity and polymer had not infiltrated the pores. There has been considerable development since this seminal

work, with numerous such composites being prepared in situ via polymerization between monomers and co-functionalized MOFs.[50-52] This method affords materials with impressive separation and physical properties when compared to mixed blends of MOFs and polymers. While the copolymerization of monomers and functionalized MOFs provides a straightforward approach to highly integrated composites, the inevitable crosslinking of the polymer matrix produces a thermoset-like material that impedes further processing or purification of excess monomer and solvent. The current state-of-the-art in MOF PSP circumvents this by employing more controlled polymerization methods that are initiated from MOF surface sites, resulting in polymer coating on the surface of each individual particle.

Matzger et al. were one of the first to report this type of PSP, conducting atom-transfer radical polymerization (ATRP) from the surface of IRMOF-1.[53] Given that IRMOF-1 lacks chemical functional groups for modification, a shell of IRMOF-3 was grown around the IRMOF-1 crystals. The shell of IRMOF-3, which is isoreticular to IRMOF-1 and contains the H_2bdc-NH_2 ligand, allows for PSM. The amine present on the surface was functionalized with 2-bromoisobutyric anhydride to form the alkyl bromide initiator. With the initiator installed, ATRP of methyl methacrylate (MMA) produced a poly(methyl methacrylate) coating on the surface. Notably, the polymer could be recovered by digestion of the particles and analyzed by gel permeation chromatography (GPC), which indicated that crosslinking of the polymer chains had not occurred.

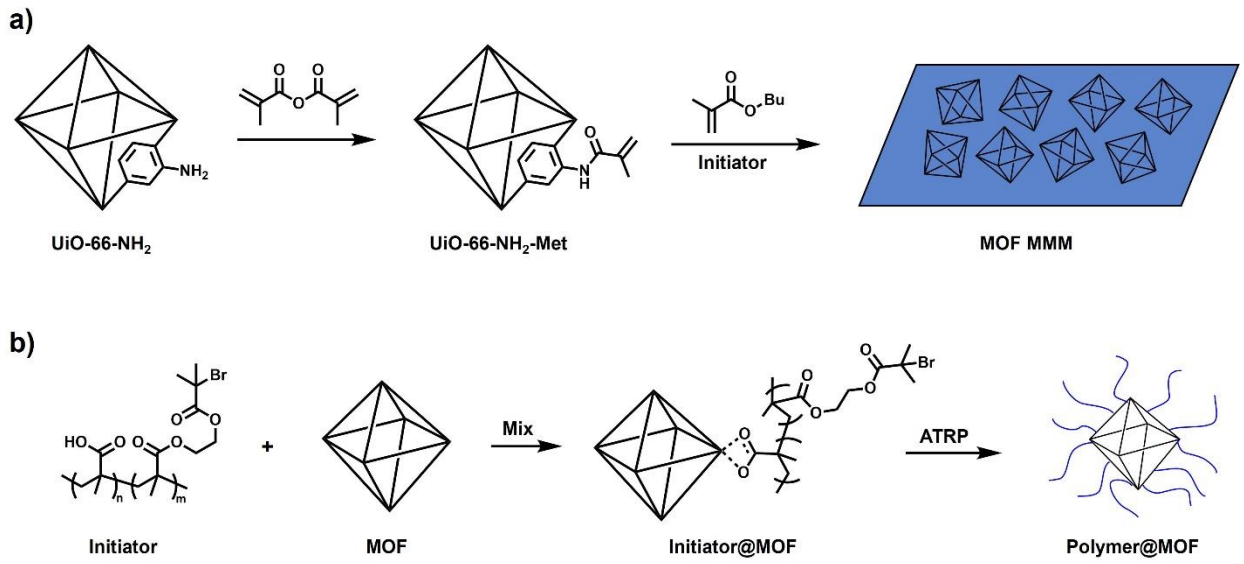

Figure 1.5. Schematic representation of two approaches for postsynthetic polymerization (PSP). a) Covalent PSM of UiO-66-NH_2 to attach monomer and copolymerization with *n*-butyl methacrylate to form crosslinked film. b) Coordinative PSM with initiator-functionalized copolymer followed by ATRP polymerization to form polymer-grafted MOF particles.

A more general strategy to attach ATRP initiators to the surface of MOFs was proposed by He et al.[54] This involved preparing a block co-polymer from the copolymerization of methacrylic acid (MAA) and a monomer containing an ATRP initiator: 2-(2-bromoisobutyryloxy) ethyl methacrylate (BIEM) (Figure 1.5b). The resultant copolymer could coordinate to the surface of MOFs via the carboxylic acid side chains of MAA, while BIEM provides initiation sites for ATRP. In this way, five distinct MOFs were coated with the polymer and ATRP was used to create several different polymer coatings including polystyrene and various polyacrylates. The significant diversity in both MOFs and polymers demonstrated in this study underscores the potential for MOF PSP to generate highly customized materials for an array of possible material applications.

1.3 Controlled Radical Polymerization and Polymer-Grafted Nanoparticles

As the research and potential applications of polymer-MOF hybrid materials has grown, it has become increasingly necessary to fabricate polymers with tailored functionalities to create more sophisticated materials. To accomplish this, the field of MOF research increasingly relies upon progress in synthetic polymer chemistry, drawing on new techniques for the development of polymers bespoke for novel applications. Highlighted in Section 1.2 was the utilization of ATRP, a form of controlled radical polymerization (CRP), to perform PSP from the surface of several MOFs. This was shown to be an effective method to prepare a well-defined polymer shell on the MOF surface while simultaneously controlling the polymer molecular weight and mitigating interparticle crosslinking. However, this approach is not novel; it was first demonstrated on silica nanoparticles almost two decades prior, almost concurrently with the initial discovery of MOFs.

Surprisingly, despite the similar impact both CRP and MOFs have had on materials chemistry since their concurrent discoveries, there remains a significant lack of overlap between these two areas of research and only a handful of studies integrating CRP and MOFs have been published. Furthermore, the field of surface-initiated controlled radical polymerization (SI-CRP) from inorganic nanoparticles is well-developed, and polymers synthesized to embody their own properties could synergistically enhance MOFs beyond their individual potential when combined.[55] To this end, CRP, and by extension SI-CRP, stands out as one of the most versatile methods for creating polymers with precise architecture and functionality for the most demanding applications.

Controlled Radical Polymerization. Fundamentally, the goal of CRP strategies is to control crucial polymer characteristics such as chain length, dispersity, and end-group fidelity. The two most popular methods used to achieve this are the aforementioned ATRP[56-58] and reversible addition-fragmentation chain transfer (RAFT)[59-61] polymerization. While mechanistically distinct,

both ATRP and RAFT rely on the introduction of a chemical species which establishes an equilibrium between dormant and active chains.[62] The equilibrium is tuned to favor the dormant state and allows only the brief, intermittent activation of dormant chains to propagating radicals. This ensures continuous and uniform growth of polymer chains and simultaneously limits termination. The difference between ATRP and RAFT is the mechanisms which govern this equilibrium and the reagents used to achieve them (Figure 1.6). The mechanism in ATRP is reversible deactivation, which harnesses a reversible redox process between a metal complex. The dormant species (typically an alkyl halide) reacts with a transition metal complex reacts with a transition metal complex (e.g., Cu(I)/ligand) to abstract the halide and generate both an active radical species and a higher oxidation state metal complex (e.g., Cu(II)/ligand). The active radical then undergoes continuous addition of monomer until deactivation by the higher oxidation state metal complex, returning the polymer chain to its dormant state. By comparison, the equilibrium established by RAFT involves degenerative transfer and relies on the use of a stable, easily transferrable group that can rapidly transition between active and dormant species (Figure 1.6). This is achieved by a chain transfer agent (CTA), typically a thiocarbonylthio (Z–C(═S)S–R) compound, which mediates the polymerization process through a series of reversible addition and fragmentation reactions.

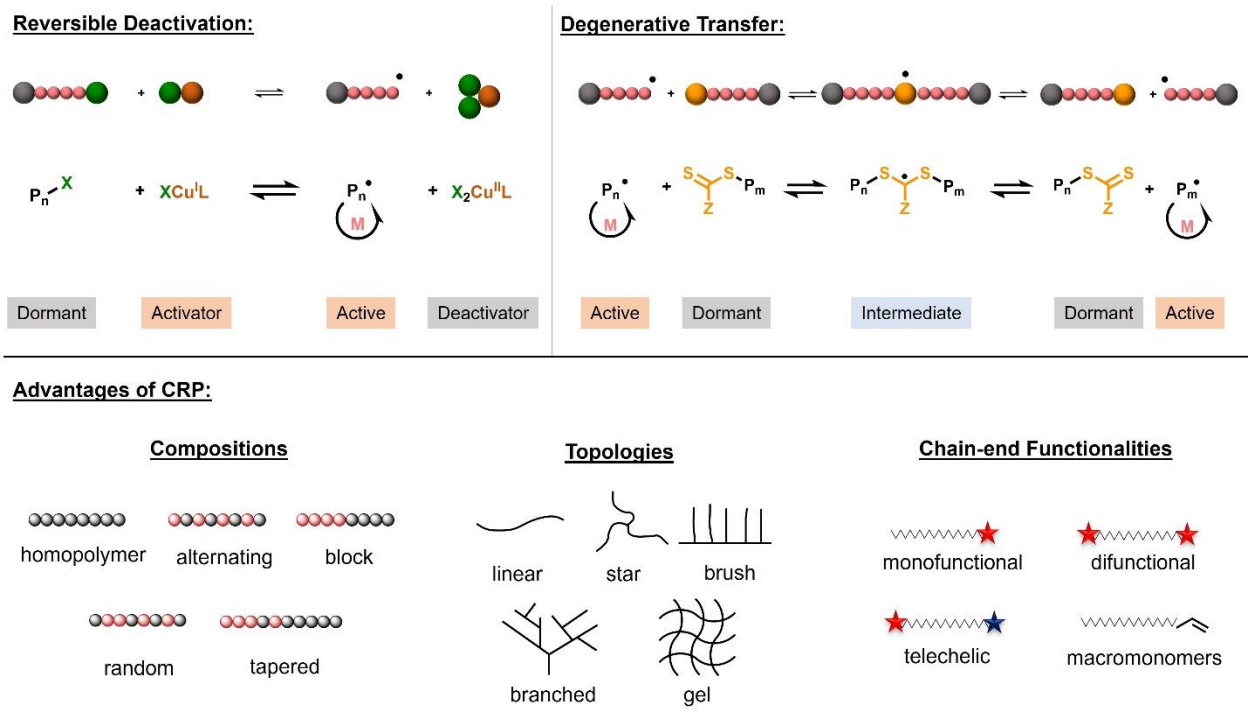

Figure 1.6. Schematic representation of the reversible equilibriums established by ATRP (reversible deactivation) and RAFT (degenerative transfer) (*top*) and the various compositions, topologies, and functionalities achievable by CRP (*bottom*).

Beyond controlling the polymer molecular weight, CRP affords polymers with chemically distinct end groups on each polymer chain (Figure 1.6). The dormant chain ends can be reactivated in the presence of another monomer to form well-defined block copolymers.[63] Furthermore, pre- or postsynthetic modification of the initiator or terminal functional groups is easily achieved using standard synthetic methods (e.g., azide-alkyne cyclization or amide coupling).[64] Finally, a variety of polymer architectures such as stars, combs, and rings can be formed which demonstrate unique macroscopic properties relative to their linear counterparts.[65]

Synthesis and Properties of Polymer-Grafted Nanoparticles. Polymer-grafted nanoparticles (PGNPs) are a class of nanostructured materials consisting of a layer of individual polymer chains tethered at one end to the particle surface. The properties of these materials are highly dependent on the conformation of the polymer shell, which is controlled by both the spatial

distribution and molecular weight of the grafted chains. As either molecular weight or grafting density increases beyond a certain ratio, steric interactions force the polymer chains to extend away from the surface giving rise to a dense polymer brush (Figure 1.7a). The curvature of the surface has a more subtle influence; since the spacing between chains decreases the further from the surface they extend, the polymer chains eventually adopt a relaxed conformation beyond a certain distance (Figure 1.7b). However, the presence of this regime can have a drastic effect on mechanical properties. Choi et al. performed mechanical testing on thin films composed entirely of PGNPs and studied the effect of increasing polymer chain length.[66] They observed an order of magnitude increase in fracture toughness once the length of polymer passed this critical radius. Electron microscopy showed that the presence of this low-density polymer regime allowed for chain entanglement to occur between neighboring particles and gave rise to energy dissipation during fracture through microscopic plastic deformation (Figure 1.7b).

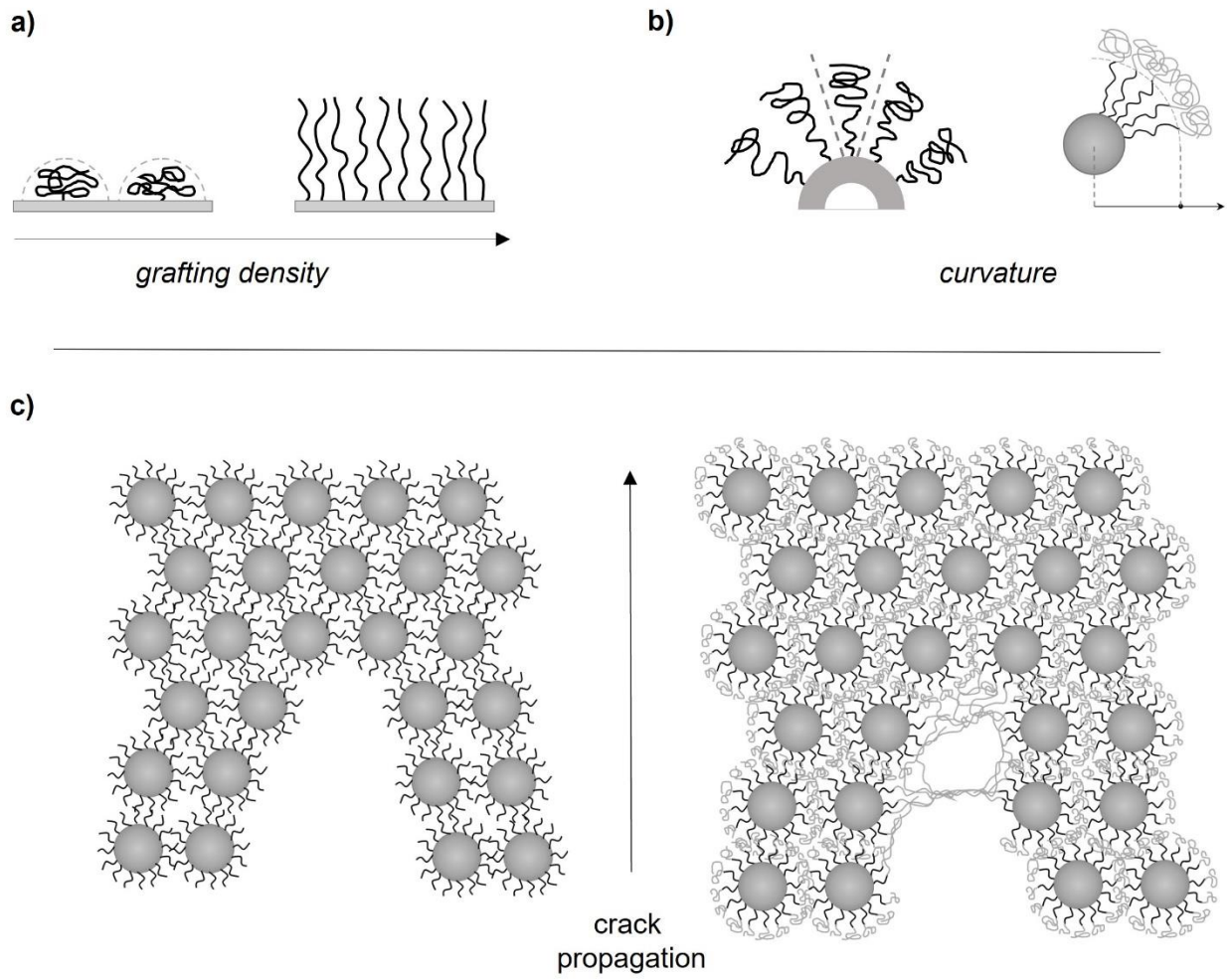

Figure 1.7. a) Polymer chains grafted on flat surface in relaxed and extended conformations. b) Polymer chains grafted on curved surface and the transition into relaxed conformation at defined radius from surface. c) Schematic showing the proposed mechanism of the enhanced fracture toughness of PGNP materials with both extended and relaxed regimes of the polymer graft.

The preparation of PGNPs is achieved by one of two methods: grafting to or grafting from. In grafting to, the polymer chain is first synthesized then attached to the particle surface via a functional group is installed at the polymer chain-end which reacts with a complimentary functionality on the particle surface. While experimentally straightforward, the density of polymer chains achievable are defined and limited by the molecular weight of the grafting polymer. This is due to the steric hinderance between the polymers, which prevents grafting at short

intermolecular distances. Overcoming this tradeoff is achieved by grafting-from, where the nanoparticles are first modified with small-molecule initiators followed by surface-initiated polymerization to grow the polymer chains. Due to the many advantages of CRP outlined above, surface-initiated CRP (SI-CRP) is well-suited for this method. While some experimental optimization is usually necessary to transfer homogenous CRP conditions to particle surfaces, both SI-ATRP and SI-RAFT have been used extensively to prepare PGNPs. In addition, the multitude of polymer compositions and architectures offered by CRP can extend to PGNPs as well. Amphiphilic block copolymers prepared by CRP readily form complex self-assembled structures such as micelles and vesicles. He et al. showed that this feature extends to PGNPs as well.[67] By controlling both the direction and length of the hydrophobic and hydrophilic blocks of the grafted chains, large vesicles with shells composed entirely gold nanoparticles spontaneously formed in aqueous solution.

When considering the incredible ability of both MOFs and polymers prepared by CRP to create materials at the molecular level, it is not surprising that these methods individually have had such an impact in materials science. However, the lack of shared background and training between these areas of research has stymied their integration. As such, there remains a pressing need to develop reliable methods readily accessible to researchers in both fields for the development of the next generation of functional materials.

1.4 Scope of this Dissertation

This dissertation will discuss fundamental studies on the internal and external modification of MOFs with well-defined polymers and small molecules. Chapter 2 describes the surface-initiated RAFT polymerization from the surface of MOF particles and the self-assembly of these

materials into free-standing monolayers. Three MOFs, UiO-66, UiO-66-NH_2, and MIL-88B-NH_2, were modified by coordination of a RAFT initiator to the surface and poly(methyl methacrylate) brushes were grown from the surface. The polymer grafted particles were then self-assembled at the air-water interface to form thin-film monolayers. The effect of polymer molecular weight was investigated, and a threshold of 100 kDa was found to be the minimum molecular weight necessary for the film to remain free-standing.

Chapter 3 describes systematic investigations into the different factors affecting the self-assembly of polymer-grafted MOFs, including the size of the MOF particle, type of polymer, and polymer molecular weight. Coarse-grain simulations of the particle assembly at the air-water interface show how changes to particle size and polymer molecular weight lead to periodic ordering of the particles during self-assembly.

Chapter 4 describes the fundamental study of coordination to MOF surfaces by various ligands. By coordinating a dye to the surface of different MOFs, the strength of coordination of the different ligands to the MOF surface was determined quantitatively. Using increasing concentrations of the ligands, apparent binding constants for several ligands were derived and compared between MOFs.

1.5 References

1. Furukawa, H.; Cordova, K. E.; O'Keeffe, M.; Yaghi, O. M., The Chemistry and Applications of Metal-Organic Frameworks. *Science* **2013,** *341*, 1230444.

2. Eddaoudi, M.; Kim, J.; Rosi, N.; Vodak, D.; Wachter, J.; O'Keeffe, M.; Yaghi, O. M., Systematic Design of Pore Size and Functionality in Isoreticular MOFs and Their Application in Methane Storage. *Science* **2002,** *295*, 469-472.

3. Long, J. R.; Yaghi, O. M., The pervasive chemistry of metal–organic frameworks. *Chem. Soc. Rev.* **2009,** *38*, 1213-1214.

4. Zhou, H.-C.; Long, J. R.; Yaghi, O. M., Introduction to Metal–Organic Frameworks. *Chem. Rev.* **2012,** *112*, 673-674.

5. Liu, J.; Chen, L.; Cui, H.; Zhang, J.; Zhang, L.; Su, C.-Y., Applications of metal–organic frameworks in heterogeneous supramolecular catalysis. *Chem. Soc. Rev.* **2014,** *43*, 6011-6061.

6. Diercks, C. S.; Liu, Y.; Cordova, K. E.; Yaghi, O. M., The role of reticular chemistry in the design of CO2 reduction catalysts. *Nat. Mater.* **2018,** *17*, 301-307.

7. Murray, L. J.; Dincă, M.; Long, J. R., Hydrogen storage in metal–organic frameworks. *Chem. Soc. Rev.* **2009,** *38*, 1294-1314.

8. Wu, M.-X.; Yang, Y.-W., Metal–Organic Framework (MOF)-Based Drug/Cargo Delivery and Cancer Therapy. *Adv. Mater.* **2017,** *29*, 1606134.

9. Moghadam, P. Z.; Li, A.; Wiggin, S. B.; Tao, A.; Maloney, A. G. P.; Wood, P. A.; Ward, S. C.; Fairen-Jimenez, D., Development of a Cambridge Structural Database Subset: A Collection of Metal–Organic Frameworks for Past, Present, and Future. *Chem. Mater.* **2017,** *29*, 2618-2625.

10. Chung, Y. G.; Haldoupis, E.; Bucior, B. J.; Haranczyk, M.; Lee, S.; Zhang, H.; Vogiatzis, K. D.; Milisavljevic, M.; Ling, S.; Camp, J. S.; Slater, B.; Siepmann, J. I.; Sholl, D. S.; Snurr, R. Q., Advances, Updates, and Analytics for the Computation-Ready, Experimental Metal–Organic Framework Database: CoRE MOF 2019. *J. Chem. Eng. Data* **2019,** *64*, 5985-5998.

11. Li, H.; Eddaoudi, M.; O'Keeffe, M.; Yaghi, O. M., Design and synthesis of an exceptionally stable and highly porous metal-organic framework. *Nature* **1999,** *402*, 276-279.

12. Cavka, J. H.; Jakobsen, S.; Olsbye, U.; Guillou, N.; Lamberti, C.; Bordiga, S.; Lillerud, K. P., A New Zirconium Inorganic Building Brick Forming Metal Organic Frameworks with Exceptional Stability. *J. Am. Chem. Soc.* **2008,** *130*, 13850-13851.

13. Furukawa, H.; Gándara, F.; Zhang, Y.-B.; Jiang, J.; Queen, W. L.; Hudson, M. R.; Yaghi, O. M., Water Adsorption in Porous Metal–Organic Frameworks and Related Materials. *J. Am. Chem. Soc.* **2014,** *136*, 4369-4381.

14. Deng, H.; Doonan, C. J.; Furukawa, H.; Ferreira, R. B.; Towne, J.; Knobler, C. B.; Wang, B.; Yaghi, O. M., Multiple Functional Groups of Varying Ratios in Metal-Organic Frameworks. *Science* **2010,** *327*, 846-850.

15. Kandiah, M.; Nilsen, M. H.; Usseglio, S.; Jakobsen, S.; Olsbye, U.; Tilset, M.; Larabi, C.; Quadrelli, E. A.; Bonino, F.; Lillerud, K. P., Synthesis and Stability of Tagged UiO-66 Zr-MOFs. *Chem. Mater.* **2010,** *22*, 6632-6640.

16. Ahnfeldt, T.; Gunzelmann, D.; Loiseau, T.; Hirsemann, D.; Senker, J.; Férey, G.; Stock, N., Synthesis and Modification of a Functionalized 3D Open-Framework Structure with MIL-53 Topology. *Inorg. Chem.* **2009,** *48*, 3057-3064.

17. Taylor-Pashow, K. M. L.; Della Rocca, J.; Xie, Z.; Tran, S.; Lin, W., Postsynthetic Modifications of Iron-Carboxylate Nanoscale Metal−Organic Frameworks for Imaging and Drug Delivery. *J. Am. Chem. Soc.* **2009,** *131*, 14261-14263.

18. Wang, Z.; Cohen, S. M., Postsynthetic modification of metal–organic frameworks. *Chem. Soc. Rev.* **2009,** *38*, 1315-1329.

19. Kalaj, M.; Cohen, S. M., Postsynthetic Modification: An Enabling Technology for the Advancement of Metal–Organic Frameworks. *ACS Cent. Sci.* **2020,** *6*, 1046-1057.

20. Kiang, Y. H.; Gardner, G. B.; Lee, S.; Xu, Z.; Lobkovsky, E. B., Variable Pore Size, Variable Chemical Functionality, and an Example of Reactivity within Porous Phenylacetylene Silver Salts. *J. Am. Chem. Soc.* **1999,** *121*, 8204-8215.

21. Seo, J. S.; Whang, D.; Lee, H.; Jun, S. I.; Oh, J.; Jeon, Y. J.; Kim, K., A homochiral metal–organic porous material for enantioselective separation and catalysis. *Nature* **2000,** *404*, 982-986.

22. Wang, Z.; Cohen, S. M., Postsynthetic Covalent Modification of a Neutral Metal−Organic Framework. *J. Am. Chem. Soc.* **2007,** *129*, 12368-12369.

23. Nguyen, J. G.; Cohen, S. M., Moisture-Resistant and Superhydrophobic Metal−Organic Frameworks Obtained via Postsynthetic Modification. *J. Am. Chem. Soc.* **2010,** *132*, 4560-4561.

24. Suh, B. L.; Hyun, T.; Koh, D.-Y.; Kim, J., Rational Tuning of Ultramicropore Dimensions in MOF-74 for Size-Selective Separation of Light Hydrocarbons. *Chem. Mater.* **2021,** *33*, 7686-7692.

25. Jiang, H.; Zhang, W.; Kang, X.; Cao, Z.; Chen, X.; Liu, Y.; Cui, Y., Topology-Based Functionalization of Robust Chiral Zr-Based Metal–Organic Frameworks for Catalytic Enantioselective Hydrogenation. *J. Am. Chem. Soc.* **2020,** *142*, 9642-9652.

26. Conrad, J. C.; Robertson, M. L., Shaping the Structure and Response of Surface-Grafted Polymer Brushes via the Molecular Weight Distribution. *JACS Au* **2023,** *3*, 333-343.

27. Cohen, S. M., The Postsynthetic Renaissance in Porous Solids. *J. Am. Chem. Soc.* **2017,** *139*, 2855-2863.

28. Xu, Y.; Vermeulen, N. A.; Liu, Y.; Hupp, J. T.; Farha, O. K., SALE-Ing a MOF-Based "Ship of Theseus." Sequential Building-Block Replacement for Complete Reformulation of a Pillared-Paddlewheel Metal-Organic Framework. *Eur. J. Inorg. Chem.* **2016,** *2016*, 4345-4348.

29. Das, S.; Kim, H.; Kim, K., Metathesis in Single Crystal: Complete and Reversible Exchange of Metal Ions Constituting the Frameworks of Metal−Organic Frameworks. *J. Am. Chem. Soc.* **2009,** *131*, 3814-3815.

30. Brozek, C. K.; Michaelis, V. K.; Ong, T.-C.; Bellarosa, L.; López, N.; Griffin, R. G.; Dincă, M., Dynamic DMF Binding in MOF-5 Enables the Formation of Metastable Cobalt-Substituted MOF-5 Analogues. *ACS Cent. Sci.* **2015,** *1*, 252-260.

31. Brozek, C. K.; Dincă, M., Thermodynamic parameters of cation exchange in MOF-5 and MFU-4l. *Chem. Commun.* **2015,** *51*, 11780-11782.

32. Morabito, J. V.; Chou, L.-Y.; Li, Z.; Manna, C. M.; Petroff, C. A.; Kyada, R. J.; Palomba, J. M.; Byers, J. A.; Tsung, C.-K., Molecular Encapsulation beyond the Aperture Size Limit through Dissociative Linker Exchange in Metal–Organic Framework Crystals. *J. Am. Chem. Soc.* **2014,** *136*, 12540-12543.

33. Boissonnault, J. A.; Wong-Foy, A. G.; Matzger, A. J., Core–Shell Structures Arise Naturally During Ligand Exchange in Metal–Organic Frameworks. *J. Am. Chem. Soc.* **2017,** *139*, 14841-14844.

34. Mu, Q.; Jiang, G.; Chen, L.; Zhou, H.; Fourches, D.; Tropsha, A.; Yan, B., Chemical Basis of Interactions Between Engineered Nanoparticles and Biological Systems. *Chem. Rev.* **2014,** *114*, 7740-7781.

35. Forgan, R. S., The surface chemistry of metal–organic frameworks and their applications. *Dalton Trans.* **2019,** *48*, 9037-9042.

36. Figueroa-Quintero, L.; Villalgordo-Hernández, D.; Delgado-Marín, J. J.; Narciso, J.; Velisoju, V. K.; Castaño, P.; Gascón, J.; Ramos-Fernández, E. V., Post-Synthetic Surface Modification of Metal–Organic Frameworks and Their Potential Applications. *Small Methods* **2023,** *7*, 2201413.

37. Kondo, M.; Furukawa, S.; Hirai, K.; Kitagawa, S., Coordinatively Immobilized Monolayers on Porous Coordination Polymer Crystals. *Angew. Chem. Int. Ed.* **2010,** *49*, 5327-5330.

38. Wang, S.; McGuirk, C. M.; Ross, M. B.; Wang, S.; Chen, P.; Xing, H.; Liu, Y.; Mirkin, C. A., General and Direct Method for Preparing Oligonucleotide-Functionalized Metal–Organic Framework Nanoparticles. *J. Am. Chem. Soc.* **2017,** *139*, 9827-9830.

39. Röder, R.; Preiß, T.; Hirschle, P.; Steinborn, B.; Zimpel, A.; Höhn, M.; Rädler, J. O.; Bein, T.; Wagner, E.; Wuttke, S.; Lächelt, U., Multifunctional Nanoparticles by Coordinative Self-Assembly of His-Tagged Units with Metal–Organic Frameworks. *J. Am. Chem. Soc.* **2017,** *139*, 2359-2368.

40. Chen, X.; Zhuang, Y.; Rampal, N.; Hewitt, R.; Divitini, G.; O'Keefe, C. A.; Liu, X.; Whitaker, D. J.; Wills, J. W.; Jugdaohsingh, R.; Powell, J. J.; Yu, H.; Grey, C. P.; Scherman, O. A.; Fairen-Jimenez, D., Formulation of Metal–Organic Framework-Based Drug Carriers by Controlled Coordination of Methoxy PEG Phosphate: Boosting Colloidal Stability and Redispersibility. *J. Am. Chem. Soc.* **2021,** *143*, 13557-13572.

41. Wang, S.; Morris, W.; Liu, Y.; McGuirk, C. M.; Zhou, Y.; Hupp, J. T.; Farha, O. K.; Mirkin, C. A., Surface-Specific Functionalization of Nanoscale Metal–Organic Frameworks. *Angew. Chem. Int. Ed.* **2015,** *54*, 14738-14742.

42. Ryu, U.; Jee, S.; Rao, P. C.; Shin, J.; Ko, C.; Yoon, M.; Park, K. S.; Choi, K. M., Recent advances in process engineering and upcoming applications of metal–organic frameworks. *Coord. Chem. Rev.* **2021,** *426*, 213544.

43. Ren, J.; Langmi, H. W.; North, B. C.; Mathe, M., Review on processing of metal–organic framework (MOF) materials towards system integration for hydrogen storage. *Int. J. Energy Res.* **2015,** *39*, 607-620.

44. Kalaj, M.; Bentz, K. C.; Ayala, S., Jr.; Palomba, J. M.; Barcus, K. S.; Katayama, Y.; Cohen, S. M., MOF-Polymer Hybrid Materials: From Simple Composites to Tailored Architectures. *Chem. Rev.* **2020,** *120*, 8267-8302.

45. Qian, Q.; Asinger, P. A.; Lee, M. J.; Han, G.; Mizrahi Rodriguez, K.; Lin, S.; Benedetti, F. M.; Wu, A. X.; Chi, W. S.; Smith, Z. P., MOF-Based Membranes for Gas Separations. *Chem. Rev.* **2020,** *120*, 8161-8266.

46. Denny, M. S.; Moreton, J. C.; Benz, L.; Cohen, S. M., Metal–organic frameworks for membrane-based separations. *Nat. Rev. Mater.* **2016,** *1*, 16078.

47. Lin, R.; Villacorta Hernandez, B.; Ge, L.; Zhu, Z., Metal organic framework based mixed matrix membranes: an overview on filler/polymer interfaces. *J. Mater. Chem. A* **2018,** *6*, 293-312.

48. Ma, L.; Svec, F.; Lv, Y.; Tan, T., Engineering of the Filler/Polymer Interface in Metal–Organic Framework-Based Mixed-Matrix Membranes to Enhance Gas Separation. *Chem. Asian J.* **2019,** *14*, 3502-3514.

49. Zhang, Y.; Feng, X.; Li, H.; Chen, Y.; Zhao, J.; Wang, S.; Wang, L.; Wang, B., Photoinduced Postsynthetic Polymerization of a Metal–Organic Framework toward a Flexible Stand-Alone Membrane. *Angew. Chem. Int. Ed.* **2015,** *54*, 4259-4263.

50. Xie, K.; Fu, Q.; Webley, P. A.; Qiao, G. G., MOF Scaffold for a High-Performance Mixed-Matrix Membrane. *Angew. Chem. Int. Ed.* **2018,** *57*, 8597-8602.

51. Satheeshkumar, C.; Yu, H. J.; Park, H.; Kim, M.; Lee, J. S.; Seo, M., Thiol–ene photopolymerization of vinyl-functionalized metal–organic frameworks towards mixed-matrix membranes. *J. Mater. Chem. A* **2018,** *6*, 21961-21968.

52. Gao, X.; Zhang, J.; Huang, K.; Zhang, J., ROMP for Metal–Organic Frameworks: An Efficient Technique toward Robust and High-Separation Performance Membranes. *ACS Appl. Mater. Interfaces* **2018,** *10*, 34640-34645.

53. McDonald, K. A.; Feldblyum, J. I.; Koh, K.; Wong-Foy, A. G.; Matzger, A. J., Polymer@MOF@MOF: "grafting from" atom transfer radical polymerization for the synthesis of hybrid porous solids. *Chem. Commun.* **2015,** *51*, 11994-11996.

54. He, S.; Wang, H.; Zhang, C.; Zhang, S.; Yu, Y.; Lee, Y.; Li, T., A generalizable method for the construction of MOF@polymer functional composites through surface-initiated atom transfer radical polymerization. *Chem. Sci.* **2019,** *10*, 1816-1822.

55. Zoppe, J. O.; Ataman, N. C.; Mocny, P.; Wang, J.; Moraes, J.; Klok, H.-A., Surface-Initiated Controlled Radical Polymerization: State-of-the-Art, Opportunities, and Challenges in Surface and Interface Engineering with Polymer Brushes. *Chem. Rev.* **2017,** *117*, 1105-1318.

56. Wang, J.-S.; Matyjaszewski, K., Controlled/"living" radical polymerization. atom transfer radical polymerization in the presence of transition-metal complexes. *J. Am. Chem. Soc.* **1995,** *117*, 5614-5615.

57. Matyjaszewski, K.; Xia, J., Atom Transfer Radical Polymerization. *Chem. Rev.* **2001,** *101*, 2921-2990.

58. Lorandi, F.; Fantin, M.; Matyjaszewski, K., Atom Transfer Radical Polymerization: A Mechanistic Perspective. *J. Am. Chem. Soc.* **2022,** *144*, 15413-15430.

59. Chiefari, J.; Chong, Y. K.; Ercole, F.; Krstina, J.; Jeffery, J.; Le, T. P. T.; Mayadunne, R. T. A.; Meijs, G. F.; Moad, C. L.; Moad, G.; Rizzardo, E.; Thang, S. H., Living Free-Radical Polymerization by Reversible Addition−Fragmentation Chain Transfer: The RAFT Process. *Macromolecules* **1998,** *31*, 5559-5562.

60. Moad, G.; Rizzardo, E.; Thang, S. H., Living Radical Polymerization by the RAFT Process – A Third Update. *Aust. J. Chem.* **2012,** *65*, 985-1076.

61. Corrigan, N.; Jung, K.; Moad, G.; Hawker, C. J.; Matyjaszewski, K.; Boyer, C., Reversible-deactivation radical polymerization (Controlled/living radical polymerization): From discovery to materials design and applications. *Prog. Polym. Sci.* **2020,** *111*, 101311.

62. Truong, N. P.; Jones, G. R.; Bradford, K. G. E.; Konkolewicz, D.; Anastasaki, A., A comparison of RAFT and ATRP methods for controlled radical polymerization. *Nat. Rev. Chem.* **2021,** *5*, 859-869.

63. Dau, H.; Jones, G. R.; Tsogtgerel, E.; Nguyen, D.; Keyes, A.; Liu, Y.-S.; Rauf, H.; Ordonez, E.; Puchelle, V.; Basbug Alhan, H.; Zhao, C.; Harth, E., Linear Block Copolymer Synthesis. *Chem. Rev.* **2022,** *122*, 14471-14553.

64. Zhou, D.; Zhu, L.-W.; Wu, B.-H.; Xu, Z.-K.; Wan, L.-S., End-functionalized polymers by controlled/living radical polymerizations: synthesis and applications. *Polym. Chem.* **2022,** *13*, 300-358.

65. Matyjaszewski, K., Advanced Materials by Atom Transfer Radical Polymerization. *Adv. Mater.* **2018,** *30*, 1706441.

66. Choi, J.; Hui, C. M.; Pietrasik, J.; Dong, H.; Matyjaszewski, K.; Bockstaller, M. R., Toughening fragile matter: mechanical properties of particle solids assembled from polymer-grafted hybrid particles synthesized by ATRP. *Soft Matter* **2012,** *8*, 4072-4082.

67. He, J.; Liu, Y.; Babu, T.; Wei, Z.; Nie, Z., Self-Assembly of Inorganic Nanoparticle Vesicles and Tubules Driven by Tethered Linear Block Copolymers. *J. Am. Chem. Soc.* **2012,** *134*, 11342-11345.

Chapter 2: Free-Standing Metal–Organic Framework (MOF) Monolayers by Self-Assembly of Polymer-Grafted Nanoparticles

2.1 Introduction

The modification of MOFs with polymers through the various PSP methods discussed in Chapter 1 is an attractive method to prepare MOF-polymer hybrid materials. To ensure strong interactions between the polymer and MOF surface, most methodologies form covalent bonds between the organic linker of the MOF and the polymer chain. These covalent PSM and PSP strategies in general necessitate a modifiable functional group on the ligand. For example, one of the more common procedures used for PSP utilizes amide bond formation between a MOF containing amines, such as UiO-66-NH_2, and an activated carboxylate.[1-7] This presents a challenge to further extend the PSP methodology to other MOFs, as many MOFs contain ligands that are either incompatible with or difficult to derivatize with free amines. More broadly, the introduction of functional groups on the MOF ligand can alter the targeted properties of the MOF. In order to create a PSP method more broadly applicable to a variety of MOFs, researchers have turned to the metal coordination of the MOF SBUs. As the SBU is a ubiquitous part of the MOF structure, methods that utilize coordination for PSP allow for a more general approach to grafting polymers to the MOF structure.

In Chapter 1, He et al. demonstrated that a polymer decorated with carboxylate side chains could coordinate several different MOFs while also providing initiation sites for polymerization.[8] After coordination of the polymeric ligand to the MOF surface, SI-ATRP was used to grow polymers from the surface of the MOF. The ability to use the same ligand for many different MOFs highlights the flexibility of the coordination strategy as a general purpose method for MOF modification. Recently, PSP from ZIF-8 (ZIF = Zeolitic Imidazolate Framework) was reported which used the coordination of an imidazole-bound initiator for SI-ATRP from the MOF surface.[9] After the successful polymerization of methyl methacrylate (MMA), the polymer-coated particles

could be self-assembled into monolayers at the air-water interface. This was the first example of self-assembled MOF monolayers (SAMMs) constructed from MOFs decorated with polymer brushes. However, the PSE approach for surface functionalization was only demonstrated on ZIF-8, which contains the imidazole linkers necessary for surface PSE to occur. Furthermore, while the polymer was successfully characterized, it was shown that the SI-ATRP conditions gave poor control over the polymerization and low molecular weight polymer grafts. This resulted in monolayer films too fragile to be physically removed from the water surface. These results the worthwhile pursuit of developing a SI-CRP methodology that is not only applicable to a wide range of MOFs, but also affords polymers with a controlled and predictable molecular weight.

In Chapter 2, the development of a general methodology for the preparation of MOFs with a polymer coating is described. Three MOFs, UiO-66(Zr), UiO-66(Zr)-NH_2, and MIL-88B(Fe)-NH_2 were surface functionalized using a catechol-modified CTA (cat-CTA) for the SI-RAFT polymerization of methyl methacrylate (MMA) (Scheme 2.1). The MOFs used in this study were chosen to demonstrate the versatility of cat-CTA to coordinate the surface of MOFs bearing different particle morphologies, sizes, SBUs, and ligand functionalities. Furthermore, following successful controlled polymerization, monolayers of the polymer-coated MOFs were prepared through self-assembly at an air-water interface.

2.2 Results and Discussion

To coordinate the surface of the MOFs with initiator, the RAFT CTA was first modified with a catechol functional group. Synthesis of the catechol-modified RAFT CTA (cat-CTA) was performed using a two-step acylation procedure between a commercially available CTA and dopamine hydrochloride as previously reported (Scheme 2.1).[10] UiO-66(Zr) truncated octahedra,

UiO-66(Zr)-NH_2 octahedra, and MIL-88B(Fe)-NH_2 hexagonal rods were selected for modification. Due to the low tolerance for particle size dispersity in self-assembled particle-brush systems,[11] each MOF was prepared via solvothermal methods that gave relatively narrow size dispersities of the desired morphology.[2, 12-13] Powder X-ray diffraction (PXRD) and gas sorption analysis with N_2 gas were in good agreement with previous reports, while scanning electron microscopy (SEM) images of the MOFs showed discrete particles with controlled morphology and size (Figure 2S.1-4).

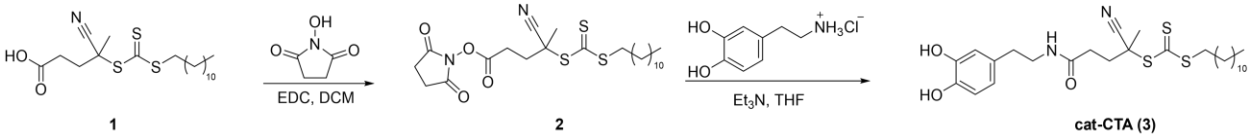

Scheme 2.1. Synthesis of catechol-modified CTA: 2-cyano-5-((3,4-dihydroxyphenethyl)amino)-5-oxopentan-2-yl dodecyl carbonotrithioate (**cat-CTA**) **(3)**.

The surface functionalization of UiO-66(Zr) with cat-CTA was accomplished using a phase-transfer methodology adapted from a previously reported procedure (Scheme 2.2).[14] The MOF particles were dispersed in water and the cat-CTA was dissolved in chloroform. The two solutions were combined and mixed with a vortex mixer for several minutes to functionalize the MOF surface. Ethanol was added to break up the resulting emulsion and the particles were collected by centrifugation, washed several times with THF, and dried under vacuum. A sample of UiO-66(Zr)-CTA was digested in dilute HF and analysed by ^{1}H NMR, which confirmed the presence of the cat-CTA (Figure 2S.5). PXRD and N_2 gas sorption analysis of the sample indicated the addition of the cat-CTA did not affect the crystallinity or accessible porosity of UiO-66(Zr), and SEM images showed that no particle etching or a change in morphology occurred (Figures 2S.1 and 2S.2). The increase in surface area is suspected to be a result of the functionalization

procedure involving redispersion in water and washing the particles again. This acts as a second round of activation to remove any residual impurities that may have remained after particle synthesis.

Scheme 2.2. Surface functionalization procedure for coordinating cat-CTA to MOF. MOF particles (UiO-66) are depicted by polyhedron with aqueous and organic solvents represented by the blue and yellow layers, respectively. Mixed (vortexed) solutions represented by green color.

The polymer brush was grown from the surface of UiO-66(Zr) using RAFT polymerization of methyl methacrylate (MMA). To determine the amount cat-CTA coordinated to the surface of UiO-66(Zr), first a ratio of the MOF ligand to cat-CTA was measured using ^{1}H NMR analysis of the digested UiO-66(Zr). This value was then used to calculate the amount of CTA present on the surface of the MOF, and a mass ratio of ~250 µg of CTA per 10 mg of UiO-66(Zr) was obtained (see ESI for details). A molar ratio of 5000:1 MMA to cat-CTA was chosen for a target degree of polymerization (DP) of 2000 and carried out at 70 °C using DMF as a solvent and AIBN as a free radical initiator. The high molar ratio of monomer to target DP is necessary as surface-initiated polymerizations are known to give crosslinked particles at high conversions, resulting in macroscopic gels.[15] Free CTA was also added to the polymerization reaction to increase the initial concentration of the transfer agent and improve control over the molecular weight of the polymers growing from the MOF surfaces. Following the polymerization, the particles were recovered by centrifugation and the supernatant was poured into methanol to precipitate the free polymer grown in solution (which was retained for molecular weight analysis by gel permeation chromatography

(GPC). The remaining polymer-coated MOF was washed several times with THF and toluene to remove any unbound polymer and finally suspended in toluene for self-assembly. While PXRD analysis of particles indicated the crystallinity of the MOF was unaffected by the polymerization, the surface area decreased by ~39% to 846 $m^2 g^{-1}$ (Figure 2S.1, 2S.6, Table 2S.2). To correct for the added mass from the nonporous polymer, thermal gravimetric analysis (TGA) of UiO-66(Zr)-PMMA compared to unfunctionalized UiO-66 calculated that the sample is composed of 20% polymer by mass (Figure 2S.6). The adjusted surface area would then be ~1015 $m^2 g^{-1}$, indicating that UiO-66-PMMA still retains 73% of the total surface area of the parent MOF.

Monolayers of UiO-66(Zr)-PMMA were prepared through self-assembly at an air water interface by dispersing the MOF in toluene at 50-100 mg mL^{-1} and placing a 10 µL drop on the surface of a layer of water in a 55 mm diameter petri dish. The drop spread immediately to the edges forming a thin film with an iridescent color (Figure 2S.6). A free-standing film was obtained by lifting a copper wire loop up from under the water surface. The loop was fashioned small enough (diameter = 7 mm) that a water drop was trapped in the ring by surface tension with the film floating on the surface. This allowed the monolayer to be lifted without fracturing, and slow evaporation of the water in ambient conditions resulted in a self-supporting membrane of the MOF monolayer (Figure 2.1a). Surprisingly, even though the films are almost entirely composed of MOF particles, the free-standing films were translucent and maintained their iridescence. SEM images of the free-standing film showed the particles maintained a tightly packed structure with only small defects present (Figure 2.1b-c).

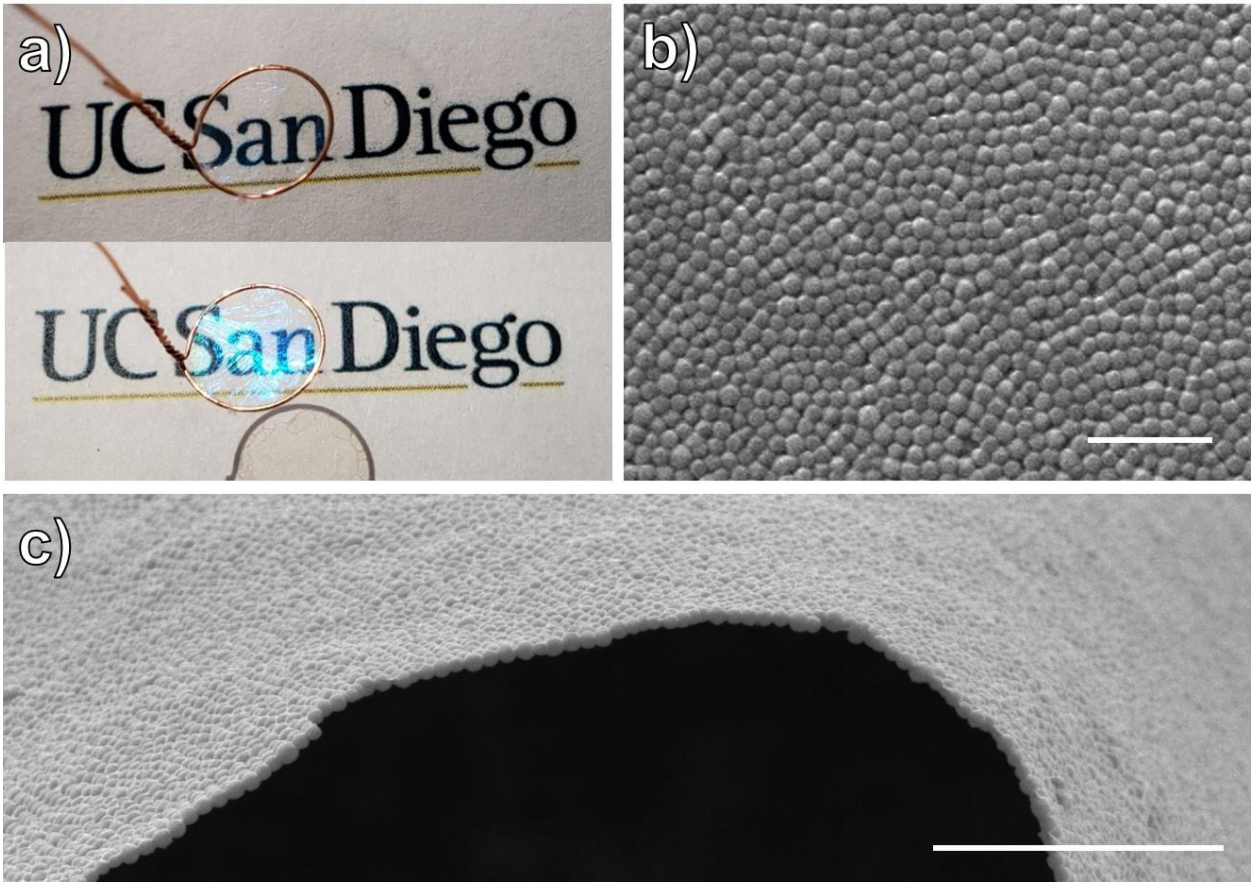

Figure 2.1. Free-standing monolayer of self-assembled UiO-66(Zr)-PMMA. (a) Images of the monolayer taken at different angles to show both clarity and iridescence. (b) SEM image of the monolayer surface showing tightly packed UiO-66(Zr)-PMMA particles. Scale bar is 2 μm. (c) SEM image of film from the side, illustrating the continuous monolayer. Scale bar is 5 μm.

Functionalized MOF samples were digested with HF to recover the polymer brush from the MOF surface for molecular weight analysis by GPC and compared to the polymer recovered from the supernatant. The molecular weight of the surface polymer (M_n = 252 kg mol^{-1}, $Đ$ = 1.17) and the free polymer (isolated from the RAFT reaction, vide supra, M_n = 263 kg mol^{-1}, $Đ$ = 1.15) are similar, and the low dispersity of both indicate the polymerization is controlled by the RAFT mechanism. The effect of polymer molecular weight on monolayer formation and particle ordering was investigated by halting the polymerization at several time points (Figures 2S.12 and 2S.13). In the first hour, the molecular weight reached only 8.3 kg mol^{-1}, which was too small

prevent particle aggregation as shown by SEM (Figure 2.2a-b). At two hours, the molecular weight increased to 59 kg mol^{-1}, and monolayers were observed (Figure 2.2c). However, these monolayers could not form free-standing films, presumably due to the relatively weak particle interactions leaving large gaps between the MOFs (Figure 2.2c). Once the molecular weight reached 138 kg mol^{-1} at four hours polymerization time, free-standing films of densely packed particles were obtained. These results highlight the importance of polymer length on stabilizing the interparticle interactions and increasing film strength (Figure 2.2d).

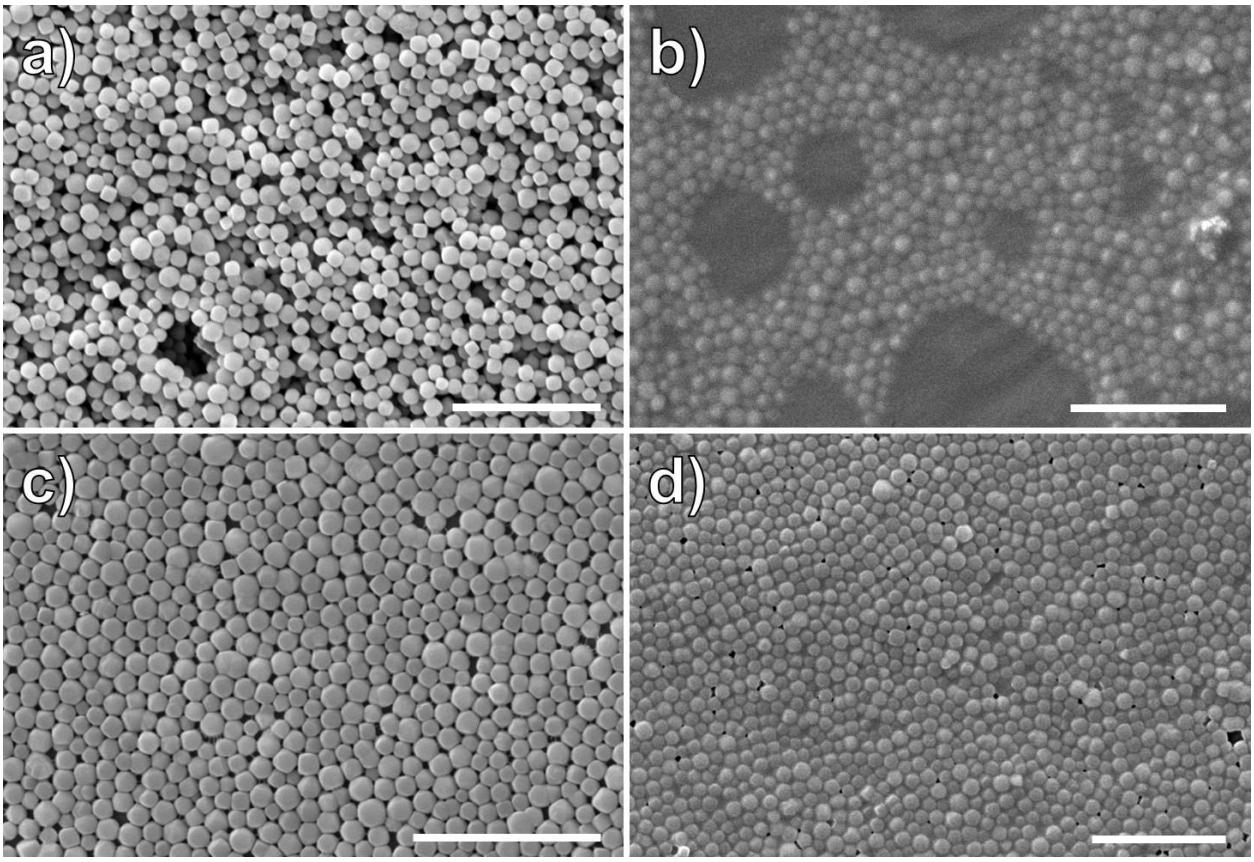

Figure 2.2. Effect of polymer brush molecular weight on order and packing of UiO-66(Zr) particles. a) 30 minutes, M_n = 6.3 kg mol^{-1} $Đ$ = 2.15. b) 1 hour, M_n = 8.3 kg mol^{-1} $Đ$ = 1.8. c) 2 hours, M_n = 59 kg mol^{-1} $Đ$ = 1.49. d) 4 hours, M_n = 138 kg mol^{-1} $Đ$ = 1.16. All scale bars are 3 μm.

This methodology of polymerization and self-assembly was then attempted with other MOF nanoparticles. UiO-66(Zr)-NH_2 octahedra and MIL-88B(Fe)-NH_2 hexagonal nanorods were chosen to demonstrate the generality of the methodology towards different SBUs, chemical functionalities, and particle morphologies. Functionalization of the surface with cat-CTA using the same methodology was successful, and ^{1}H NMR analysis digested UiO-66(Zr)-CTA showed the amine of the organic linker remained unfunctionalized (Figure 2S.14). Following polymerization and digestion of the polymer coated MOFs, GPC analysis of the polymer brush gave molecular weights and dispersities for UiO-66(Zr)-NH_2-PMMA (M_n = 215 kg mol^{-1}, $Đ$ = 1.17) and MIL-88B(Fe)-NH_2-PMMA (M_n = 190 kg mol^{-1}, $Đ$ = 1.22) that were comparable to UiO-66(Zr). PXRD and gas sorption analysis indicate the effect on crystallinity and surface area of UiO-66(Zr)-NH_2-PMMA was comparable to UiO-66(Zr)-PMMA, with the high crystallinity preserved and a total surface area of 692 m^2 g^{-1} (Table 2S.1, Figures 2S.3, 2S.7). MIL-88B(Fe)-NH_2 is an expanding MOF with pores that remain closed unless swollen with solvent such as DMF; therefore, these materials were non-porous and no change in surface area could be measured under the conditions used for measuring gas sorption.[16] Surprisingly, the PXRD of MIL-88B(Fe)-NH_2-PMMA changed, giving a diffraction pattern consistent with the open form of the MOF (Figure 2S.4).[17] While the exact reason for this is unknown, it is possible that the polymer brush makes the complete removal of DMF more difficult and DMF is still present in the interior of these MOF particles. Self-assembly of these MOFs resulted in freestanding monolayers of MIL-88B(Fe)-NH_2-PMMA (Figure 2.3a); however, the UiO-66(Zr)-NH_2-PMMA could only make free-standing films when deposited at a thickness of 2-3 particles (Figure 2S.15). This may be due to the substantially smaller particle size of UiO-66(Zr)-NH_2 (<100 nm) versus UiO-66(Zr) (~250 nm) and MIL-88B(Fe)-NH_2 (anisotropic shape, >700 × 100 nm). Assuming the films are strengthened

by the intercalation of polymer chains in the lateral direction, the smaller particle size of UiO-66(Zr)-NH_2 would result in fewer interchain polymer interactions, leading to a less robust film structure.

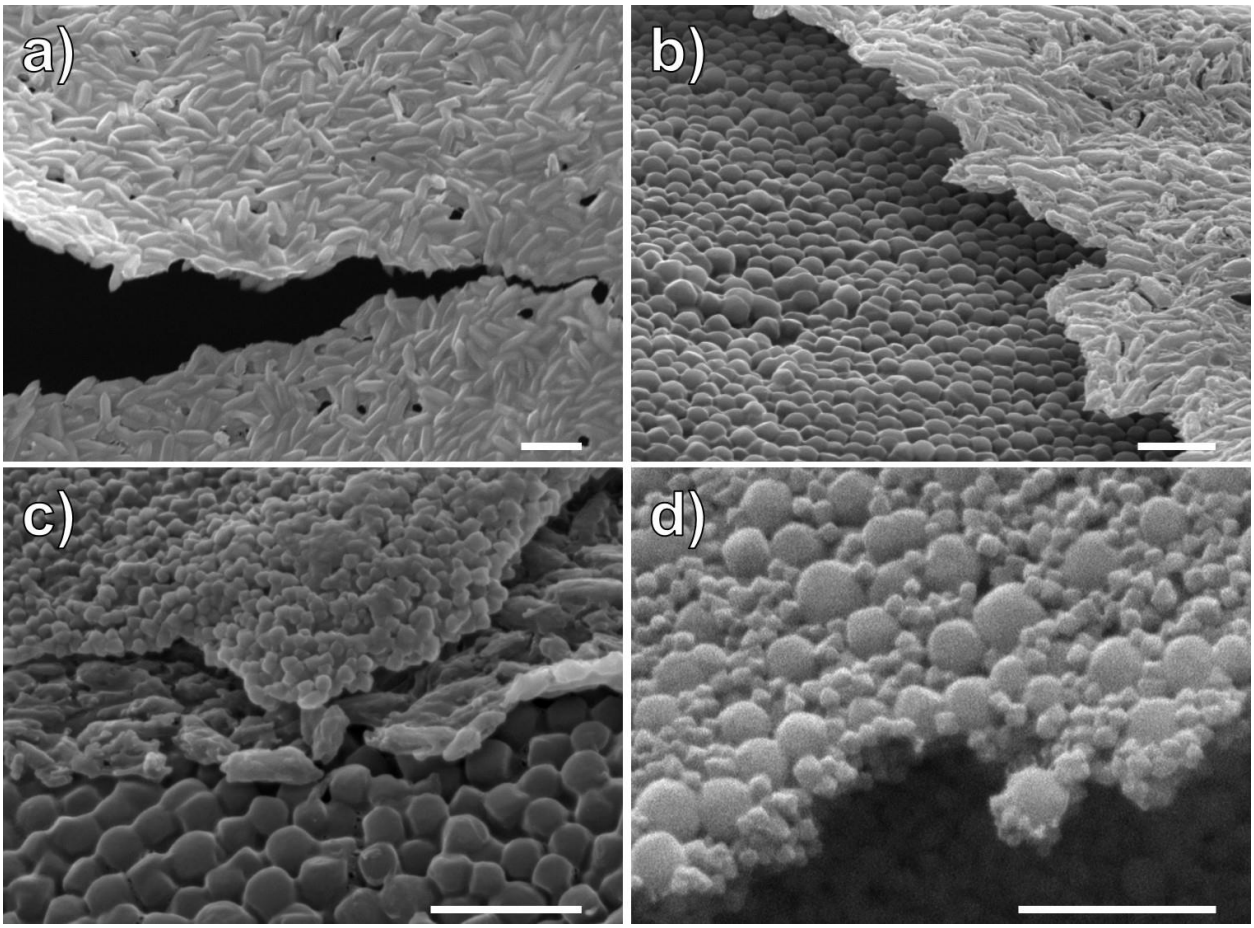

Figure 2.3. Monolayer, multilayers, and mixed monolayers of MOFs. a) Monolayer of MIL-88B(Fe)-NH_2-PMMA. b) Bilayer of UiO-66(Zr)-PMMA (*bottom*) and MIL-88B(Fe)-NH_2-PMMA (*top*). c) Multilayer of UiO-66(Zr)-PMMA (*bottom*) and MIL-88B(Fe)-NH_2-PMMA (*middle*) and UiO-66(Zr)-NH_2-PMMA (*top*). d) Mixed monolayer comprised of UiO-66(Zr)-PMMA (larger particles) and UiO-66(Zr)-NH_2-PMMA (smaller particles). All scale bars are 1 μm.

One advantage of creating membranes through the self-assembly of individually functionalized particles is that the modularity allows for the components to be assembled in different combinations to create multifunctional composites. To demonstrate this, a monolayer of

UiO-66(Zr)-PMMA was coated on a glass slide with SEM tape. After drying, a layer of MIL-88B(Fe)-NH_2-PMMA was applied to form a bilayer of both MOFs (Figure 2.3b), followed by a layer of UiO-66(Zr)-NH_2 to form a multilayer film (Figure 2.3c). In addition, mixed monolayers of the MOFs were also fabricated by mixing a toluene suspension of both UiO-66(Zr)-PMMA and UiO-66(Zr)-NH_2-PMMA which were then self-assembled together (Figure 2.3c). The SEM images show that the large size discrepancy between the two MOFs allows for the smaller UiO-66(Zr)-NH_2-PMMA to fill gaps between the larger UiO-66(Zr)-PMMA, resulting in a monolayer that combines the functionalities of both MOFs without adding any extra thickness (Figure 2.3d).

2.3 Conclusion

In conclusion, this study provides a general methodology to functionalize MOF nanoparticles with RAFT CTAs for controlled radical polymerization from the MOF surface. These multifunctional, porous nanoparticles were further self-assembled into ultra-thin films of MOF particles and demonstrated to be fully free-standing with inherent iridescence and good optical clarity. Furthermore, multi-layered composites were realized through the sequential layering of films, and monolayers of mixed MOFs were synthesized through the self-assembly of MOF mixtures. This system establishes a modular route towards novel multifunctional membranes. However, only a single polymer, PMMA was used in this study, and characterization of the polymer brush structure was not performed. In Chapter 3, the effect of different polymers, particle sizes, and grafting density is explored in more detail.

2.4 Appendix: Supporting Information

General Materials and Methods. All starting materials and reagents were purchased from commercial suppliers (Sigma-Aldrich, Fisher Scientific, Acros Organics, Combi-blocks, and others) and used without further purification.

Characterization

Nuclear Magnetic Resonance. Proton nuclear magnetic resonance spectra (1H NMR) were recorded on a Varian FT-NMR spectrometer (400 MHz). Chemical shifts are reported in parts per million (ppm) referenced to the appropriate solvent peak.

Gel Permeation Chromatography (GPC). Gel permeation chromatography (GPC) was performed in THF at 35 °C with a flow rate of 1.0 mL min^{-1} using an Agilent 1260 HPLC with diode array, Wyatt DAWN HELEOS 8+ light scattering detector, Viscostar III viscometer, and Optilab TrEX refractive index.

Powder X-Ray Diffraction (PXRD). ~50 mg of dry MOF powder or 0.5 cm^2 or SAMM was mounted on a silicon sample holder for analysis by PXRD. PXRD data was collected at ambient temperature on a Bruker D8 Advance diffractometer at 40 kV, 40 mA for Cu Ka (l = 1.5418 Å), with a scan speed of 2 sec/step, a step size of 0.05° in 2θ, and a 2θ range of 2-50°.

BET Surface Area Analysis. Samples for analysis were evacuated on a vacuum line overnight at room temperature prior to analysis. ~50 mg samples were then transferred to pre-weighed sample tubes and degassed at 105 °C on a Micromeritics ASAP 2020 Adsorption Analyzer for a minimum of 12 h or until the outgas rate was <5 mmHg. After degassing, the sample tubes were re-weighed to obtain a consistent mass for the samples. BET surface area (m^2 g^{-1}) measurements

were collected at 77 K with N_2 on a Micromeritics ASAP 2020 Adsorption Analyzer using volumetric techniques.

Scanning Electron Microscopy (SEM). MOF particles or MMM films (~3 mm^2) were transferred to conductive carbon tape on a sample holder disk, and coated using an Ir-sputter coating for 8 sec. A FEI Quanta 250 SEM instrument was used for acquiring images using a 5 kV energy source under vacuum at a working distance at 10 mm.

Experimental.

Synthesis of cat-CTA (3).

NHS-CTA (2). A 100 mL round bottom flask was charged with **1** (Scheme 2.1, 1 g, 2.5 mmol, 1 eq., Combi-blocks), *N*-hydroxysuccinimide (428 mg, 3.6 mmol, 1.5 eq.) and 40 mL of dry dichloromethane. The flask was degassed with argon for 5 min and cooled to 0 °C, after which EDC (760 mg, 4.0 mmol, 1.6 eq.) was added and the reaction was left to stir at room temperature under an argon atmosphere overnight. Upon completion, the organic layer was washed with 1 M HCl (1 × 100 mL), saturated $NaHCO_3$ (1 × 100 mL), brine, and dried with Na_2SO_4. Compound **2** was purified using column chromatography (EtOAc/hexane, 0-50%, elutes at 35%) to give a yellow solid. Yield: 1.01 g, 81%. ^{1}H NMR (300 MHz, $CDCl_3$): δ 3.38 – 3.27 (m, 2H), 2.93 (t, J = 8.4 Hz, 2H), 2.85 (s, 4H), 2.72 – 2.59 (m, 1H), 2.52 (ddd, J = 14.4, 9.3, 7.1 Hz, 1H), 1.88 (s, 3H), 1.76 – 1.63 (m, 2H), 1.58 (s, 1H), 1.42 (s, 1H), 1.26 (s, 18H), 0.88 (t, J = 6.7 Hz, 3H). ESI-MS(+) Experimental: *m/z* 523.13 $[M+Na]^+$, Calculated for $[C_{23}H_{36}N_2O_4S_3]$: 500.14.

cat-CTA (3). A 100 mL round bottom flask was charged with **2** (1 g, 2.0 mmol, 1 eq.), dopamine hydrochloride (417 mg, 2.2 mmol, 1.1 eq.) and 50 mL of dry THF. The flask was degassed with argon for 5 minutes and cooled to 0 °C, after which triethylamine (306 µl, 2.2 mmol, 1.1 eq.) was

added dropwise and the reaction was left under an argon atmosphere in the ice bath to warm to room temperature overnight. After 24 h, the reaction was diluted with 100 mL of 1M HCl and extracted with $CHCl_3$ (3 × 50 mL). The combined organic layers were washed with brine and dried with Na_2SO_4. Compound **3** was purified by column chromatography (EtOAc/hexane, 0-70%, elutes at 50%) and dried overnight in a vacuum oven to give a resinous, amber oil. Yield: 880 mg, 82%. ^{1}H NMR (500 MHz, $CDCl_3$): δ 6.81 (d, J = 8.0 Hz, 1H), 6.70 (d, J = 1.8 Hz, 1H), 6.59 (d, J = 8.0 Hz, 1H), 3.47 (dd, J = 5.9, 4.5 Hz, 2H), 3.32 (t, J = 7.5 Hz, 2H), 2.70 (t, J = 6.8 Hz, 2H), 2.54 – 2.45 (m, 1H), 2.45 – 2.38 (m, 2H), 2.37 – 2.28 (m, 1H), 1.86 (s, 3H), 1.75 – 1.60 (m, 3H), 1.43 – 1.33 (m, 2H), 1.25 (s, 18H), 0.88 (t, J = 6.9 Hz, 3H). ESI-MS(+) Experimental: *m/z* 539.21 $[M+H]^+$, Calculated for $[C_{27}H_{42}N_2O_3S_3]$: 538.24.

MOF Syntheses

UiO-66(Zr). A 250 mL flask was charged with terephthalic acid (440 mg, 2.7 mmol, 1 eq.) and $ZrCl_4$ (617 mg, 2.7 mmol, 1 eq.) and dissolved in 150 mL DMF. Acetic acid (4.55 mL, 80 mmol, 30 eq.) was added, and the solution was divided into 15 mL portions in 6 dram vials with Teflon lined caps. The vials were placed in a sand bath in a preheated 120 °C oven to crystallize for 24 h. The vials were cooled to room temperature, combined into 50 mL centrifuge tubes, and the white solid was collected by centrifugation (7000 rpm, 10 min). The particles were then washed through repeated dispersion/centrifugation cycles with DMF (2 × 40 mL, 2 h each) and methanol (3 × 40 mL, 24 h each) and dried in a vacuum oven at 50 °C overnight.

UiO-66(Zr)-NH_2. A 20 mL vial was charged with $ZrCl_4$ (61 mg, 0.26 mmol, 1 eq.) and 2-aminoterephthalic acid (43 mg, 0.26 mmol) and dissolved in 15 mL DMF. Acetic acid (0.45 mL, 7.9 mmol, 30 eq.) was added and the vial was then placed in a 120 °C oven for 24 h. After cooling

to ambient temperature, the particles were collected by centrifugation (7000 rpm, 10 min.). The particles were then washed through repeated dispersion/centrifugation cycles with DMF (2x40 mL, 2 h each) and methanol (3 × 40 mL, 24 h each). Using a modified procedure, the formyl groups were restored to free amine. 200 mg of UiO-66(Zr)-NH_2 was added to 10 mL MeOH:H_2O 1:1 mixture with 50 μL of conc. HCl and refluxed overnight. The solid was collected by filtration and washed with methanol.

MIL-88B(Fe)-NH_2. A 150 mL flask with a stir bar was charged with 640 mg of Pluronic F127 surfactant dissolved in 60 mL of DI H_2O. Iron(III) chloride hexahydrate (716 mg, 2.6 mmol, 2 eq.) was added and the solution was stirred for 1 h, after which acetic acid (2.4 mL, 42 mmol, 32 eq.) was added. After stirring 1 h, 2-aminoterephthalic acid (240 mg, 1.3 mmol, 1 eq.) was added and the suspension was kept stirring for 2 h. The reaction mixture was transferred to a 100 mL autoclave and placed in a preheated oven at 110 °C oven for 24 h. The solution was cooled to room temperature and the dark purple particles were washed through repeated dispersion/centrifugation cycles with DMF (2 × 30 mL, 30 min. each) and ethanol (4 × 30 mL, 30 min. each) and dried in a vacuum oven at 60 °C overnight.

MOF Functionalization, Polymerization, and Self-Assembly.

Surface Functionalization of MOFs with CTA. A vial filled with 10 mL of DI H_2O and 200 mg of MOF was sonicated for 30 min to suspend the particles. A 50 mL centrifuge tube was prepared with 4 mg of cat-CTA (**3**) dissolved in 5 mL of $CHCl_3$ and the solution of suspended particles was added. The biphasic mixture was vortexed for 3 min and 20 mL of EtOH was added to form a homogenous suspension. The particles were collected by centrifugation (6000 rpm, 10 min.), washed through repeated dispersion/centrifugation cycles with EtOH (2 × 25 mL, 30 min each)

and THF (25 mL, 12 h), and dried overnight in a vacuum oven at 50 °C. Particle digestion for ^{1}H NMR analysis was performed by sonicating 10-15 mg of dried MOF in a 1 mL plastic centrifuge tube with 400 µL d_6-DMSO and minimal (~6 µL) HF (48% H_2O) until a clear solution was obtained.

Polymerization of MMA from CTA-Functionalized MOFs. A solution of AIBN in DMF (10 mg mL^{-1}) and free CTA in DMF (1 mg mL^{-1}) were prepared. A 10 mL round bottom flask was charged with 10 mg of CTA@MOF (0.46 µmol cat-CTA, 1 equiv.) and 2 mL of DMF. The flask was sonicated for 30 min to fully suspend the MOFs before methyl methacrylate (2.0 mL, 18.8 mmol, 40000 equiv.) was added and the reaction was sonicated an additional 30 min. From the prepared stock solutions, 7.6 µL AIBN (76 µg, 0.46 µmol, 1 equiv.) and 1.9 µL free CTA (758 µg, 2 µmol, 1 equiv.) were both added and the reaction was degassed with argon for 30 min. The flask was briefly sonicated for 5 min before being placed in an oil bath heated to 70 °C. The polymerization was quenched by cooling in liquid nitrogen before opening the flask and adding 6 mL of DMF. The particles were collected by centrifugation (10000 rpm, 20 min) and the supernatant was poured into 10x excess rapidly stirring MeOH to precipitate the polymer. The remaining solids were washed through repeated dispersion/centrifugation cycles with DMF (30 mL, 1 h), THF (2 × 30 mL, 6 h), and toluene (30 mL, 1 h) and suspended in 150 µL of toluene for self-assembly. Particle digestion to isolate the polymer for GPC analysis was performed by sonicating 15-20 mg of dried MOF-PMMA in a 15 mL plastic centrifuge tube with 100 µL d_6-DMSO and 20 µL HF (48% H_2O) until a clear solution was obtained. 2 mL of 1M NaOH was added followed by 5 mL of toluene and vigorously mixed before separating the layers by centrifugation. The toluene layer was transferred to a 20 mL vial and dried in a vial under vacuum. The remaining residue was dissolved in 150 µl THF for GPC analysis.

Self-Assembly at the Air-Water Interface. The polymer-coated MOFs were suspended in toluene at 50-100 mg mL^{-1} through sonication. A 10 µL drop of the solution was place on the surface of water in a 55 mm diameter petri dish. After the toluene evaporated, the SAMM was lifted onto the surface of SEM carbon tape on a glass slide for imaging. For free-standing monolayers, a copper loop was prepared by wrapping copper wire (diameter = 0.5 mm) around a 1 mL plastic syringe barrel. The loop was removed and placed under the water surface, then quickly lifted from underneath the monolayer, suspending a drop of water with the film floating on the surface. The loop was hung to air dry, leaving a thin film of the MOF which was then imaged by SEM.

Figures and Tables

Table 2S.1. Surface area results from N_2 gas sorption analysis. Mass loss indicates percent mass loss during TGA heating up to 600 °C normalized with respect to the unfunctionalized MOF.

Material	Surface area (m^2 g^{-1})	Normalized mass loss (%)	Approximate Corrected Surface Area (m^2 g^{-1})
UiO-66(Zr)	1039	0	1040
UiO-66(Zr)-CTA	1342	3.5	1389
UiO-66(Zr)-PMMA	846	20	1015
UiO-66(Zr)-NH_2	1010	0	1010
UiO-66(Zr)-NH_2-CTA	1078	0	1078
UiO-66(Zr)-NH_2-PMMA	591	17	692

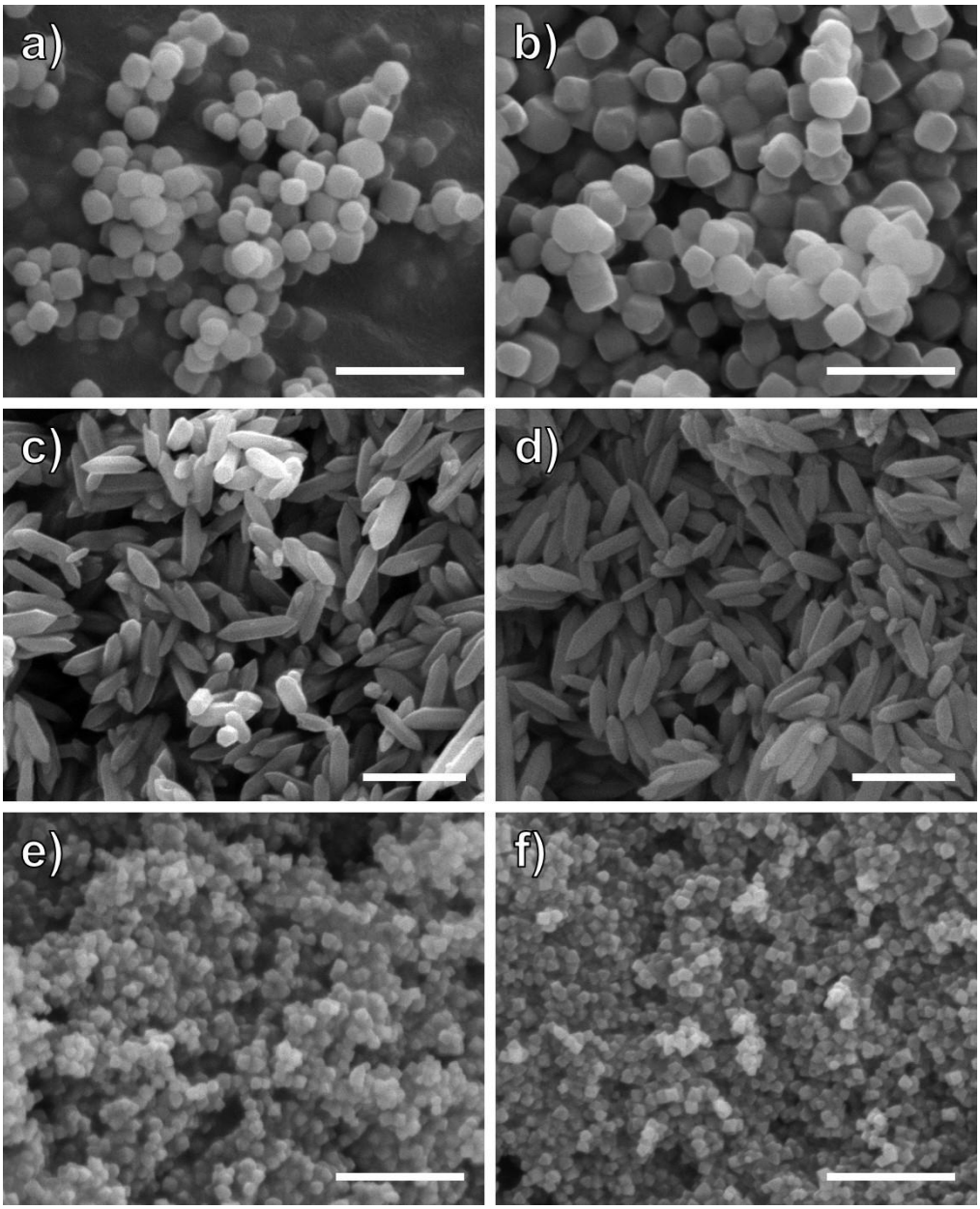

Figure 2S.1. SEM images of the different MOFs before and after functionalization with cat-CTA. a) UiO-66(Zr). b) UiO-66(Zr)-CTA. c) MIL-88B(Fe)-NH_2. d) MIL-88B(Fe)-NH_2-CTA. e) UiO-66(Zr)-NH_2. f) UiO-66(Zr)-NH_2-CTA. All scale bars are 1μm.

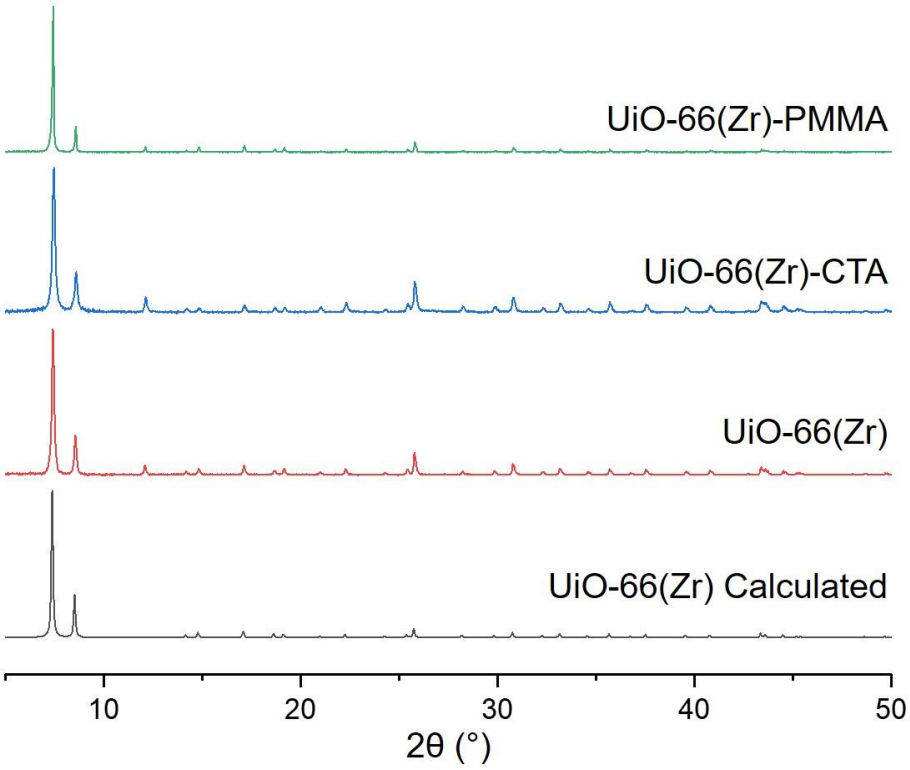

Figure 2S.2. PXRD spectra of UiO-66(Zr) (simulated pattern), UiO-66(Zr), UiO-66(Zr)-CTA, and UiO-66(Zr)-PMMA.

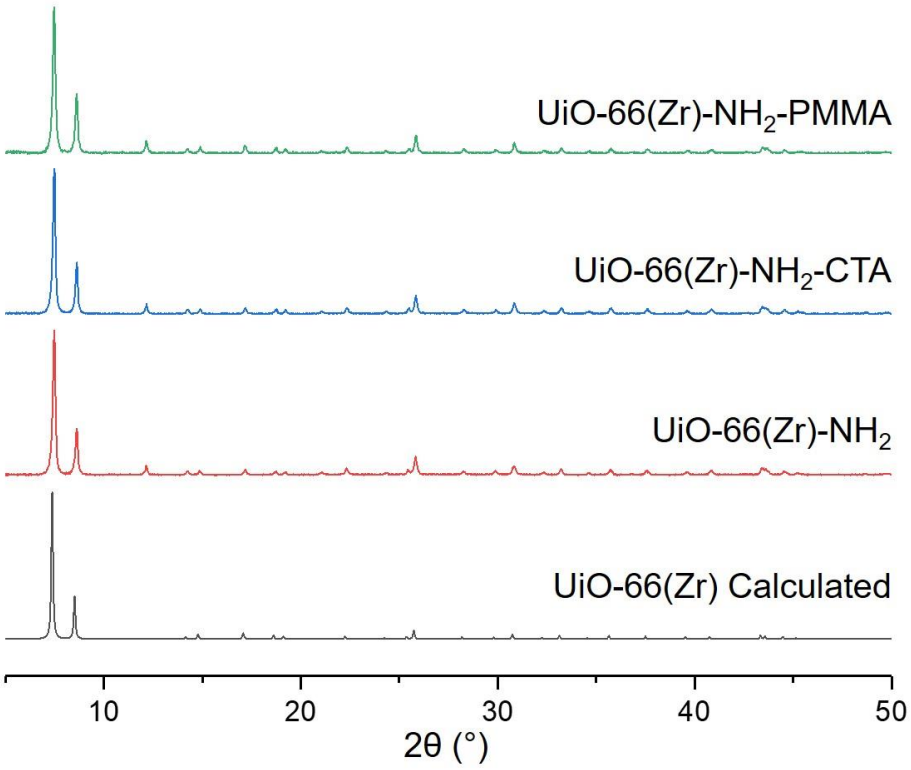

Figure 2S.3. PXRD spectra of UiO-66(Zr) (simulated pattern), UiO-66(Zr)-NH_2, UiO-66(Zr)-NH_2-CTA, and UiO-66(Zr)-NH_2-PMMA.

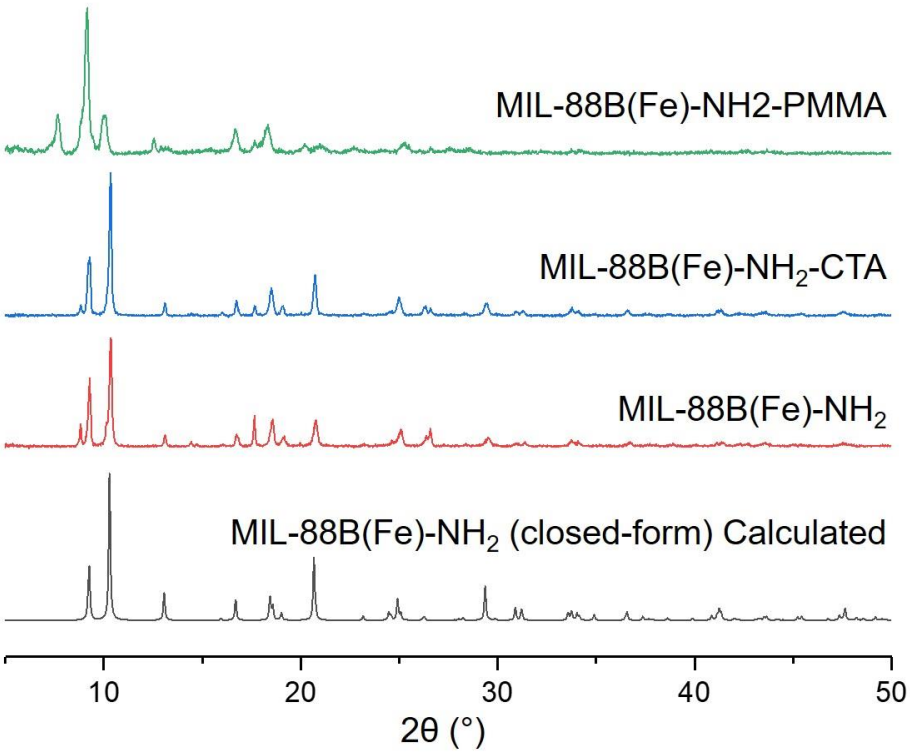

Figure 2S.4. PXRD spectra of MIL-88B(Fe)-NH_2 (simulated pattern), MIL-88B(Fe)-NH_2, MIL-88B(Fe)-NH_2-CTA, and MIL-88B(Fe)-NH_2-PMMA.

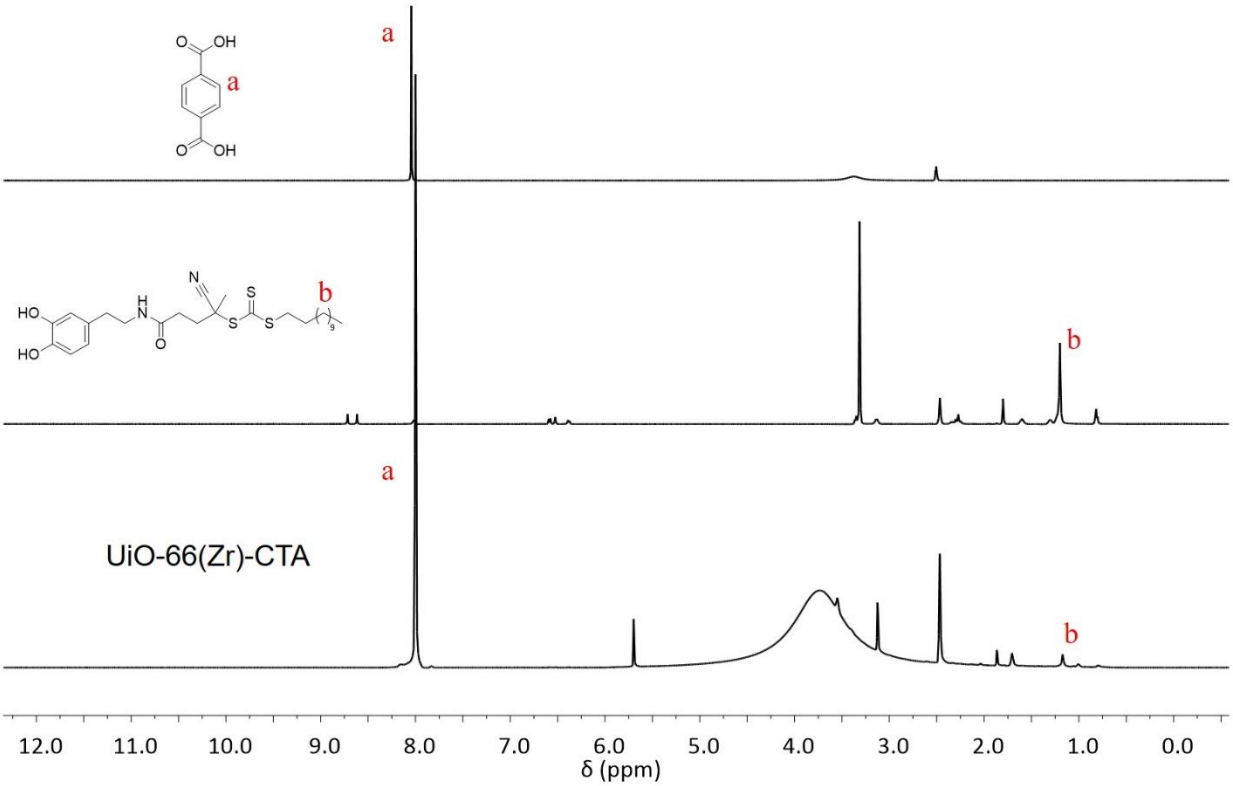

Figure 2S.5. ^{1}H NMR of terephthalic acid (top) and cat-CTA (middle) compared to digestion of UiO-66(Zr)-CTA (bottom).

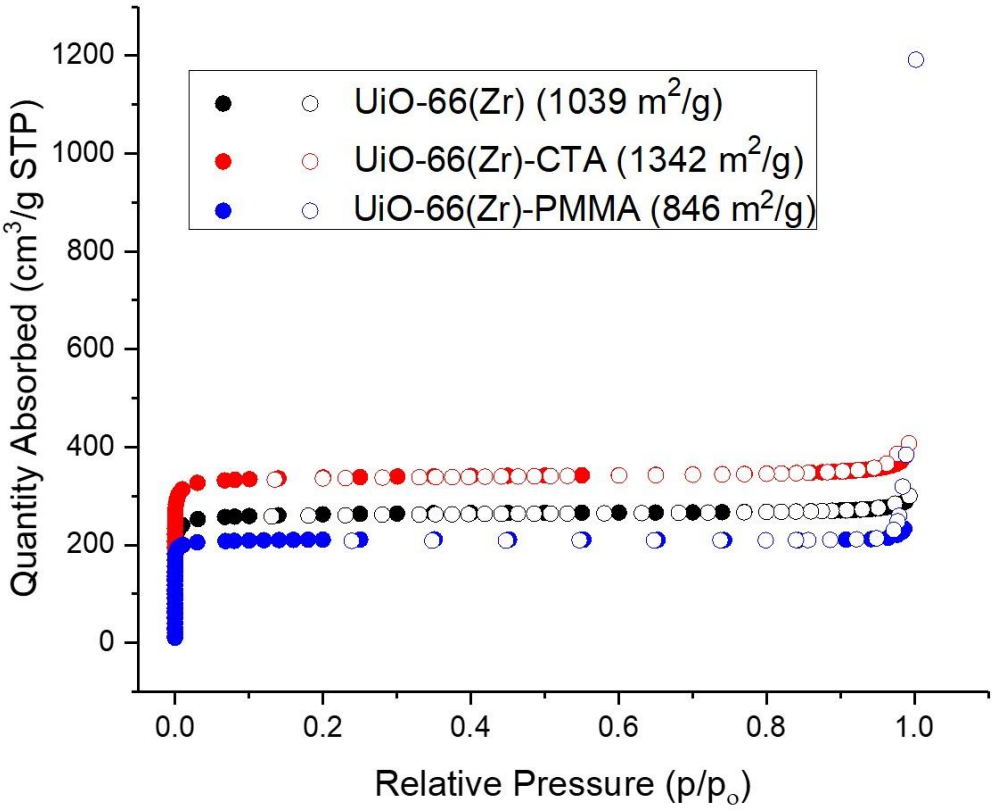

Figure 2S.6. N_2 sorption isotherm for UiO-66(Zr), UiO-66(Zr)-CTA, and UiO-66(Zr)-PMMA with respective BET surface areas.

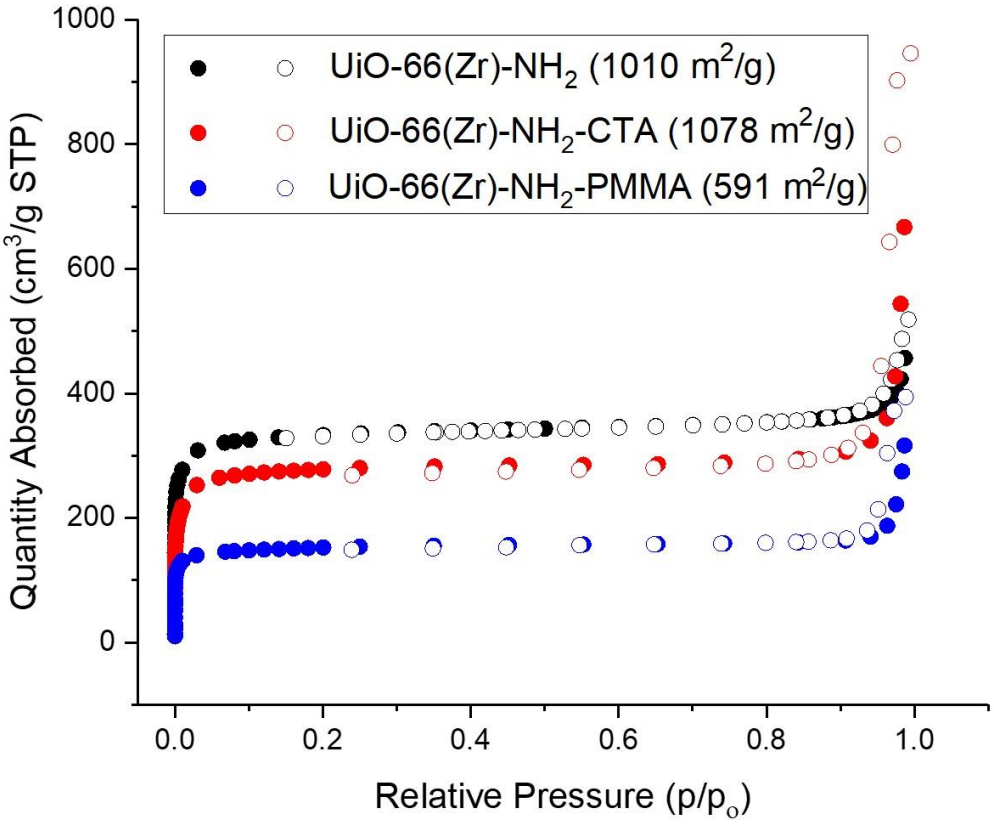

Figure 2S.7. N_2 sorption isotherm for UiO-66(Zr)-NH_2, UiO-66(Zr)-NH_2-CTA, and UiO-66(Zr)-NH_2-PMMA with respective BET surface areas.

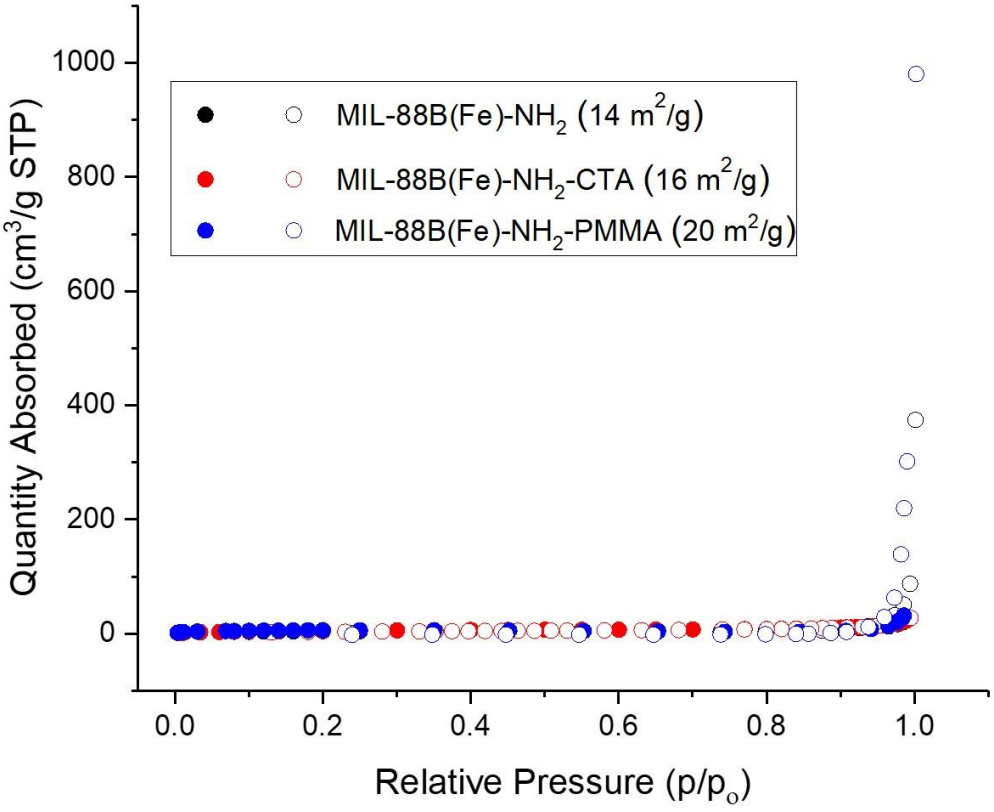

Figure 2S.8. N_2 sorption isotherm for MIL-88B(Fe)-NH_2 and MIL-88B(Fe)-NH_2-PMMA with respective BET surface areas.

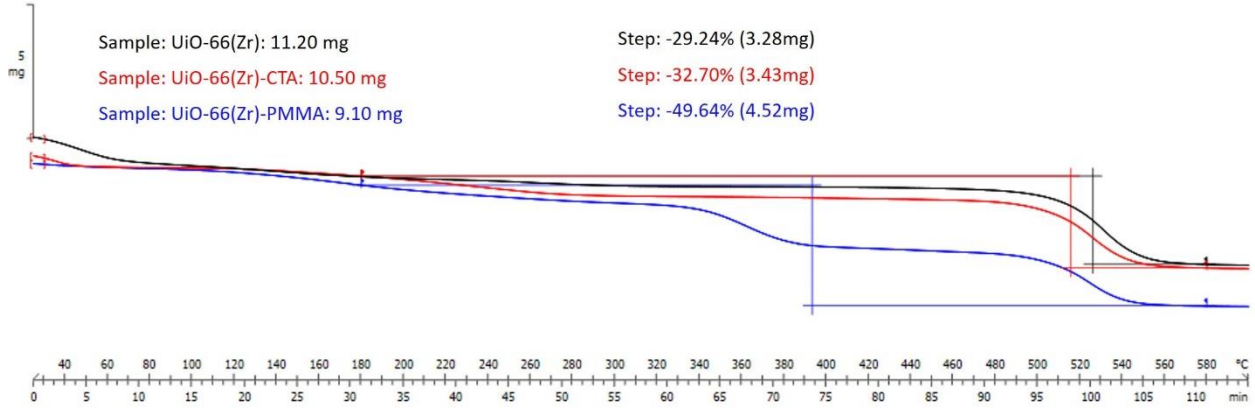

Figure 2S.9. TGA data for UiO-66(Zr), UiO-66(Zr)-CTA, and UiO-66(Zr)-PMMA.

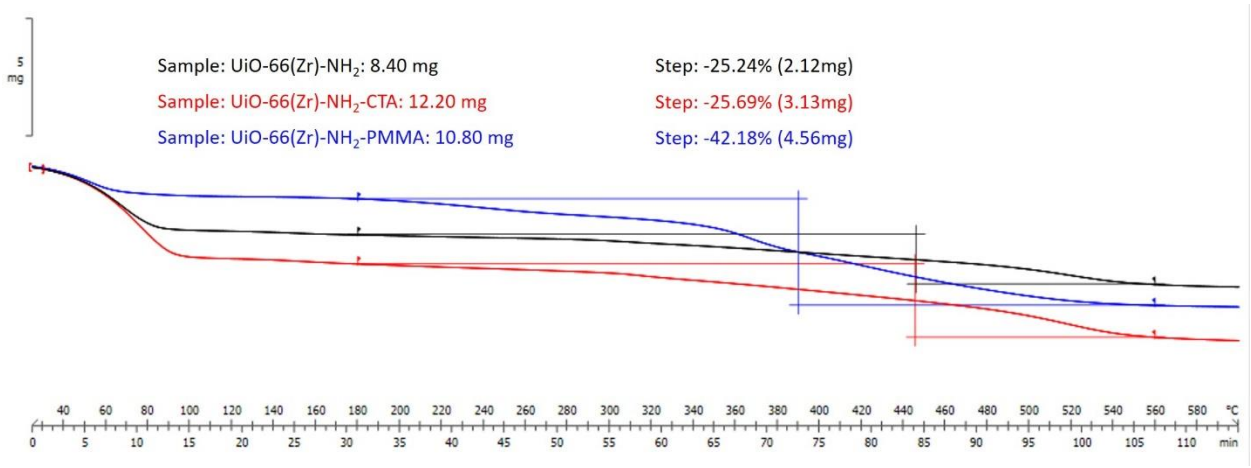

Figure 2S.10. TGA data for UiO-66(Zr)-NH_2, UiO-66(Zr)-NH_2-CTA, and UiO-66(Zr)-NH_2-PMMA.

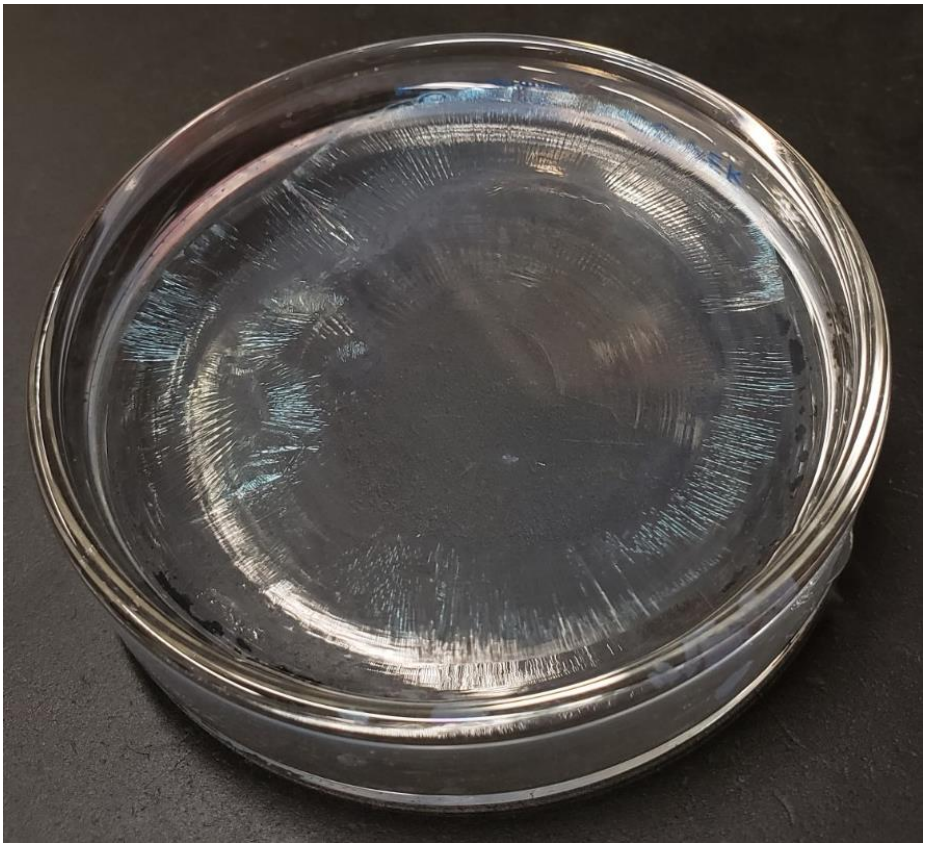

Figure 2S.11. Image of monolayer film of UiO-66(Zr)-PMMA showing the faint iridescent color.

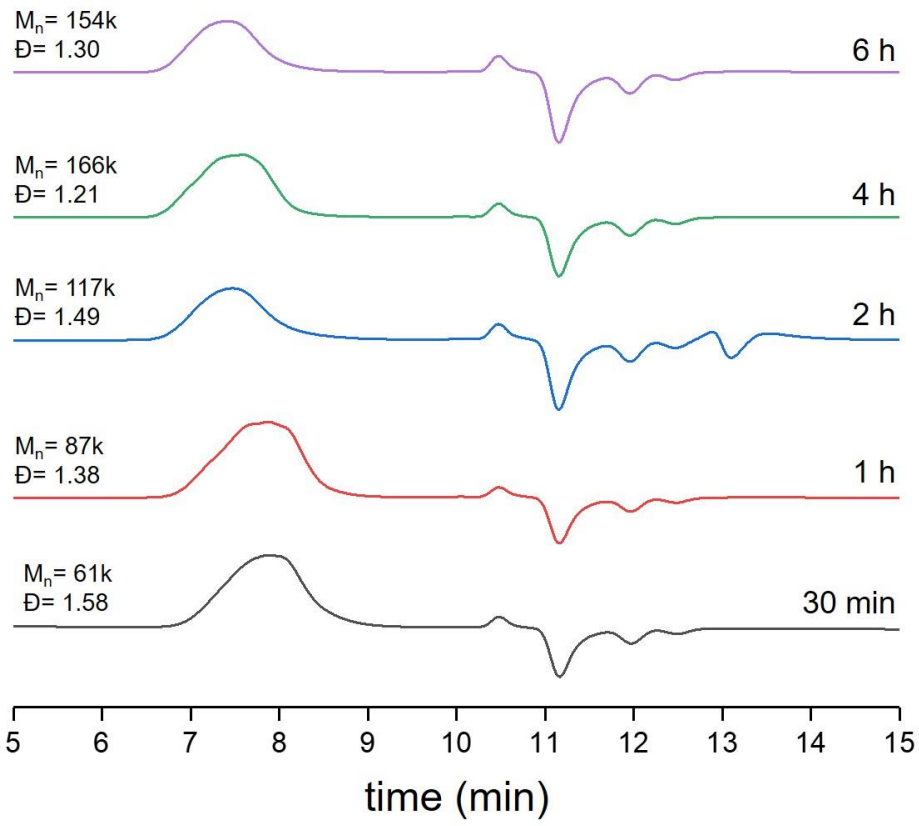

Figure 2S.12. GPC traces of the polymer recovered from the supernatant from the RAFT polymerization time study with UiO-66(Zr)-CTA.

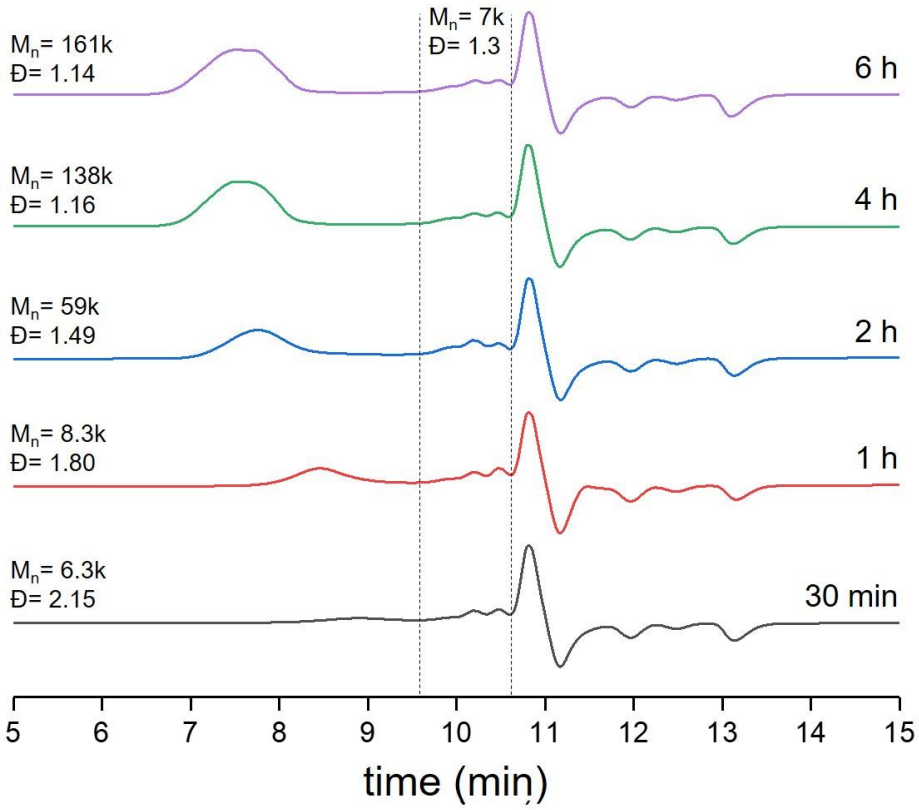

Figure 2S.13. GPC traces of the polymer brush recovered from the UiO-66(Zr)-PMMA surface after the RAFT polymerization time study.

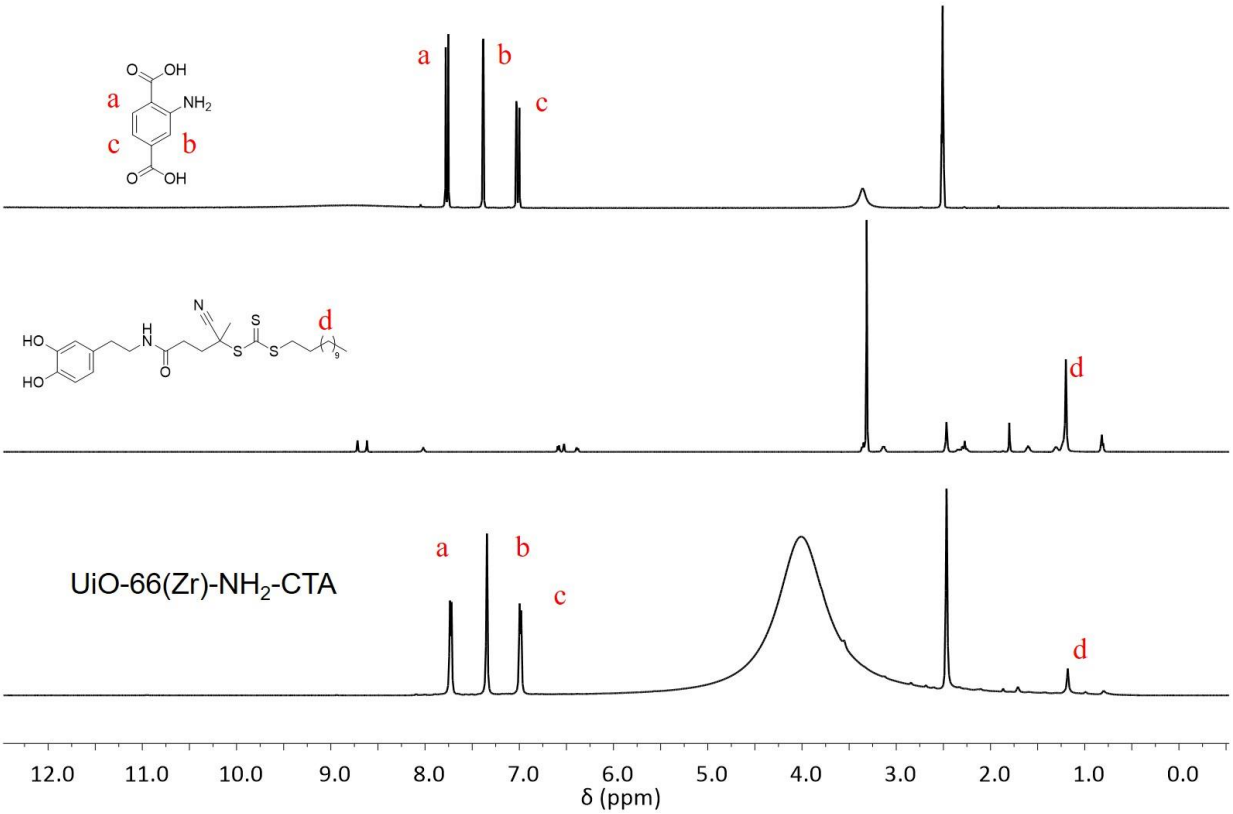

Figure 2S.14. ^{1}H NMR of 2-aminoterephthalic acid (top) and cat-CTA (middle) compared to digestion of UiO-66(Zr)-NH_2-CTA (bottom).

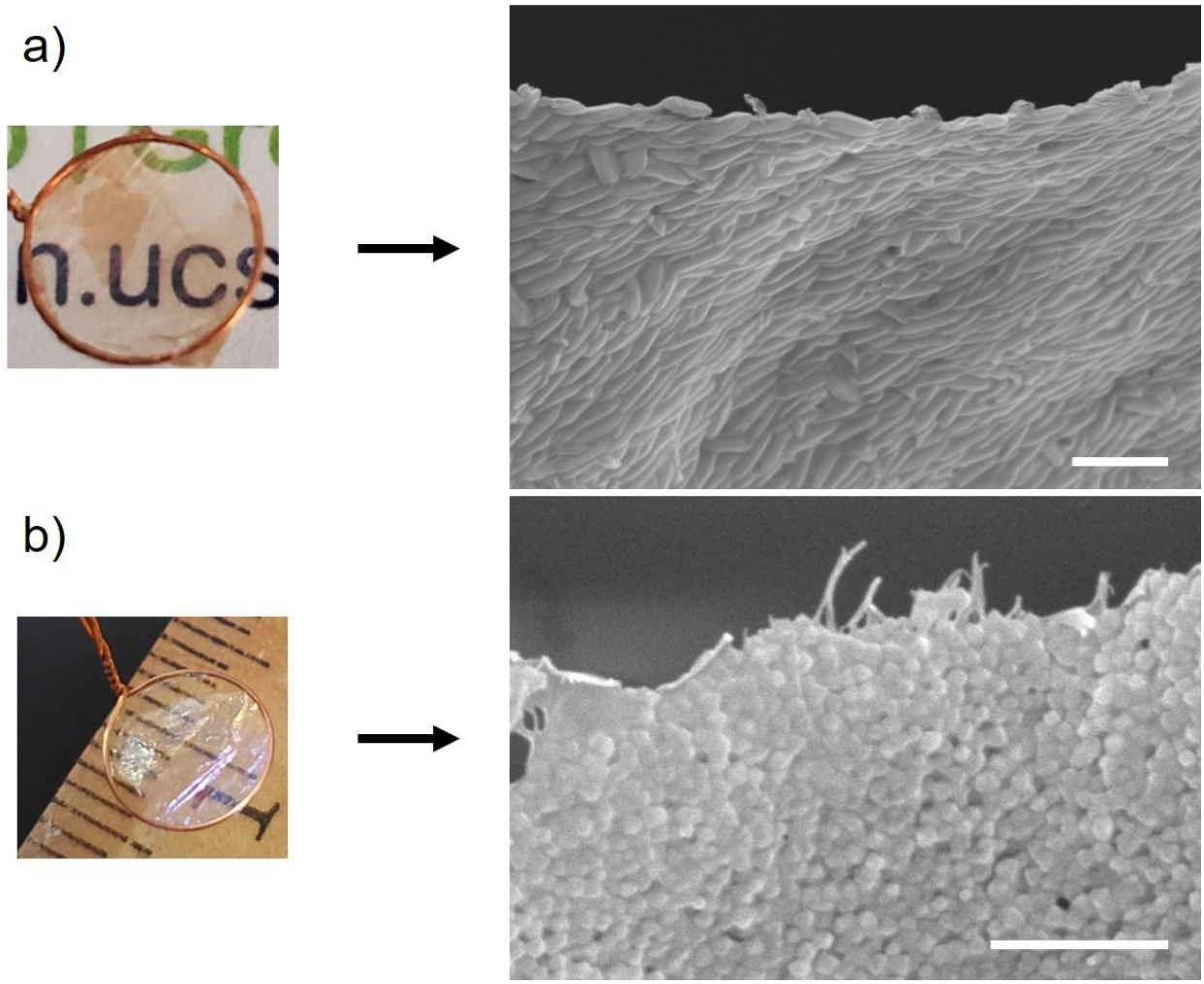

Figure 2S.15. Free-standing films of MOFs and SEM images. a) MIL-88B(Fe)-NH_2-PMMA. b) UiO-66(Zr)-NH_2-PMMA. All scale bars are 1 μm.

Determination of amount of cat-CTA on the surface of UiO-66(Zr)-CTA.

The average facet length of the UiO-66(Zr) particle was determined to be roughly 250 nm based on SEM images. The surface area and volume of each particle was calculated as a cube for simplicity.

$$MOF\ surface\ area = 6 \times (2500\text{Å})^2 = 3.75 \times 10^7\ \text{Å}^2$$

$$MOF\ volume = (2500\text{Å})^3 = 1.56 \times 10^{10}\ \text{Å}^3$$

The dimension of a single edge of the unit cell for UiO-66(Zr) is 2.08 nm according to the literature (*J. Am. Chem. Soc.* 2008, 130, 42, 13850-13851.), so the surface area and volume of the unit cell are

$$Unit\ cell\ surface\ area = 6 \times (20.8\text{Å})^2 = 2596\text{Å}^2$$

$$Unit\ cell\ volume = (20.8\text{Å})^3 = 8999\text{Å}^3$$

The number of unit cells per crystal are found by dividing the volume of the MOF by the volume of the unit cell

$$Unit\ cells\ per\ MOF = \frac{1.56 \times 10^{10}\text{Å}^3}{8999\text{Å}^3} = 1.73 \times 10^6$$

Assuming a defect free MOF, there are 24 benzenedicarboxylate (BDC) ligands per unit cell, so the total number of BDC per MOF is

$$BDC\ ligand\ per\ MOF = 24 \times (1.73 \times 10^6) = 4.17 \times 10^7$$

The molecular formula of a UiO-66(Zr) unit cell is $Zr_{24}O_{120}C_{192}H_{96}$ which corresponds to a formula mass of 6512.12 g mol^{-1}. The molecular weight of a single UiO-66(Zr) is equal to the number of unit cells per MOF multiplied by the formula mass

$$molecular\ weight\ of\ UiO-66(Zr) = (1.73 \times 10^6) \times 6512.12 = 1.13 \times 10^{10} g\ mol^{-1}$$

With these values, it was calculated that for 10 mg of MOF the mol of BDC

$$mol\ of\ BDC = \frac{0.010g\ UiO-66}{1.13\times10^{10}g\ mol^{-1}} \times 4.17\times10^{7} = 0.037mmol$$

The ^{1}H NMR of digested UiO-66(Zr)-CTA was used to find a ratio of BDC ligand (labeled a in Figure 2S.5) the CTA (labeled b in Figure 2S.5) to the, which was 80. Therefor the moles of cat-CTA per 10mg of UiO-66(Zr) crystal is

$$\frac{0.037mmol}{80} = 0.46\mu mol$$

And the mass of cat-CTA given a molecular weight of 539.2 g mol^{-1} is

$$4.6\times10^{-7}mol \times 539.2\frac{g}{mol} = 0.25mg$$

2.5. Acknowledgements

Chapter 2, in part, is a reprint of the material, "Free-standing metal–organic framework (MOF) monolayers by self-assembly of polymer-grafted nanoparticles" *Chem. Sci.* **2020**, 11, 8433-8437. The dissertation author was the primary author of this manuscript and gratefully acknowledges the contributions of its coauthor Seth M. Cohen.

2.6. References

1. Xie, K.; Fu, Q.; Webley, P. A.; Qiao, G. G., MOF Scaffold for a High-Performance Mixed-Matrix Membrane. *Angew. Chem. Int. Ed.* **2018,** *130*, 8733-8738.

2. Kalaj, M.; Denny Jr, M. S.; Bentz, K. C.; Palomba, J. M.; Cohen, S. M., Nylon–MOF Composites through Postsynthetic Polymerization. *Angew. Chem. Int. Ed.* **2019,** *58*, 2336-2340.

3. Zhang, Y.; Feng, X.; Li, H.; Chen, Y.; Zhao, J.; Wang, S.; Wang, L.; Wang, B., Photoinduced Postsynthetic Polymerization of a Metal–Organic Framework toward a Flexible Stand-Alone Membrane. *Angew. Chem. Int. Ed.* **2015,** *54*, 4259-4263.

4. Gao, X.; Zhang, J.; Huang, K.; Zhang, J., ROMP for Metal–Organic Frameworks: An Efficient Technique toward Robust and High-Separation Performance Membranes. *ACS Appl. Mater. Interfaces* **2018,** *10*, 34640-34645.

5. Satheeshkumar, C.; Yu, H. J.; Park, H.; Kim, M.; Lee, J. S.; Seo, M., Thiol–ene photopolymerization of vinyl-functionalized metal–organic frameworks towards mixed-matrix membranes. *J. Mater. Chem. A* **2018,** *6*, 21961-21968.

6. Wang, H.; He, S.; Qin, X.; Li, C.; Li, T., Interfacial Engineering in Metal–Organic Framework-Based Mixed Matrix Membranes Using Covalently Grafted Polyimide Brushes. *J. Am. Chem. Soc.* **2018,** *140*, 17203-17210.

7. McDonald, K. A.; Feldblyum, J. I.; Koh, K.; Wong-Foy, A. G.; Matzger, A. J., Polymer@MOF@MOF: "grafting from" atom transfer radical polymerization for the synthesis of hybrid porous solids. *Chem. Commun.* **2015,** *51*, 11994-11996.

8. He, S.; Wang, H.; Zhang, C.; Zhang, S.; Yu, Y.; Lee, Y.; Li, T., A generalizable method for the construction of MOF@polymer functional composites through surface-initiated atom transfer radical polymerization. *Chem. Sci.* **2019,** *10*, 1816-1822.

9. Katayama, Y.; Kalaj, M.; Barcus, K. S.; Cohen, S. M., Self-Assembly of Metal–Organic Framework (MOF) Nanoparticle Monolayers and Free-Standing Multilayers. *J. Am. Chem. Soc.* **2019,** *141*, 20000-20003.

10. Oyeneye, O. O.; Xu, W. Z.; Charpentier, P. A., Adhesive RAFT agents for controlled polymerization of acrylamide: effect of catechol-end R groups. *RSC Adv.* **2015,** *5*, 76919-76926.

11. Bachhar, N.; Kumaraswamy, G.; Kumar, S. K., Core-Size Dispersity Dominates the Self-Assembly of Polymer-Grafted Nanoparticles in Solution. *Macromolecules* **2019,** *52*, 4888-4894.

12. Zhang, S. L.; Guan, B. Y.; Wu, H. B.; Lou, X. W. D., Metal–Organic Framework-Assisted Synthesis of Compact Fe2O3 Nanotubes in Co3O4 Host with Enhanced Lithium Storage Properties. *Nano-Micro Lett.* **2018,** *10*, 44.

13. Kalaj, M.; Palomba, J. M.; Bentz, K. C.; Cohen, S. M., Multiple functional groups in UiO-66 improve chemical warfare agent simulant degradation. *Chem. Commun.* **2019,** *55*, 5367-5370.

14. Zhu, W.; Xiang, G.; Shang, J.; Guo, J.; Motevalli, B.; Durfee, P.; Agola, J. O.; Coker, E. N.; Brinker, C. J., Versatile Surface Functionalization of Metal–Organic Frameworks through Direct Metal Coordination with a Phenolic Lipid Enables Diverse Applications. *Adv. Funct. Mater.* **2018,** *28*, 1705274.

15. Pyun, J.; Kowalewski, T.; Matyjaszewski, K., Synthesis of Polymer Brushes Using Atom Transfer Radical Polymerization. *Macromol. Rapid Commun.* **2003,** *24*, 1043-1059.

16. Horcajada, P.; Salles, F.; Wuttke, S.; Devic, T.; Heurtaux, D.; Maurin, G.; Vimont, A.; Daturi, M.; David, O.; Magnier, E.; Stock, N.; Filinchuk, Y.; Popov, D.; Riekel, C.; Férey, G.; Serre, C., How Linker's Modification Controls Swelling Properties of Highly Flexible Iron(III) Dicarboxylates MIL-88. *J. Am. Chem. Soc.* **2011,** *133*, 17839-17847.

17. Ma, M.; Bétard, A.; Weber, I.; Al-Hokbany, N. S.; Fischer, R. A.; Metzler-Nolte, N., Iron-Based Metal–Organic Frameworks MIL-88B and NH2-MIL-88B: High Quality Microwave Synthesis and Solvent-Induced Lattice "Breathing". *Cryst. Growth Des.* **2013,** *13*, 2286-2291.

Chapter 3: The Influence of Polymer Characteristics on the Self-Assembly of Polymer-Grafted MOF Particles

3.1 Introduction

Following the successful development of SI-RAFT as a method to prepare polymer-grafted MOFs in Chapter 2, the parameters that governed the self-assembly of MOF-polymer particles was further investigated. As described in Chapter 1, several factors can determine the physical properties of polymer-grafted particles. Specifically, the conformation of the polymer brush on the surface plays a significant role. In Chapter 2, the effect of polymer molecular weight on the mechanical properties of the SAMMs was clearly delineated, and high molecular weight polymers were needed to form free-standing membranes. However, it was not determined how closely packed the polymer chains were (i.e., the grafting density). It was hypothesized that determining and controlling grafting density could be instrumental in fabricating more robust SAMMs. Furthermore, the SAMMs exclusively used poly(methyl methacrylate), neglecting the potential influence that polymers with different bulk physical properties could have. Finally, the failure of the UiO-66-NH_2 particles to form free-standing monolayers was surprising, as these particles had polymer grafts of similar molecular weight to free-standing UiO-66. It was hypothesized that the smaller particle size of UiO-66-NH_2 had contributed to mechanical failure. In summary, it appeared that molecular weight alone could not account for the results observed in Chapter 2, and a systematic study was needed to fully explore this system.

Chapter 3 describes an in-depth, systematic investigation of polymer-grafted MOF self-assembly. Three different particle sizes of UiO-66 octahedron were prepared at 80 nm, 120 nm, and 250 nm edge length. For each size of MOF particle, three different vinyl polymers─poly(methyl methacrylate) (pMMA), poly(benzyl methacrylate) (pBnMA), and poly(methyl acrylate) (pMA)─were polymerized from the surface at different molecular weights. Each MOF–polymer combination was then self-assembled at an air–water interface to more

thoroughly understand the multi-scale interactions that contribute to the success and failure of achieving free-standing SAMMs and the factors that govern the properties of these materials more broadly. Concurrently, molecular dynamics (MD) simulations using a coarse-grained (CG) model were used for elucidating the roles of polymer grafting and particle size in dictating the orientation and translational order of MOF particles in the assembled SAMMs.

3.2 Results and Discussion

The synthesis of MOFs on a large scale while simultaneously controlling the size, polydispersity, and morphology remains a significant challenge. For this study, a large-scale continuous-feed method introduced by Wang et al.[1] was used, which afforded multi-gram quantities of UiO-66 in three distinct size regimes, termed UiO-66$_x$ (x = the particle edge length in nm measured by scanning-electron microscopy, SEM) (Figure 3.1, Figure 3S.1). Powder X-ray diffraction (PXRD) of the three sizes of UiO-66 showed the MOFs exhibited good crystallinity (Figure 3.1). Nitrogen adsorption isotherms of the MOF particles were in good agreement with literature reports (Figure 3S.2).[2]

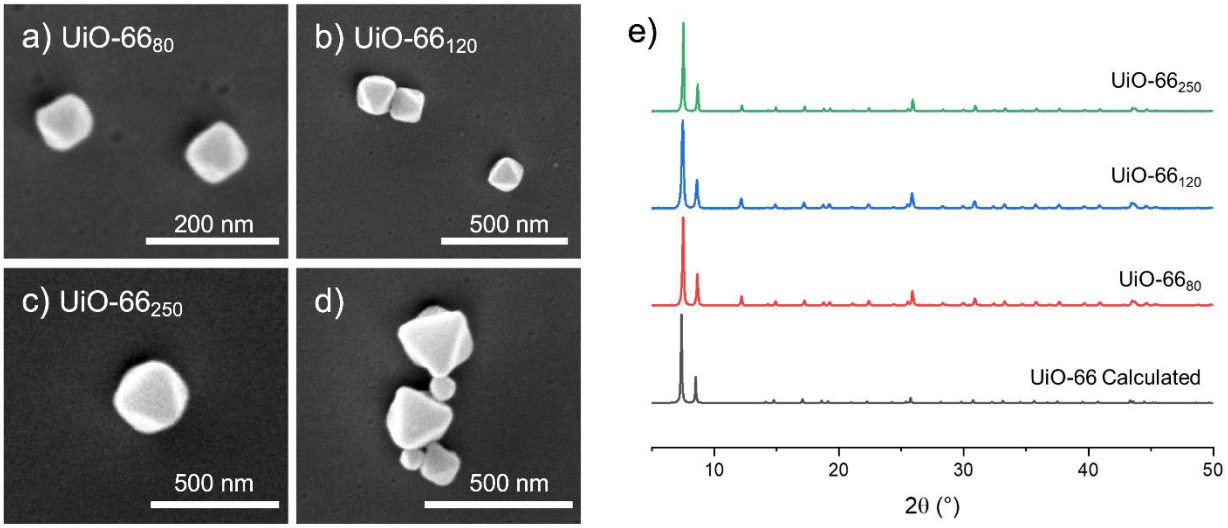

Figure 3.1. SEM images and PXRD of synthesized MOFs: (a) UiO-66$_{80}$, (b) UiO-66$_{120}$, (c) UiO-66$_{250}$, and (d) mixture of all three MOFs displaying relative particle size (scale bars are 200 or 500 nm, as indicated). (e) Calculated and experimental PXRD patterns for MOF particles.

Control over the polymerization of different monomers using RAFT is dependent on the structure of the CTA with respect to monomer structure.[3] To ensure control over a wide variety of monomers, two CTAs, 2-(dodecylthiocarbonothioylthio)-2-methylpropionic acid (DDMAT) and 4-cyano-4-[(dodecylsulfanylthiocarbonyl)sulfanyl]pentanoic acid (CDSPA), were used in this study. In Chapter 2, CDSPA was used to prepare cat-CTA which allowed for the controlled RAFT polymerization of methacrylates. However, CDSPA does not have a high enough reactivity to initiate acrylates for polymerization. By replacing the cyano- group of CDSPA with the carbonyl group of DDMAT, the reactivity is increased enough to ensure rapid initiation is achieved with acrylates. For each CTA, a catechol group was introduced via the reaction of dopamine with the activated ester form of the CTA (Schemes 3S.1 and 3S.2). Surface functionalization of the MOF particles was performed using a biphasic mixture of an aqueous suspension of MOF particles in 10 mL water (20 mg/mL) and the CTA in 5 mL of chloroform (1 mg/mL) as previously reported (Scheme 3S.3).[4] Briefly, the aqueous and organic solutions were combined in a 50 mL centrifuge

tube and vigorously mixed for 5 min using a vortex mixer to ensure adequate interfacial contact between the two solutions. The emulsion was broken with ethanol and the particles were collected by centrifugation. The solids were resuspended in ethanol and solvent exchanged by repeated centrifugation/dispersion cycles in ethanol, then solvent exchanged into DMSO to a final concentration of 80 mg/mL for further polymerization. After functionalization the MOF particles possess an orange/yellow color indicative of the presence of the CTA agent (Figure 3S.3). Determination of the amount of CTA present on the surface of the MOF particles was attempted with several methods typically used for inorganic nanoparticles (e.g., ^{1}H NMR, TGA, UV-vis). However, these methods proved ineffective for quantifying the CTA coverage due to the large excess of the terephthalic acid ligand (H_2bdc) originating from the MOF. The UV-vis absorbance of the CTA at 300 nm overlapped completely with the absorbance from H_2bdc, and TGA did not show a distinct mass loss between unfunctionalized and functionalized MOF particles. While ^{1}H NMR of digested MOF particles could resolve the presence of the long alkyl chain of the CTA, the exact quantity of CTA present could not be determined with confidence.

To analyze the effect of the polymer backbone and side-chain effects on self-assembly, we chose poly(methyl methacrylate) (pMMA), poly(benzyl methacrylate) (pBnMA), and poly(methyl acrylate) (pMA) as polymers with different physical properties. The polymer graft was synthesized by surface-initiated photoinduced electron transfer reversible addition-fragmentation chain transfer polymerization (SI-PET-RAFT) using $Ir(ppy)_3$ as the photocatalyst under blue LED lights (Scheme 3.1, Figure 3S.4). Free, unbound CTA without the anchoring catechol group was included in each polymerization to ensure efficient chain transfer and control from the surface.[5] While the amount of CTA bound to the surface was unknown, this excess of free CTA was used to ensure that the polymerization on the surface is controlled regardless of the amount of surface

CTA present. For acrylates, the same DDMAT CTA was used on both the surface (cat-DDMAT) and in solution (Scheme 3S.4). However, better control was achieved in the polymerization of methacrylates when 4-cyano-4-(phenylcarbonothioylthio)pentanoic acid (CPADB) was used as the free CTA in solution instead of CDSPA due to the higher transfer constant of the former (Scheme 3S.5 and 3S.6).[3] To check the effect of the MOF on the polymerization itself, a control experiment using methyl acrylate as the monomer was performed without MOF, with unfunctionalized UiO-66_{120}, and DDMAT functionalized UiO-66_{120}. Analysis of the free polymer shows that the presence of UiO-66 does not have a large effect on the polymerization (Table 3S.2).

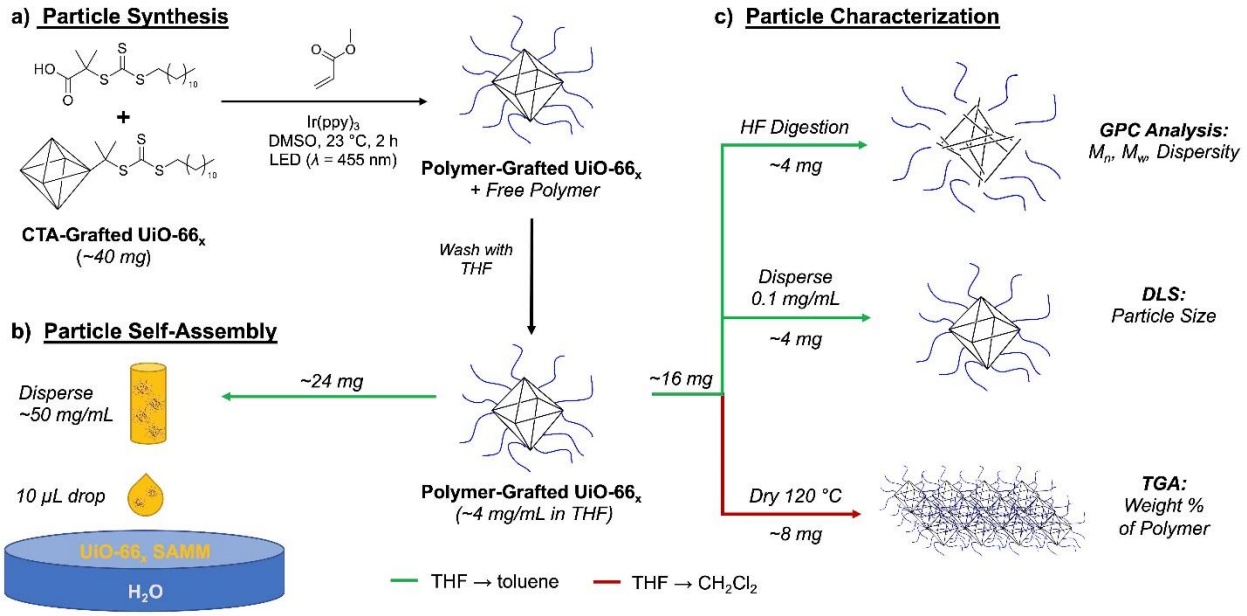

Scheme 3.1. Workflow for synthesis and characterization of polymer-grafted MOF particles and the resulting self-assembled MOF monolayers (SAMMs) using UiO-66_x-MA_n as an example. (a) Synthesis of polymer-grafted MOF particles via surface-initiated photoinduced electron-transfer reversible addition–fragmentation chain-transfer polymerization (SI-PET-RAFT). (b) Self-assembly of particle monolayers at an air–water interface. (c) Characterization of particles via GPC, DLS, and TGA. Green and red arrows indicate solvent changes from THF to toluene and CH_2Cl_2, respectively.

Each MOF/polymer combination was polymerized to different molecular weights to see how the length of the polymer chain relative to particle size affected the particle self-assembly and physical properties of the monolayer (Table 3S.1). After polymerization, the particles were separated from ungrafted (e.g., free in solution) polymer via five cycles of centrifugation, decanting, and redispersion in THF. A small sample of the particles was removed for characterization while the remaining particles were solvent exchanged into toluene for self-assembly at an air-water interface (Scheme 3.1). The molecular weight of the surface-bound polymer was characterized by digesting the polymer-grafted MOF in HF/toluene followed by gel-permeation chromatography (GPC), while thermogravimetric analysis (TGA) was used to calculate the weight percent of the polymer relative to MOF.

The porous and organic-inorganic nature of the MOF adds some complexity to the TGA analysis, and three distinct regimes of mass loss occur from 0-600 °C (Figure 3.2). The initial mass loss is due to the evaporation of solvent from the MOF pores while the mass loss from 280 to 420 °C and 420 to 600 °C correspond to the degradation of the polymer and MOF, respectively. The remaining mass is residual ZrO, and by comparing these values the amount of polymer relative to MOF can be determined.

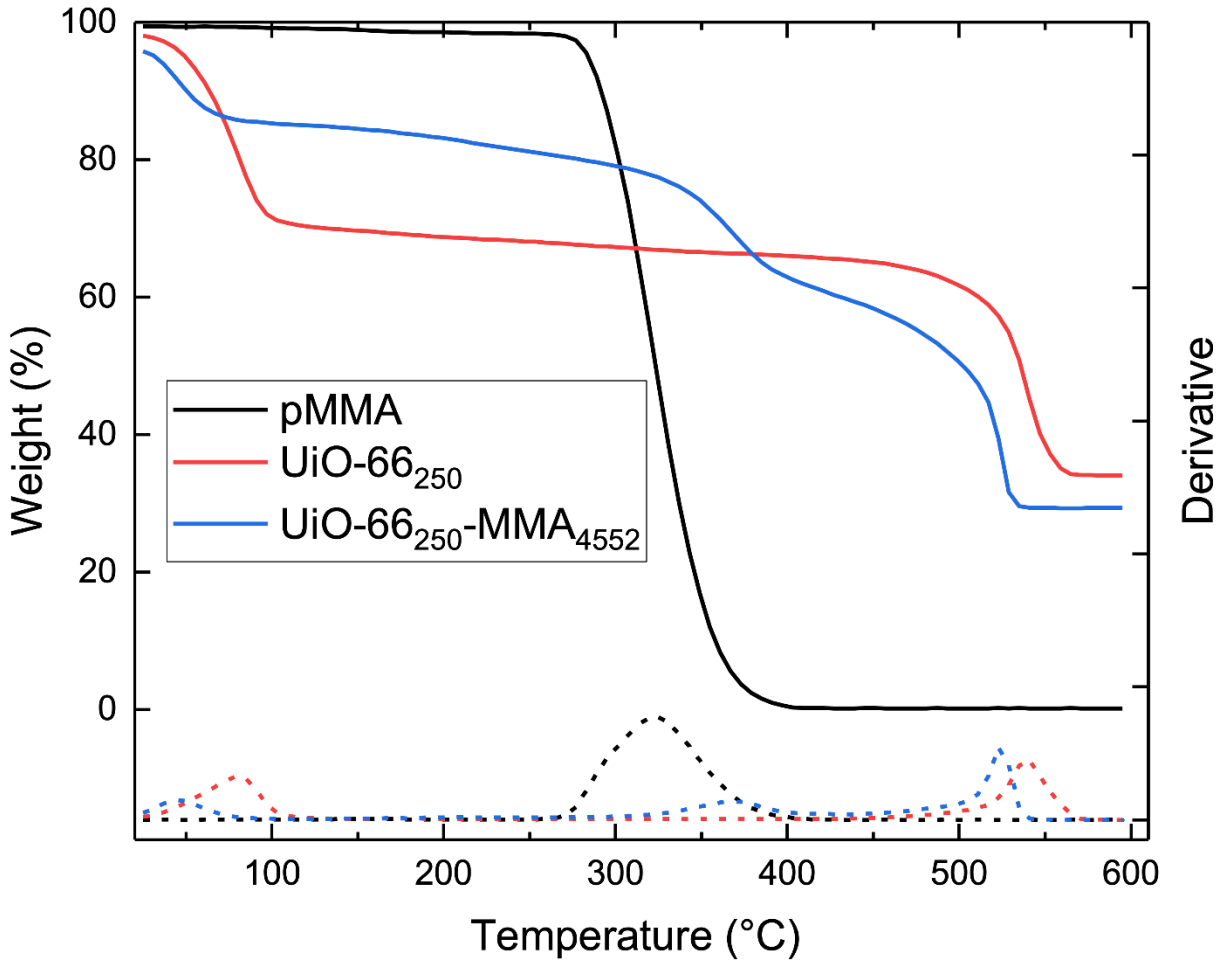

Figure 3.2. Representative TGA plot of weight percent (solid lines, left *y*-axis) and derivative of weight percent (dashed lines, right *y*-axis) for pMMA (black), UiO-66_{250} (red), and UiO-66_{250}-MMA_{4552} (blue).

With the molecular weight and relative mass of the polymer obtained by GPC and TGA, respectively, the grafting density on the surface of the MOF can be estimated by the following equation:

$$\sigma = \frac{w_{\mathrm{p}} N_{\mathrm{A}} \rho_{\mathrm{MOF}} a}{4.85 w_{\mathrm{MOF}} M_{\mathrm{n}}}$$

where w_{p} is the weight fraction of the polymer and w_{MOF} is the weight fraction of MOF as determined by TGA, N_{A} is Avogadro's number, ρ_{MOF} is the density of UiO-66, a is the edge length of the octahedron, and M_{n} is the molecular weight of the surface-grafted polymer.[6] The grafting

density of each sample are shown in Table 3S.1. The brush height of the polymer grafts was determined by subtracting the radius of the core particle, r_0, from the radius of the polymer-grafted MOF nanoparticle (PGMN) obtained by dynamic light scattering (DLS) of the particles in toluene. It should be noted that the size measured by DLS (Figure 3.3) is representative of a sphere with equivalent Brownian motion, which does not account for the octahedral shape of the MOF particles.[7] To simplify the calculations, a sphere of intermediate radius to the MOF particle was assumed as the core radius and subtracted from the radius determined by DLS to get the brush height, *h* (see ESI for a detailed explanation, Figure 3S.5).

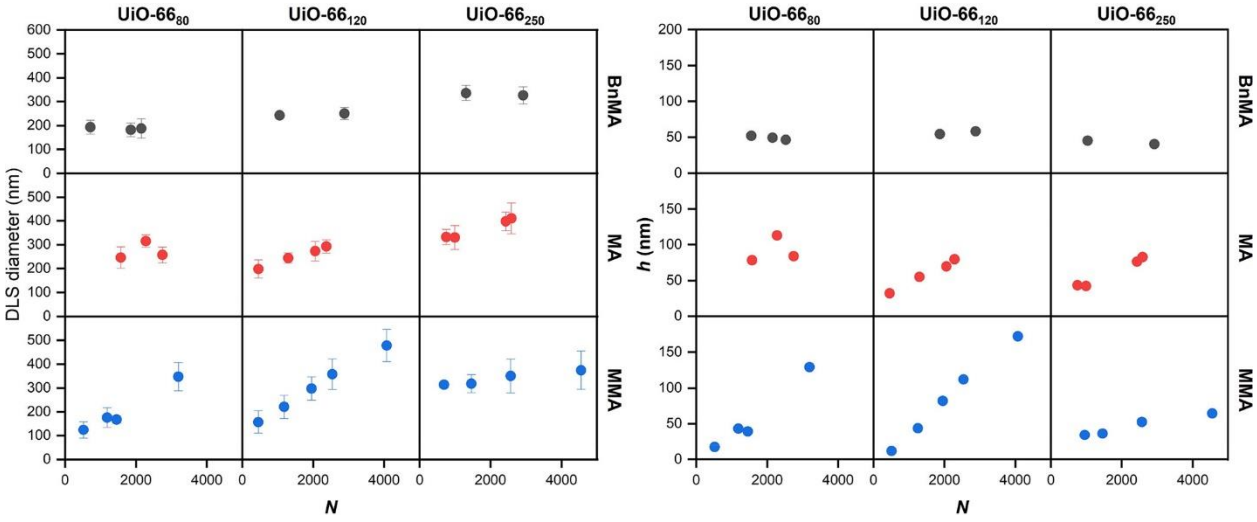

Figure 3.3. Left: Particle diameter as characterized by dynamic light scattering (DLS) in toluene with respect to the surface polymer length as determined by gel permeation chromatography (GPC). Error bars are the standard deviation of three independent measurements. Right: Relationship of the polymer brush height (*h*) determined by DLS as a function of increasing polymer length (*N*). Columns designate the size of the MOF particle and rows designate the monomer used. Each point is the average of three independent DLS measurements.

The brush height, *h*, as a function of degree of polymerization, *N*, shows different scaling depending on the size of the MOF and the grafted polymer (Figure 3.3). In the case of UiO-66$_x$-BnMA$_n$, the samples show no change in brush height at any values of *N*, whereas UiO-66$_x$-MMA$_n$

and UiO-66$_x$-MA$_n$ show a linear increase in all cases excluding UiO-66$_{80}$-MA$_n$. These results are shown primarily to illustrate the potential of these combined methods to analyze the polymer graft on a MOF surface beyond simple molecular weight characterization, as clear variations can occur between samples with similar *N*. However, the current data set is not sufficient to develop a robust physical model of the polymer microstructure across all the different variables, and more data is needed to comprehensively understand how these MOF-polymer brush materials compare to other polymer grafted nanoparticle systems.

The self-assembly of the polymer-grafted MOF particles into SAMMs was investigated. The self-assembly at the air-water interface was performed by adding a 10 µL drop of a 10 wt% suspension of the polymer-grafted MOF particles in toluene to a layer of water in a plastic Petri dish (diameter = 55 mm). The drop immediately spread to the edge of the dish and was quickly covered with a lid to prevent disturbance from the evaporation process and air turbulence. After 10 min the lid was removed, revealing an iridescent film. The monolayer was then suspended on a 7 mm loop of copper wire, which held a drop of water supporting the monolayer (Scheme 3S.7). The wire loop was then suspended to air dry, after which the film either broke or remained suspended as a free-standing monolayer.

As previously reported, polymer-grafted MOFs with low molecular weight ($N < 1000$) gave monolayers with poor mechanical properties and easily fractured when disturbed. Depending on the polymer used, as MW was increased further the monolayers began to behave more like polymeric films, with large areas of the film responding to localized stress indicating a significant level of entanglement between the particles. Films formed from poly(benzyl methacrylate) (pBnMA) or poly(methyl methacrylate) (pMMA) were brittle and easily fractured when disturbed. Of these two polymers, only pMMA was able to form free-standing membranes at higher

molecular weights ($N > 4000$). However, when the polymer was changed to pMA, a significant difference in membrane forming behavior was observed. For $N > 1000$ with pMA, the monolayer films were extremely tough and flexible, exhibiting none of the brittleness of pMMA. The monolayers formed from polymer-grafted MOFs with pMA were strong enough that removal of sections of the films for SEM imaging was nearly impossible, with the entire film delaminating from the water surface.

To understand the origin of these pronounced differences in film properties with varying polymer type and length, sections of each monolayer were transferred from the water surface to a glass coverslip for SEM imaging (Figure 3.4, Figures 3S.6-3S.8). In the case of UiO-66_{80}-MMA_n, the presence of polymer coating on the exterior of the particles is visible for UiO-66_{80}-MMA_{1453}, but the loose packing indicates that the chains fail to entangle enough to prevent separation (Figure 3.4c, Figure 3S.6). At a comparable molecular weight, UiO-66_{250}-MMA_{1460} shows little visible polymer present on the surface (Figure 3.4h). At $N > 4000$, densely packed films form for UiO-66_{120} and the polymer brushes are clearly entangled enough between particles to show distinct crazing as cracks form through the material (Figure 3.4f,i). However, only UiO-66_{120}-MMA_{4071} remained a free-standing membrane while the UiO-66_{250}-MMA_{4452} monolayer fractured. As both particles have similar polymer lengths and grafting densities, this effect is presumed to be a result of the significantly larger particle size for UiO-66_{250}-MMA_{4452}. The larger particle size results in larger gaps between MOFs that the polymer chains must bridge to hold the particles together, and the chains are not able to form substantial entanglements across these interstitial spaces for UiO-66_{250}-MMA_{4452}. We also observed that as the MOFs become smaller or are grafted with longer chains, the particles lose some of their translational and orientational order in the films (for instance, compare Figure 3.4d with 3.4f). As the MOF particles become smaller, it is more

challenging to obtain uniformly sized particles (compare Figure 3.4a with 3.4g), which could also contribute to some loss in order. Even if the absolute variations were the same across all particle sizes, the small particles will exhibit larger *relative* variations in size (the primary factor dictating their ordering) compared to large particles. We also noted some rounding off at the vertices of the MOF particles. Because the relative effect of curvature is stronger on smaller particles than on larger ones (even if the absolute curvature was the same), this effect could also contribute to the increasing disorder with decreasing particle size.

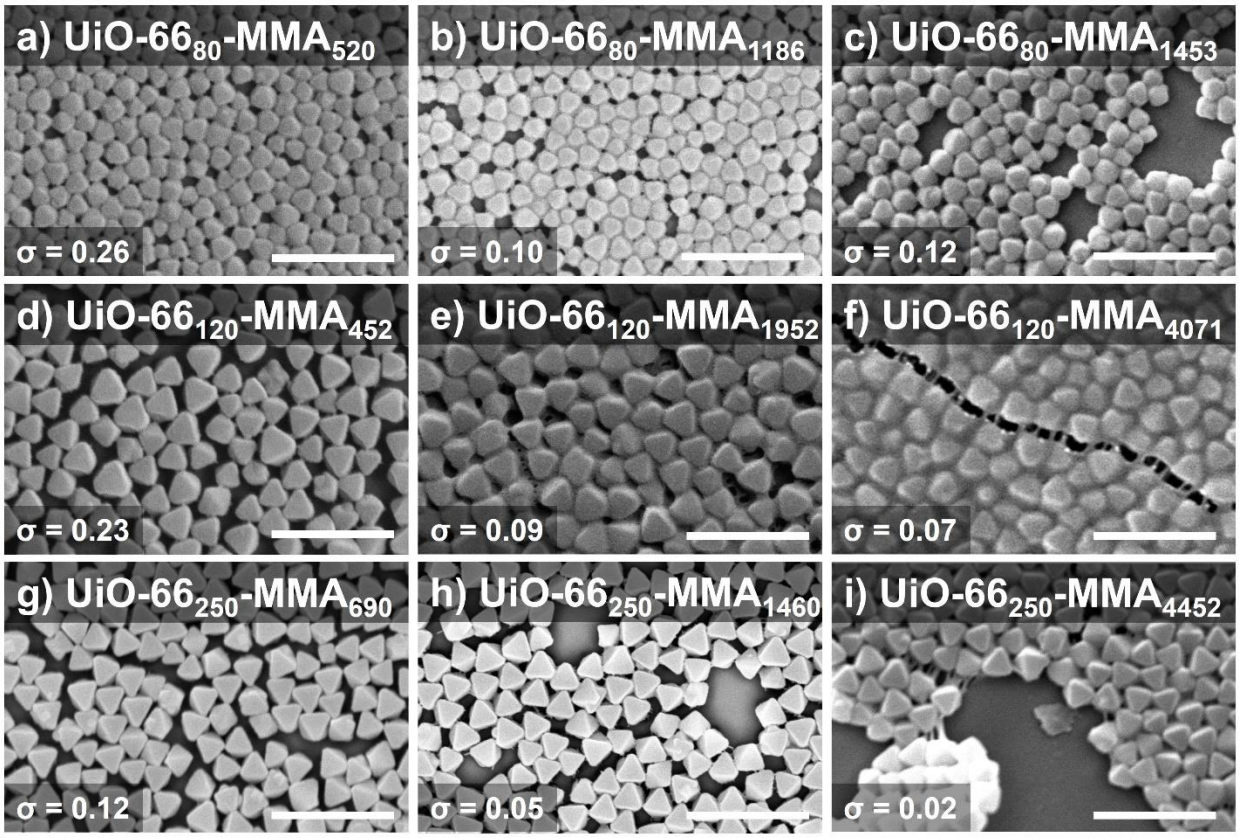

Figure 3.4. SEM images of SAMMs with pMMA. (a–c) UiO-66$_{80}$-MMA$_n$ (scale bars 500 nm). (d–f) UiO-66$_{120}$-MMA$_n$ (scale bars 500 nm). (g, h) UiO-66$_{250}$-MMA$_n$ (scale bars, 1 μm). Grafting density values (σ) are shown.

Compared to UiO-66$_x$-MMA$_n$, images of the highly ductile UiO-66$_x$-MA$_n$ monolayers showed significant polymer entanglement at much lower molecular weights (Figure 3S.7). Free-standing films were achieved for all monolayers with $N > 1000$ regardless of particle size, indicating the mechanism for this improved mechanical strength is not a result of simply increasing molecular weight to a higher value. The grafting density and brush height are both higher at comparable molecular weights to the MMA grafts. It is not obvious what leads to the higher initial graft density in the MA polymerization as the graft density of initiator should be the same. One possible explanation is the acrylate polymerization in this particular system provides better control than methyl methacrylate.[8] This would lead to more uniform growth at the initial stages of polymerization forming a dense brush at low molecular weights until steric crowding begins to prevent activation-deactivation by the CTA. This higher grafting density forces the polymer chains to extend further from the surface. As molecular weight increases, the increased grafting density results in more entanglements per particle, which prevents the SAMM from cracking during the drying process resulting in a highly interconnected, flexible film. SEM images of the delaminated film show that the fiber formed is comprised from a single monolayer twisted and folded into itself (Figure 3.5a-e).

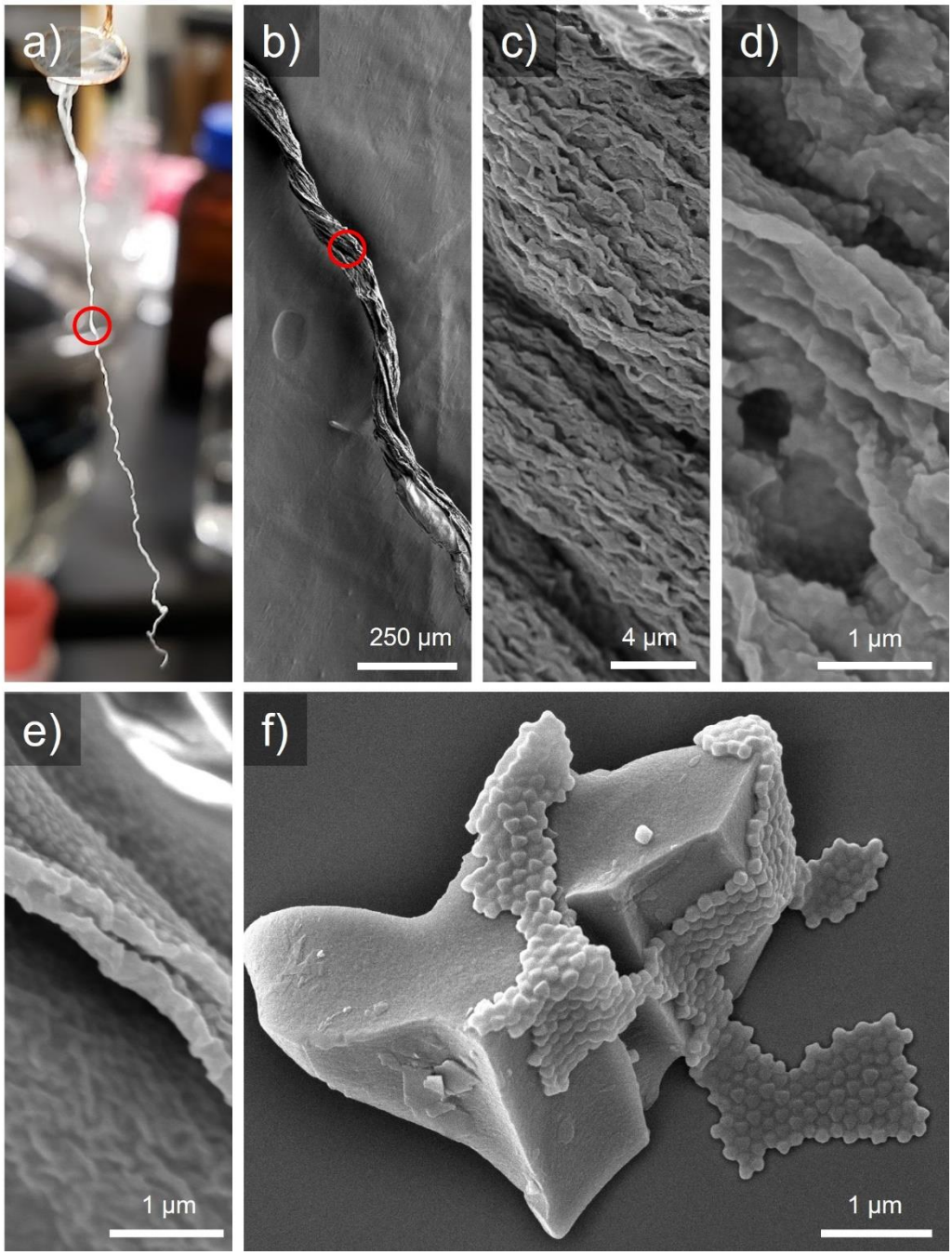

Figure 3.5. (a) Delaminated monolayer of UiO-66_{120}-MA_{1294} in dry fiber form. (b–e) SEM images of fiber at increasing magnification. (f) SEM of monolayer on small glass fragment (irregular shaped solid particle) showing ability to conform to various surface curvatures while retaining ordered monolayer.

This macroscopic flexibility extends to the microscale as well, with SEM images of the monolayer on a small glass fragment showing the film can tightly adhere to both convex and

concave surfaces of high curvature without breaking the ordered monolayer structure (Figure 3.5f). These results are encouraging when considering future applications, as the films can be applied to a wide variety of substrates with rough surface features without compromising the monolayer.

As a representative example of the polymer-coated MOF particles, the accessible surface area of UiO-66_{250}-MMA_{2566} was measured using N_2 gas. The BET surface area of UiO-66_{250}-MMA_{2566} was determined to be 885 m^2/g; by comparison, the unmodified UiO-66_{250} material gave a surface area of 1442 m^2/g (Figure 3S.9). TGA shows UiO-66_{250}-MMA_{2566} is 20% polymer by mass (Table S1); therefore, the expected surface area of UiO-66_{250}-MMA_{2566} based on the weight percent of the MOF and the surface area of the unmodified particles (80% of 1442 m^2/g) is ~1150 m^2/g. This data suggest that UiO-66_{250}-MMA_{2566} retains ~75% of the expected surface area.

To understand the observed changes in the orientational and translational order of MOFs with respect to their size, graft type, and MW, coarse-grained molecular dynamics (CG MD) simulations of the MOF–air–water system were performed (Figure 3.6). Analogous to the experiments, the effects of varying MOF edge length L_{MOF}, graft length L_g, and graft hydrophobicity λ were examined. As detailed below, the parameter λ describes the relative strength of polymer–solvent to solvent–solvent interactions, where $\lambda = 0$ indicates strongly hydrophobic chains and $\lambda = 1$ indicates strongly hydrophilic chains.

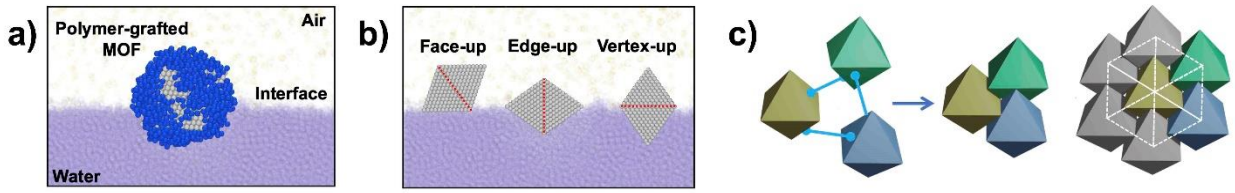

Figure 3.6. Modeling and simulation of MOF orientation and assembly at an interface. (a) Simulation setup showing the coarse-grained model of polymer-grafted MOF trapped at an air–water interface. (b) Side view of the three idealized orientations of MOFs shown without the grafts. Red dotted lines represent the square base of a regular octahedron. (c) Schematic illustrating the formation of face-to-face contacts between MOFs leading to hexagonal packing (highlighted by white dotted lines).

First, the orientation of *individual* MOFs at the interface (Figure 3.7, insets) were examined, which were classified as "face-up", "edge-up", or "vertex-up" based on the interface-projected areas of the MOFs (Figure 3.6b, Figure 3S.10). Based on energetic arguments, octahedral particles that interact similarly with fluids on both sides of the interface should reside symmetrically about the interfacial plane and adopt a vertex-up orientation, which maximizes the occluded area of the energetically unfavorable interface.[9-10] Indeed, we find that MOFs with moderately hydrophilic grafts stay close to the interfacial plane and exhibit vertex-up orientation (labelled VI, Figure 3.7). Similarly, MOFs with short hydrophobic grafts, where the hydrophilic surface of the MOF balances out the hydrophobicity of the grafts, also reside close to the interface and exhibit vertex-up orientation (I, VIII–X, Figure 3.7). However, as the grafts become more hydrophobic and long enough to screen out favorable MOF-water interactions (II, III, V, Figure 3.7), the MOFs shift from the water to the air phase and exhibit face-up orientation, thereby maximizing the occluded area of the interface while minimizing the unfavorable graft-water interactions. Interestingly, when the grafts become very long, the MOFs almost completely detach from the water phase and begin to exhibit vertex-up orientation (IV, Figure 3.7). This configuration best avoids contact between the grafts and the water phase, as the grafts are generally

depleted at the MOF tips. On the other hand, strongly hydrophilic grafts cause the particles to fully submerge into the water phase and adopt the edge-up orientation (VII, Figure 3.7), which allows some area of the interface to be occluded while maximizing favorable graft-water interactions.

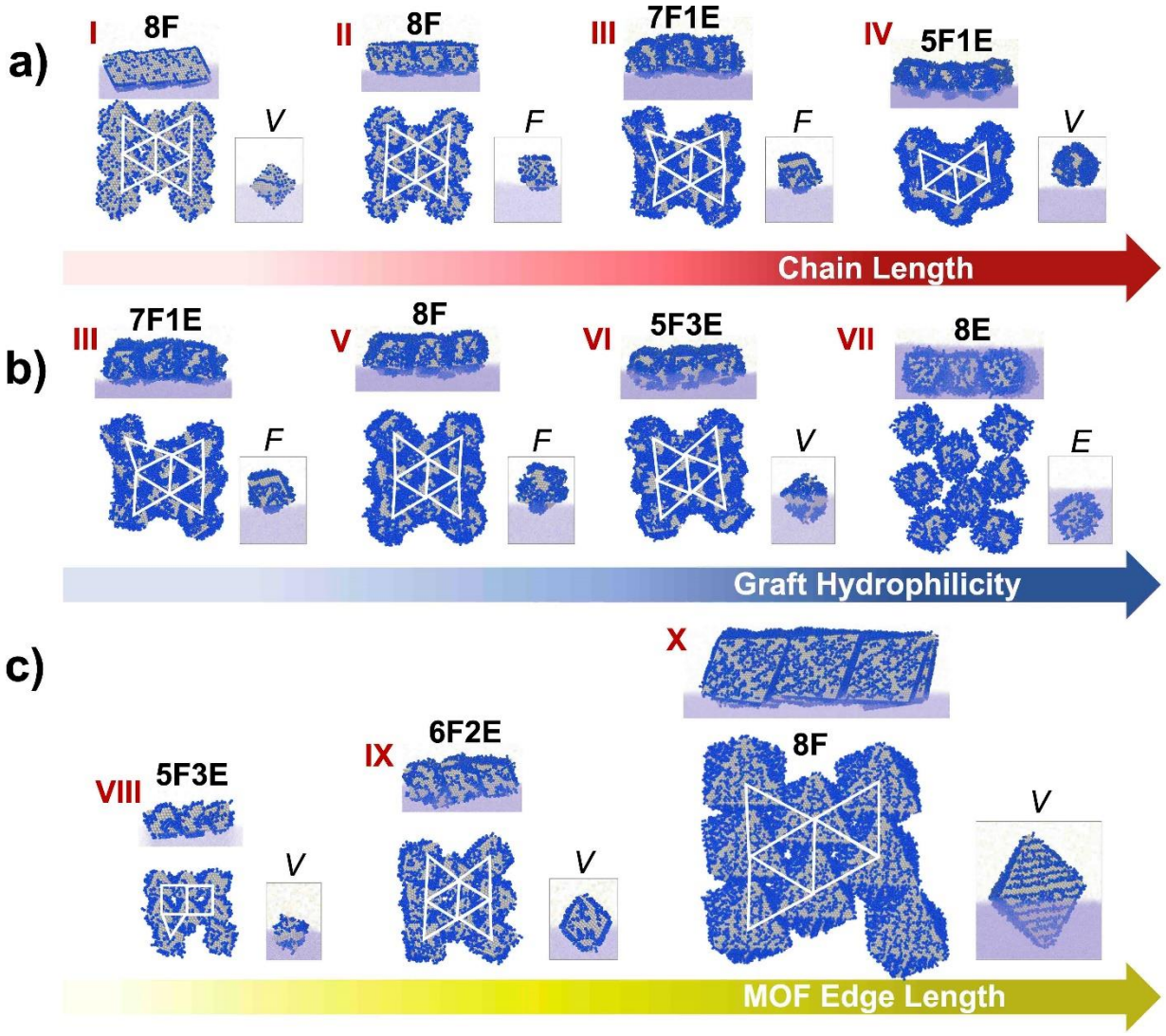

Figure 3.7. MOF orientation and assembly predicted by simulations. Side and top views of structures assembled with MOFs of increasing (a) graft lengths L_g = 1σ_{CG}, 2σ_{CG}, 4σ_{CG}, and 6σ_{CG} for fixed MOF size L_{MOF} = 13σ_{CG} and graft hydrophilicity λ = 0.2, where σ_{CG} is the basic length scale in our coarse-grained model; (b) hydrophilicity of graft monomers λ = 0.2, 0.4, 0.6, and 1 for fixed MOF size L_{MOF} = 13σ_{CG} and graft length L_g = 4; and (c) edge length L_{MOF} = 9σ_{CG}, 13σ_{CG}, and 28σ_{CG} for fixed L_g = 2σ_{CG}, λ = 0.4. Insets show the orientation adopted by a single, isolated MOF particle (E = "edge-up"; F = "face-up"; V = "vertex-up"). The orientations adopted by each MOF particle in the assembled structure were enumerated and indicated as *x*F*y*E (*x* and *y* are integers), shown immediately above each structure. White triangles highlight the hexagonal packing of particles.

Next, the assembly of *multiple* MOF particles was examined at the interface. Our simulations revealed that the MOFs assembled primarily via face-face contacts (Figure 3.7),

leading to the hexagonal packing observed in the experiments. Interestingly, many of the assembled structures were composed of face-up oriented MOFs, even when they preferred to be vertex-up or edge-up in isolation (I, IV, VI, VIII–X, Figure 3.7). This can be explained by the large free energy gained from face-to-face contacts enabled by the face-up orientation of the MOFs, which compensates for the loss in free energy due to reorientation (Figure 3.6b); if the MOFs had remained vertex-up, the free energy gained from tip-tip contacts would be small due to the small area of interactions.[10] This finding is also consistent with our previous study on polymer-grafted nanocubes.[11] With this ability to mediate face-to-face contacts, a single MOF can mediate interactions (via its six lateral facets) with six adjacent MOFs, leading to the observed hexagonal packing arrangement of the MOFs. Importantly, these results also suggest that interparticle interactions must be very strong in these MOF systems, prevailing over interfacial interactions that would otherwise have led to assemblies with different orientations.

The degree of hexagonal ordering of MOFs and homogeneity of their orientation in the self-assembled structures depended strongly on the graft length, their hydrophilicity, and particle size. In general, we found that as the grafts became longer, the interparticle distance increased, and the MOFs lost their octahedral character, leading to more disordered packing (Figure 3.7a). This finding is consistent with our experimental observations (for an example, see UiO-66_{250}-MA_n, Figure 3S.11). Decreasing the hydrophobicity of the grafts also led to more disordered packing, and eventually no assembly at all for highly hydrophilic grafts, which were strongly wetted by the surrounding water molecules (Figure 3.7b). Lastly, increasing the MOF size led to more uniform orientations (face-up) and packing (hexagonal) of the MOFs (Figure 3.7c), also consistent with our experiments when using benzyl methacrylate (Figure 3S.10). The assemblies with the smallest MOFs considered here (UiO-66_{80}-$BnMA_{715}$) exhibited large fluctuations in particle orientation and

a more square-like rather than hexagonal order, whereas those with the largest MOFs (UiO-66_{250}-$BnMA_{1309}$) exhibited hexagonal ordering with uniformly face-up particles (Figure 3S.12). Interestingly, we observed that the hexagonal order appeared before orientational order as the size of the MOFs was increased. Overall, our simulations suggest that the polymer grafts need to be sufficiently short relative to the particle size and sufficiently hydrophobic to exhibit orientational and translational order, which is in contrast to those found to promote assembly of robust SAMMs at the air-water interface.

3.3 Conclusion

UiO-66 octahedral nanoparticles were prepared in three distinct size regimes and functionalized with pMMA, pBnMA, and pMA via a grafting-from approach using a SI-PET-RAFT polymerization procedure. The effects of particle size, polymer type, and polymer length at an intermediate grafting density ($\sigma \approx 0.02 – 0.2$ chains/nm) were explored with respect to the physical properties of the self-assembled monolayers. Increasing polymer length led to increased interparticle chain entanglements and significant improvements in the physical stability of the resulting monolayers, with diminishing improvements as particle size increases. Switching from pMMA to pMA, significantly altered the properties of the monolayers to reflect the bulk polymer, with glassy pMMA grafts giving more brittle monolayers and rubbery pMA grafts producing tough, flexible films. Free-standing monolayers were easier to achieve at an intermediate particle size (120 nm) and the ideal combination of factors for mechanically robust SAMMs was found using intermediate 120 nm particles grafted with high M_n pMA. Simulations provided additional insights into the orientation and ordering of MOFs within the films as a function of particle size,

graft length, and hydrophobicity. These polymer-grafted, self-assembling MOF particles may find further application in ultrathin membranes for separations, protective coatings, and optical films.

While several characterization methods were developed for this system, quantification of the amount of CTA on the particle after functionalization and before polymerization proved to be surprisingly non-trivial. The weight percent of polymer relative to MOF was determined by TGA, but the relatively low molecular weight of the CTA prevented accurate analysis. It was assumed that the yellow color of the CTA would allow accurate determination by UV-vis measurements of the particles after digestion. Unfortunately, the weak absorbance of the CTA in the visible region was undetectable at such low concentrations. However, if the CTA was exchanged for a molecule with much higher absorptivity in the visible region, then the amount of dye could be accurately measured. This value could then be used as approximate measurement for the amount of CTA on the surface. More broadly, this could prove to be an accurate measurement of MOF surface coordination and functionalization in general. Chapter 4 explores this idea in detail, demonstrating that the coordination of dye molecules to the surface of MOFs functions as a simple methodology to analyze surface functionalization.

3.4 Appendix: Supporting Information

Materials and Methods

All starting materials and reagents were purchased from Sigma-Aldrich and used without further purification unless otherwise specified. Dimethyl sulfoxide (DMSO, 99.7% extra dry) was purchased from Acros. Methyl methacrylate (MMA), methyl acrylate (MA), and benzyl methacrylate were purified by passing through a column filled with basic alumina (Sorbtech) to remove inhibitor and stored at 8 °C. Chain transfer agents (CTAs) 4-cyano-4-

[(dodecylsulfanylthiocarbonyl)sulfanyl]pentanoic acid (CDSPA), 2-(dodecylthiocarbonothioylthio)-2-methylpropionic acid (DDMAT), and 4-cyano-4-(phenylcarbonothioylthio)pentanoic acid (CPADB) were purchased from Sigma-Aldrich and used as received. Blue LED light strips for the homemade photoreactor were purchased from ALITOVE, model 5050 Blue LED Flexible Strip Ribbon and powered using a 12V power adapter. The photoreactor was made from a thin-walled aluminum can (diameter = 16 cm) and the interior was wrapped with 50 cm of the LED strip (see Figure S3). Peristaltic pumps were purchased from New Era Pump Systems (Model 9000B).

Characterization

Nuclear Magnetic Resonance. Proton nuclear magnetic resonance spectra (^{1}H NMR) were recorded on a JEOL ECA 500 spectrometer (500 MHz). Chemical shifts are reported in parts per million (ppm) referenced to the appropriate solvent peak.

Gel Permeation Chromatography (GPC). Gel permeation chromatography (GPC) was performed in THF at 30 °C with a flow rate of 0.5 mL/min using an Agilent 1260 HPLC with diode array, Wyatt DAWN HELEOS 8+ multiangle laser light scattering detector (MALS) with light wavelength at 690 nm, Viscostar III viscometer, and Optilab TrEX refractive index. Absolute molecular weights were determined using ASTRA software from Wyatt Technology.

Powder X-Ray Diffraction (PXRD). ~50 mg of dry MOF powder mounted on a silicon sample holder was used for analysis by PXRD. PXRD data was collected at ambient temperature on a Bruker D8 Advance diffractometer at 40 kV, 40 mA for Cu *K*a (l = 1.5418 Å), with a scan speed of 2 sec/step, a step size of 0.05° in 2θ, and a 2θ range of 2-50°. Monolayer sections (~0.5 cm^2)

were removed from the water surface using a glass coverslip and characterized directly on the glass surface using the same conditions.

BET Surface Area Analysis. Samples for analysis were evacuated on a vacuum line overnight at room temperature prior to analysis. ~50 mg samples were then transferred to pre-weighed sample tubes and degassed at 105 °C on a Micromeritics ASAP 2020 Adsorption Analyzer for a minimum of 12 h or until the outgas rate was <5 mmHg. After degassing, the sample tubes were re-weighed to obtain a consistent mass for the samples. BET surface area (m^2/g) measurements were collected at 77 K with N_2 on a Micromeritics ASAP 2020 Adsorption Analyzer using volumetric techniques.

Thermogravimetric Analysis (TGA). 1-5 mg of sample were placed in a 100 μL aluminum crucible. Samples were analyzed on a Mettler Toledo Star TGA/DSC using a temperature range of 30-600 °C scanning at 20 °C/min under an air atmosphere (75 cm^3/min flow rate) for sample degradation.

Scanning Electron Microscopy (SEM). MOF particles or monolayer films were transferred to silicon wafers on a sample holder disk and coated using an Ir-sputter coating for 12 seconds. A FEI Apreo SEM instrument was used for acquiring images using a 5 kV energy source under vacuum at a working distance at 10 mm.

Dynamic Light Scattering (DLS). A dilution of polymer-grafted MOFs (~ 0.1 mg/mL) dispersed in 2 mL of toluene in a glass cuvette was analyzed at 23 °C with a Malvern Instruments Zetasizer Nano ZS90.

Experimental.

Synthesis of cat-CDSPA

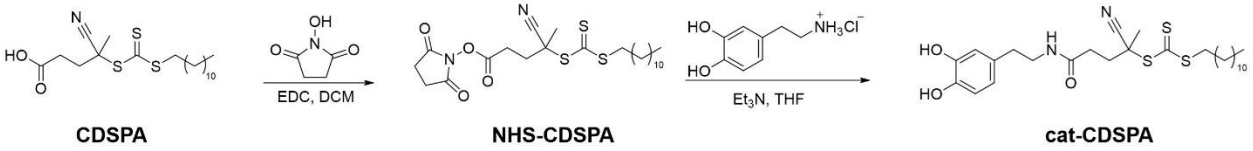

Scheme 3S.1. Synthesis of catechol-ligated 4-cyano-4-[(dodecylsulfanylthiocarbonyl)sulfanyl]pentanoic acid (cat-CDSPA).

2,5-Dioxopyrrolidin-1-yl 4-cyano-4-(((dodecylthio)carbonothioyl)thio)pentanoate (NHS-CDSPA). A 100 mL round bottom flask was charged with 4-cyano-4-[(dodecylsulfanylthiocarbonyl)sulfanyl]pentanoic acid (CDSPA, Sigma-Aldrich), (1.00 g, 2.5 mmol, 1 eq.), *N*-hydroxysuccinimide (428 mg, 3.6 mmol, 1.5 eq.), and 40 mL of dry CH_2Cl_2 (Scheme 3S.1). The flask was degassed with Ar for 5 min and cooled to 0 °C, after which 1-ethyl-3-(3-dimethylaminopropyl)carbodiimide (EDC) (760 mg, 4.0 mmol, 1.6 eq.) was added and the reaction was stirred at room temperature under an Ar atmosphere overnight. After stirring overnight, the organic layer was washed with 1 M HCl (1 × 100 mL), saturated $NaHCO_3$ (1 × 100 mL), brine, and dried with Na_2SO_4. The crude product was purified using column chromatography (EtOAc/hexane, 0-50%, elutes at 35%) to give a yellow solid. Yield: 1.01 g, 81%. ^{1}H NMR (300 MHz, $CDCl_3$): δ 3.38 – 3.27 (m, 2H), 2.93 (t, J = 8.4 Hz, 2H), 2.85 (s, 4H), 2.72 – 2.59 (m, 1H), 2.52 (ddd, J = 14.4, 9.3, 7.1 Hz, 1H), 1.88 (s, 3H), 1.76 – 1.63 (m, 2H), 1.58 (s, 1H), 1.42 (s, 1H), 1.26 (s, 18H), 0.88 (t, J = 6.7 Hz, 3H). ESI-MS(+) Experimental: *m/z* 523.13 $[M+Na]^+$, Calculated for $[C_{23}H_{36}N_2O_4S_3]$: 500.14.

2-Cyano-5-((3,4-dihydroxyphenethyl)amino)-5-oxopentan-2-yl dodecyl carbonotrithioate (cat-CDSPA). A 100 mL round bottom flask was charged with NHS-CDSPA (1 g, 2.0 mmol, 1 eq.), dopamine hydrochloride (417 mg, 2.2 mmol, 1.1 eq.), and 50 mL of dry THF. The flask was

degassed with Ar for 5 min and cooled to 0 °C, after which triethylamine (306 µl, 2.2 mmol, 1.1 eq.) was added dropwise and the reaction was left under an Ar atmosphere in an ice bath and allowed to warm to room temperature overnight. After 24 h, the reaction was diluted with 100 mL of 1M HCl and extracted with $CHCl_3$ (3 × 50 mL). The combined organic layers were washed with brine and dried with Na_2SO_4. The crude product was purified by column chromatography (EtOAc/hexane, 0-70%, elutes at 50%) and dried overnight in a vacuum oven to give an amber resin. Yield: 880 mg, 82%. ^{1}H NMR (500 MHz, $CDCl_3$): δ 6.81 (d, J = 8.0 Hz, 1H), 6.70 (d, J = 1.8 Hz, 1H), 6.59 (d, J = 8.0 Hz, 1H), 3.47 (dd, J = 5.9, 4.5 Hz, 2H), 3.32 (t, J = 7.5 Hz, 2H), 2.70 (t, J = 6.8 Hz, 2H), 2.54 – 2.45 (m, 1H), 2.45 – 2.38 (m, 2H), 2.37 – 2.28 (m, 1H), 1.86 (s, 3H), 1.75 – 1.60 (m, 3H), 1.43 – 1.33 (m, 2H), 1.25 (s, 18H), 0.88 (t, J = 6.9 Hz, 3H). ESI-MS(+) Experimental: *m/z* 539.21 $[M+H]^+$, Calculated for $[C_{27}H_{42}N_2O_3S_3]$: 538.24.

Synthesis of cat-DDMAT

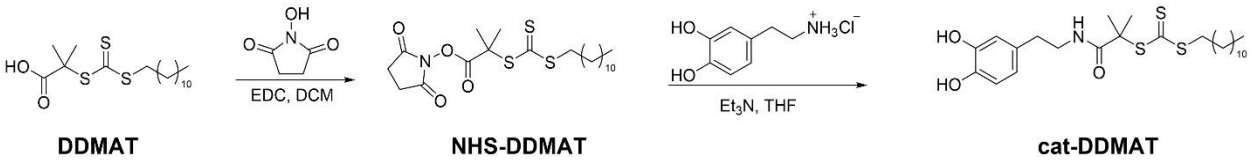

DDMAT **NHS-DDMAT** **cat-DDMAT**

Scheme 3S.2. Synthesis of catechol-ligated 1-((3,4-dihydroxyphenethyl)amino)-2-methyl-1-oxopropan-2-yl dodecyl carbonotrithioate (cat-DDMAT).

2,5-Dioxopyrrolidin-1-yl 2-methyl-2-(((dodecylthio)carbonothioyl)thio)propanoate (NHS-DDMAT). A 100 mL round bottom flask was charged with 2-(((dodecylthio)carbonothioyl)thio)-2-methylpropanoic acid (DDMAT, Sigma-Aldrich) (1.00 g, 2.74 mmol, 1 eq.), *N*-hydroxysuccinimide (473 mg, 4.11 mmol, 1.5 eq.), and 40 mL of dry CH_2Cl_2 (Scheme 3S.2). The flask was degassed with Ar for 5 min and cooled to 0 °C, after which 1-ethyl-3-(3-dimethylaminopropyl)carbodiimide (EDC) (841 mg, 4.39 mmol, 1.6 eq.) was added and the

reaction was stirred at room temperature under an Ar atmosphere overnight. After stirring overnight, the organic layer was washed with 1 M HCl (1 × 100 mL), saturated $NaHCO_3$ (1 × 100 mL), brine, and dried with Na_2SO_4. The crude product was purified using column chromatography (EtOAc/hexane, 0-30%, elutes at 15%) to give yellow crystals. Yield: 1.1 g, 85%. ^{1}H NMR (500 MHz, $CDCl_3$): δ 3.33 (t, 2H), 2.85 (s, 4H), 1.88 (s, 6H) 1.77 – 1.62 (m, 2H), 1.42-1.20 (m, 18H), 0.88 (t, 3H). ESI-MS(+) Experimental: *m/z* 484.09 $[M+Na]^+$, Calculated for $[C_{25}H_{41}NO_3S_3]$: 461.17.

1-((3,4-Dihydroxyphenethyl)amino)-2-methyl-1-oxopropan-2-yl dodecyl carbonotrithioate (cat-DDMAT). A 100 mL round bottom flask was charged with NHS-DDMAT (1.00 g, 2.38 mmol, 1 eq.), dopamine hydrochloride (452 mg, 2.38 mmol, 1.1 eq.), and 50 mL of dry THF. The flask was degassed with Ar for 5 min and cooled to 0 °C, after which triethylamine (330 µl, 2.38 mmol, 1.1 eq.) was added dropwise and the reaction was left under an Ar atmosphere in an ice bath and allowed to warm to room temperature overnight. After 24 h, the reaction was diluted with 100 mL of 1M HCl and extracted with $CHCl_3$ (3 × 50 mL). The combined organic layers were washed with brine and dried with Na_2SO_4. The crude product was purified by column chromatography (EtOAc/hexane, 0-70%, elutes at 35%) and dried overnight in a vacuum oven to give an amber resin. Yield: 785 mg, 72%. ^{1}H NMR (500 MHz, $CDCl_3$): δ 6.81 (d, J = 8.0 Hz, 1H), 6.70 (s, 1H), 6.59 (d, J = 10.2 Hz, 1H), 3.53 – 3.42 (m, 2H), 3.32 (t, J = 7.4 Hz, 2H), 2.70 (t, J = 6.9 Hz, 2H), 1.86 (s, 6H), 1.68 (p, J = 7.4 Hz, 2H), 1.46-1.19 (m, 18H), 0.88 (t, J = 6.9 Hz, 3H). ESI-MS(+) Experimental: *m/z* 523.13 $[M+Na]^+$, Calculated for $[C_{25}H_{41}NO_3S_3]$: 499.22.

MOF Synthesis

UiO-66$_x$. UiO-66 was prepared using a continuous addition method as previously reported (*Angew. Chem. Int. Ed.* **2018**, 57, 7836-7840). The synthesis of UiO-66$_x$ (x = the particle edge length in nm measured by scanning electron microscopy, SEM) at 5 L scale was carried out at 120 °C under atmospheric pressure in DMF using formic acid as a modulator. Two separate 30 mM stock solutions were prepared in 5L jars. The terephthalic acid (H_2bdc) solution was prepared with 22.5 g of H_2bdc, 4.05 L of DMF, and 450 mL of formic acid, while the $ZrOCl_2 \cdot 8H_2O$ was prepared with 45 g of $ZrOCl_2 \cdot 8H_2O$ in 4.5 L of DMF. The reaction procedure is as follows. An initial 100 mL of the $ZrOCl_2 \cdot 8H_2O$ solution was added to a 5 L round bottom flask at 120 °C, then both the $ZrOCl_2 \cdot 8H_2O$ and H_2bdc stock solution were separately delivered by peristaltic pump with a feed rate of 12 mL/min for 5 min. The feed rate was accelerated to 32 mL/min for 55 minutes. After this first addition, 2.5 L of the reaction solution was removed from the reactor to obtain the first product, UiO-66$_{80}$, and then 1.5 L of metal stock solution and 1.5 L of ligand stock solution were further added into the remaining reaction solution at 30 mL/min for 50 min. Then 3 L of reaction solution was collected from the reactor to obtain the second product, UiO-66$_{120}$. Finally, 1.55 L of metal stock solution and 1.55 L of ligand stock solution were added into the reactor within 1 h at 25.8 mL/min, and the remaining reaction solution (3.7 L) was collected as the third product UiO-66$_{250}$. All products were first centrifuged (8000 rpm, 30-60 min) and washed with 40 mL DMF twice, and then solvent exchange was performed with by washing 3 times in 40 mL of methanol. The MOFs were left suspended in methanol at ~20 mg/mL until further use. Before any experiment, a fraction of the sample was removed and dried to determine the exact weight percent of the suspended particles. For PXRD and N_2 sorption experiments the samples were dried in vacuum at 120 °C for 24 h.

Surface Functionalization of UiO-66 with cat-CDSPA

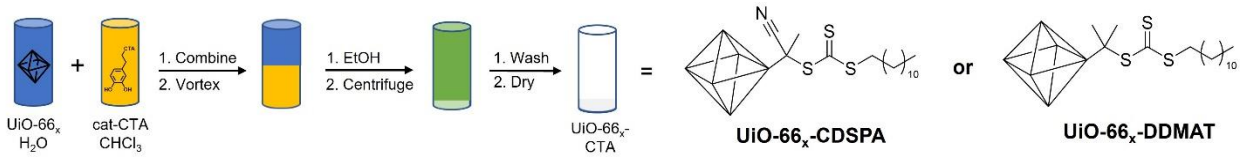

Scheme 3S.3. Surface functionalization procedure of UiO-66$_x$ with either cat-CDSPA or cat-DDMAT. UiO-66$_x$ is depicted by octahedron with aqueous and $CHCl_3$ layers represented by blue and orange colors, respectively. Mixed layers after ethanol addition is represented in green.

A 50 mL centrifuge tube was prepared with 200 mg of UiO-66$_x$ in MeOH, centrifuged (8000 rpm, 15 min) to collect particles and redispersed in 10 mL of water. A separate vial was prepared with 10 mg of either cat-CDSPA or cat-DDMAT dissolved in 5 mL of $CHCl_3$ and added to the aqueous MOF suspension. The biphasic mixture was vortexed for 5 min, and then 20 mL of EtOH was added to form a homogeneous suspension. The particles were collected by centrifugation (8000 rpm, 15 min), washed via repeated dispersion/centrifugation cycles with EtOH (2 × 25 mL, 30 min immersion each), followed by DMSO (3 × 20 mL, 30 min immersion each), and finally suspended in DMSO at a concentration of 80 mg/mL.

SI-PET-RAFT from UiO-66-CTA

General Polymerization Notes

All polymerizations were conducted using 40 mg of UiO-66$_x$-CTA regardless of particle size. The MOFs were stored as an 80 mg/mL suspension in DMSO; dried particles required extensive sonication to achieve adequate dispersion prior to polymerization. To ensure a controlled polymerization, it was necessary to add unbound CTA to the solution in excess to the surface (MOF) bound CTA. For each polymerization, the volume of monomer and solvent was held

constant, and the targeted number of repeat units (degree of polymerization, DP) was adjusted by increasing or decreasing the amount of CTA relative to monomer while assuming 75% conversion. For example, if targeting a surface DP of 1500 for UiO-66$_x$-MA$_{1500}$, 1.68 mL (18.5 mmol) of methyl acrylate and 3.38 mg (9.3 µmol) of DDMAT are added, giving a molar ratio of MA:DDMAT 2000:1. For UiO-66$_x$-MA$_{2400}$, 1.68 mL (18.5 mmol) of methyl acrylate and 2.11 mg (5.80 µmol) of DDMAT are used giving a molar ratio of MA:DDMAT 3200:1. The amount of Ir(ppy)$_3$ was always set to 1x10^{-6} molar ratio relative to monomer. It is important to add the monomer to the reaction dropwise under rapid stirring, as it was observed that rapid addition of the monomer caused the MOF particles to irreversibly aggregate and settle out of the solution.

Polymerization of Methyl Acrylate from UiO-66-DDMAT

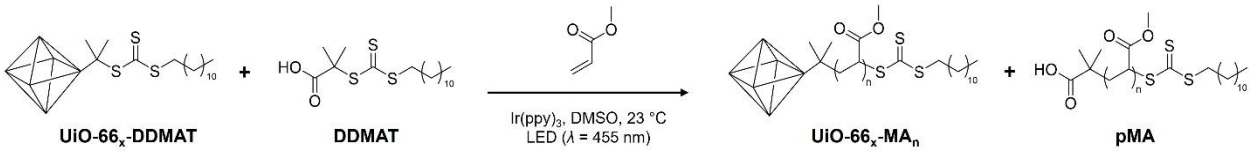

Scheme 3S.4. Surface-initiated polymerization of methyl acrylate from UiO-66$_x$-DDMAT and the additional unbound DDMAT in solution.

UiO-66$_x$-MA$_{1500}$. A 10 mL round bottom flask was charged with a magnetic stir bar, 2.5 mL DMSO, and 500 µL of an 80 mg/mL stock solution of UiO-66$_x$-DDMAT suspended in DMSO. The solution was constantly stirred while DDMAT (3.38 mg, 9.3 µmol, 1 eq.) and Ir(ppy)$_3$ (12.1 µg, 0.018 µmol, .002 eq.) were added (from 10 mg/mL and 1 mg/mL DMF stock solutions, respectively). Methyl acrylate (1.68 mL, 18.5 mmol, 2000 eq.) was then added dropwise after which the suspension was left without stirring for 5 min to ensure that the MOF particles had not aggregated and settled. The reaction was then sealed tight with a rubber septum secured with a

copper wire and degassed with Ar for 30 min. The reaction mixture was transferred to a homemade blue light photoreactor and irradiated until mixture could no longer stir.

Polymerization of Methyl Methacrylate from UiO-66-CDSPA

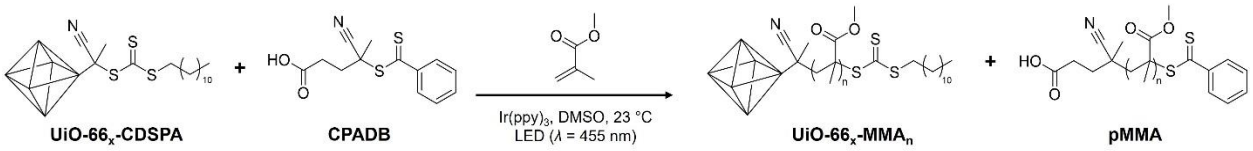

Scheme 3S.5. Surface-initiated polymerization of methyl methacrylate from UiO-66$_x$-CDSPA and the additional unbound CPADB in solution.

UiO-66$_x$-MMA$_{1500}$. A 10 mL round bottom flask was charged with a magnetic stir bar, 2.0 mL DMSO, and 500 µL of an 80 mg/mL stock solution of UiO-66$_x$-CDSPA suspended in DMSO. The solution was constantly stirred while CPADB (2.60 mg, 9.3 µmol, 1 eq.) and Ir(ppy)$_3$ (12.1 µg, 0.018 µmol, .002 eq.) were added (from 10 mg/mL and 1 mg/mL DMF stock solutions, respectively). Methyl methacrylate (1.98 mL, 18.5 mmol, 2000 eq.) was then added dropwise after which the suspension was left without stirring for 5 min to ensure that the MOF particles had not aggregated and settled. The reaction was then sealed tight with a rubber septum secured with a copper wire and degassed with Ar for 30 min. The reaction mixture was transferred to a homemade blue light photoreactor and irradiated until mixture could no longer stir.

Polymerization of Benzyl Methacrylate from UiO-66-CDSPA

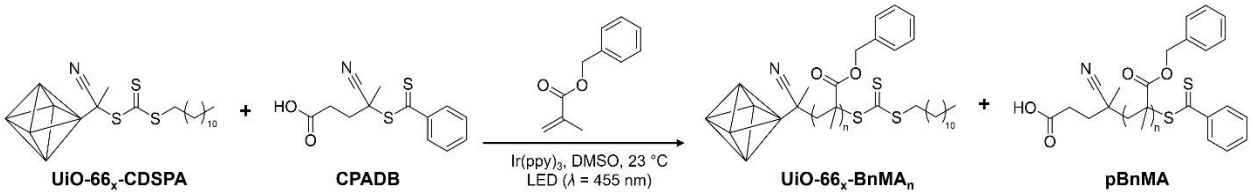

Scheme 3S.6. Surface-initiated polymerization of benzyl methacrylate from UiO-66$_x$-CDSPA and the additional unbound CPADB in solution.

UiO-66$_x$-BnMA$_{1500}$. A 10 mL round bottom flask was charged with a magnetic stir bar, 1.5 mL DMSO, and 500 µL of an 80 mg/mL stock solution of UiO-66$_x$-CDSPA suspended in DMSO. The solution was constantly stirred while CPADB (1.63 mg, 5.84 µmol, 1 eq.) and Ir(ppy)$_3$ (7.65 µg, 0.012 µmol, .002 eq.) were added (from 10 mg/mL and 1 mg/mL DMF stock solutions, respectively). Benzyl methacrylate (1.98 mL, 11.7 mmol, 2000 eq.) was then added dropwise after which the suspension was left without stirring for 5 min to ensure that the MOF particles had not aggregated and settled. The reaction was then sealed tight with a rubber septum secured with a copper wire and degassed with Ar for 30 min. The reaction mixture was transferred to a homemade blue light photoreactor and irradiated until mixture could no longer stir.

General Workup. The rubber septa was removed, and a small sample of the reaction was collected and diluted in 700 µL $CDCl_3$ for ^{1}H NMR analysis to determine conversion. The primary reaction mixture was diluted with 40 mL THF, transferred to a 50 mL centrifuge tube, and the particles were collected by centrifugation until the supernatant was no longer cloudy (UiO-66$_{250}$: 8000 rpm, 20 min; UiO-66$_{120}$: 8000 rpm, 30 min; UiO-66$_{80}$: 10000 rpm, 30 min). The MOF particles were then washed by redispersing in 5 × 40 mL of THF (20 min immersion after redispersing per wash cycle, followed by centrifugation under conditions specified above) to

ensure complete removal of any unbound, free polymer. Gel permeation chromatography (GPC) of the supernatant after last wash was used to confirm removal of all free polymer. The washed MOF particles were resuspended in 10 mL of THF and transferred to a 15 mL centrifuge tube before dividing into samples for further analysis and self-assembly experiments. For all materials, several samples were prepared for analysis and experiments (Scheme 3.1, main text). From the THF dispersion, 2 mL of solution were transferred to a 15 mL centrifuge tube and exchanged with 3 × 10 mL CH_2Cl_2 (8000 rpm, 20 min) for thermogravimetric analysis (TGA). The remaining 8 mL of the THF dispersion were then exchanged with 3 × 10 mL of toluene (8000 rpm, 10 min) and 1 mL was removed for GPC digestion analysis and another 1 mL removed for dynamic light scattering (DLS) analysis. The remaining ~6 mL of particle solution was used for self-assembly at an air-water interface.

Removal of Free-Standing Area of SAMM on Wire Loop

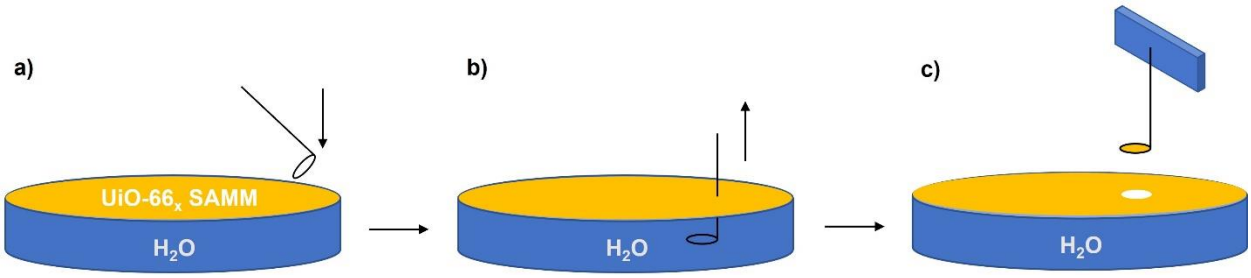

Scheme 3S.7. A segment of the monolayer is removed using a copper wire loop by a) inserting the wire loop under the surface of the film, b) gently lifting the loop from underneath the film parallel to the water surface, and c) carefully hanging the suspended film to let the water dry. A successful free-standing monolayer was identified by a dried film that remained suspended across the wire loop.

Coarse-Grained (CG) Model of MOF-Interface System. A CG model previously used for studying polymer-grafted nanoparticles at polymer interfaces was adapted for treating polymer-grafted MOFs at an air-water interface.[12-13] Briefly, the MOFs were modeled as rigid octahedra

constructed out of a lattice of CG beads of size σ_{CG}. Octahedra of edge lengths $9\sigma_{CG}$, $13\sigma_{CG}$, $28\sigma_{CG}$ were explored, corresponding to experimental MOFs of edge lengths 80, 120, 250 nm. The polymer grafts were modeled as chains of CG beads (also of size σ_{CG}) representing short segments of the polymer chain.[14] Adjacent beads in the chain were connected via finitely extensible nonlinear elastic (FENE) springs and interact with each other via a short-ranged repulsive Weeks-Chandler-Anderson (WCA) excluded-volume potential.[15] The grafts were attached uniformly to all facets of the MOF particles at a grafting density of 0.3 chains/$\sigma_{CG}{}^2$. To study the effects of degree of polymerization of the grafts examined experimentally, chain lengths of 1, 2, 4, and 6 beads were investigated. The water and air phases were also treated using CG beads, which interact with each other *within* the same phase via an attractive Lennard-Jones (LJ) potential of size σ_{CG} and energy ε and *across* the phase with a repulsive WCA potential. The two fluids were maintained at densities of 0.4 and 0.02 beads/$\sigma_{CG}{}^3$, which led to stable gas- and liquid-like phases and a sufficiently large surface tension between them at the simulated temperature. The remaining interactions between beads comprising the solvent, MOF particles, and polymer grafts were also treated using a combination of LJ and WCA potentials, depending on their mutual miscibility. For convenience, we considered the same size and energy parameters σ_{CG} and ε for these potentials, except for those describing the interactions between polymer graft beads in the water phase. These interactions were treated using an LJ potential with an adjustable energy parameter $\lambda\varepsilon$, where λ was varied between a value of 0 signifying strongly hydrophobic chains to a value of 1 signifying hydrophilic chains.

Molecular Dynamics (MD) Simulations. The LAMMPS program was used for carrying out MD simulations of polymer-grafted MOFs at the air-water interface.[16] All simulations were carried out in the canonical (NVT) ensemble at a temperature of $0.7\varepsilon/k_B$, where k_B is the Boltzmann

constant. A velocity-Verlet algorithm with a time step of 0.002 $(m\sigma_{CG}{}^2/\varepsilon)^{1/2}$ (m = mass of each CG bead) and a Nosé-Hoover thermostat with a time constant of $1.0(m\sigma_{CG}{}^2/\varepsilon)^{1/2}$ were used for integrating the equations of motion and controlling temperature. Two impermeable LJ walls were used to confine the air and water particles in the z-direction normal to the interface, while periodic boundary conditions were applied in the x and y directions parallel to the interface. To minimize the effect of the walls on the interface, the air and water layers were chosen to be sufficiently thick (~$30\sigma_{CG}$). A slow compression protocol was used for generating an equilibrated system of well-dispersed *stationary* MOF particles trapped at the air-water interface.[13] Subsequently, equilibrium simulations of *freely mobile* MOFs were performed for ~12 million timesteps for exploring their orientational and self-assembly behavior. The final orientation, z-position, and assembly morphology that the MOFs adopted were found to be insensitive to their initial orientation and position.

Classification of Particle Orientations in Simulations. A method based on the interface-projected areas of MOF facets was used for classifying the MOFs into the three main orientational states: vertex-up, edge-up, and face-up (Figure 3S.10).[13] This involves determining the normal vector of each facet and using this vector to calculate the interface-projected areas of those facets pointing upwards towards the air phase. From the total projected area, the % area contributed by the two most dominant faces, denoted S_1 and S_2, is obtained. If $S_1 < 37.5\%$, then the orientation is classified as 'vertex-up'; otherwise, S_2 is required to distinguish between the other two orientations. If $S_1 \geq 0.375\%$ and $S_2 \geq 0.333\%$, the particle exhibits 'face-up' orientation. If $S_1 \geq 0.375\%$ and $S_2 \leq 0.333\%$, the particle exhibits 'edge-up' orientation.

Supporting Figures and Tables

Table 3S.1. Synthesis conditions and characteristics of polymer grafted MOF nanoparticles prepared in this study ($Đ = M_w/M_n$), N = degree of polymerization, h = calculated brush height (nm), σ = grafting density (chains/nm^2).

Sample	Monomer Eq.	$Ir(ppy)_3$ Eq.	Mn (kDa)	Mw (kDa)	$Đ$	N	Size DLS (nm)	h	Polymer wt.%	σ
UiO-66$_{80}$-MMA$_{520}$	1200	0.001	52.0	69.2	1.33	520	124	17	26	0.26
UiO-66$_{80}$-MMA$_{1186}$	1500	0.0015	118.6	140.8	1.19	1186	175.9	43	23	0.10
UiO-66$_{80}$-MMA$_{1453}$	2000	0.002	145.3	182.1	1.25	1453	168	39	31	0.12
UiO-66$_{80}$-MMA$_{3195}$	4000	0.004	319.5	463	1.45	3195	347.6	129	46	0.10
UiO-66$_{80}$-MA$_{1574}$	2000	0.002	135.4	145.7	1.08	1574	245.9	78	78	1.02
UiO-66$_{80}$-MA$_{2279}$	2500	0.0025	196.0	218.4	1.12	2279	314.9	113	67	0.40
UiO-66$_{80}$-MA$_{2747}$	3500	0.0035	236.2	291.4	1.23	2747	257	84	23	0.05
UiO-66$_{80}$-BnMA$_{715}$	1500	0.0015	125.9	239.2	1.9	715	193.2	52	31	0.13
UiO-66$_{80}$-BnMA$_{1855}$	2500	0.0025	326.4	422.4	1.29	1855	182	46	32	0.06
UiO-66$_{80}$-BnMA$_{2151}$	3000	0.003	378.5	527.5	1.39	2151	187.8	49	32	0.05
UiO-66$_{120}$-MMA$_{452}$	1000	0.001	45.0	63.8	1.41	452	157.2	12	21	0.23
UiO-66$_{120}$-MMA$_{1180}$	1500	0.0015	118.0	145.7	1.22	1180	221.3	44	18	0.07
UiO-66$_{120}$-MMA$_{1952}$	2500	0.0025	195.2	249.6	1.28	1952	297.6	82	31	0.09
UiO-66$_{120}$-MMA$_{2539}$	3000	0.003	253.9	331.5	1.31	2539	357.9	112	33	0.08
UiO-66$_{120}$-MMA$_{4071}$	4500	0.0045	407.1	657.3	1.62	4071	478	172	41	0.07
UiO-66$_{120}$-MA$_{452}$	1500	0.001	38.9	40.2	1.03	452	198.1	32	19	0.23
UiO-66$_{120}$-MA$_{1294}$	1500	0.0015	111.3	122.6	1.1	1294	244	55	41	0.24
UiO-66$_{120}$-MA$_{2056}$	2500	0.0025	176.8	190.7	1.08	2056	273	70	43	0.17
UiO-66$_{120}$-MA$_{2370}$	3500	0.0035	203.8	219	1.08	2370	293	80	68	0.40

Table 3S.1. Synthesis conditions and characteristics of polymer grafted MOF nanoparticles prepared in this study ($Đ = M_w/M_n$), N = degree of polymerization, h = calculated brush height (nm), σ = grafting density (chains/nm^2).

Sample	Monomer Eq.	$Ir(ppy)_3$ Eq.	Mn (kDa)	Mw (kDa)	*Đ*	*N*	Size DLS (nm)	*h*	Polymer wt.%	*σ*
UiO-66$_{120}$-BnMA$_{1054}$	1500	0.0015	185.5	3157	1.7	1054	242.5	54	25	0.07
UiO-66$_{120}$-BnMA$_{2878}$	3000	0.003	506.6	537.3	1.06	2878	250.5	58	23	0.02
UiO-66$_{250}$-MMA$_{690}$	1500	0.0015	69.0	77.5	1.12	690	313.9	18	18	0.12
UiO-66$_{250}$-MMA$_{1460}$	2000	0.002	146.0	187.2	1.28	1460	318	20	17	0.05
UiO-66$_{250}$-MMA$_{2566}$	3000	0.003	256.6	318.4	1.24	2566	350.7	36	19	0.03
UiO-66$_{250}$-MMA$_{4552}$	5000	0.005	455.2	597.2	1.31	4552	374.3	48	23	0.02
UiO-66$_{250}$-MA$_{750}$	1500	0.0015	64.5	66.4	1.03	750	332	27	12	0.08
UiO-66$_{250}$-MA$_{994}$	2000	0.002	85.5	90.7	1.06	994	329.9	26	14	0.07
UiO-66$_{250}$-MA$_{2429}$	3000	0.003	208.9	222.3	1.06	2429	397.9	60	28	0.07
UiO-66$_{250}$-MA$_{2588}$	3000	0.003	222.6	237.5	1.07	2588	410.6	66	27	0.07
UiO-66$_{250}$-BnMA$_{1309}$	1500	0.0015	230.4	271	1.43	1309	335.9	29	19	0.04
UiO-66$_{250}$-BnMA$_{2920}$	3500	0.0035	513.9	542	1.06	2920	326.5	24	17	0.02

Table 3S.2. Molecular weights of free polymer with no MOF present, with unfunctionalized UiO-66$_{120}$, and UiO-66$_{120}$-DMeCTA.

Sample	Monomer eq.	$Ir(ppy)_3$	% Conversion	M_n (g/mol)	M_w (g/mol)	Đ
No MOF	1500	.0015	89	117,000	128,000	1.09
UiO-66$_{120}$	1500	.0015	84	95,100	119,400	1.255
UiO-66$_{120}$-cat-DDMAT	1500	.0015	81	90,400	110,200	1.220

Figure 3S.1. Experimental setup for the large- scale synthesis of UiO-66$_x$. 4L Flasks (left and right sides) contain separate stock solutions of H_2bdc and $ZrOCl_2 \cdot 8H_2O$ in DMF (30 mM). Peristaltic pumps deliver both solutions at prescribed feed rates to the 4L 3-neck round bottom flask set in a heating mantel. The mantel was used to hold the temperature of the reaction solution at 120 °C.

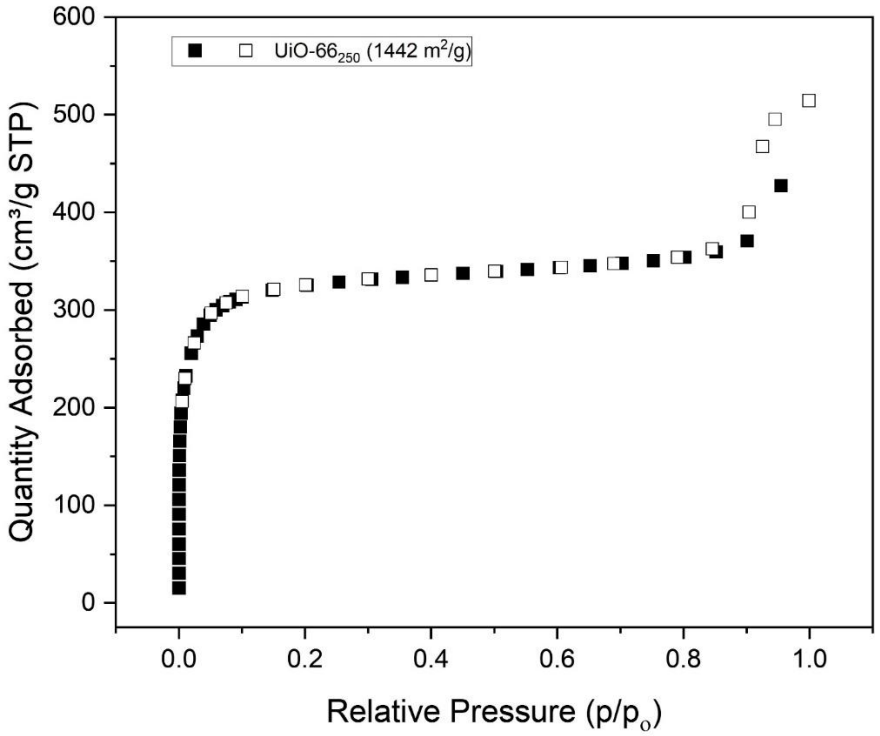

Figure 3S.2. N_2 sorption isotherm for UiO-66$_{250}$ with respective BET surface area.

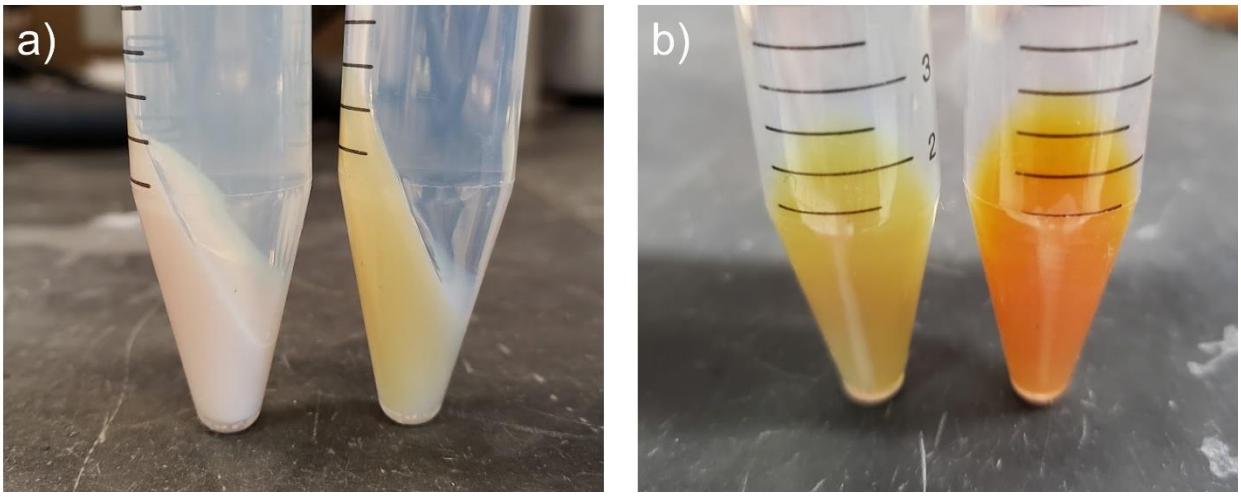

Figure 3S.3. a) UiO-66_{120} before (*left*) and after (*right*) functionalization with cat-CDSPA. b) UiO-66_{80} functionalized with cat-CDSPA (*left*) and cat-DDMAT (*right*).

Figure 3S.4. Home built LED reaction vessel lined with blue led strips.

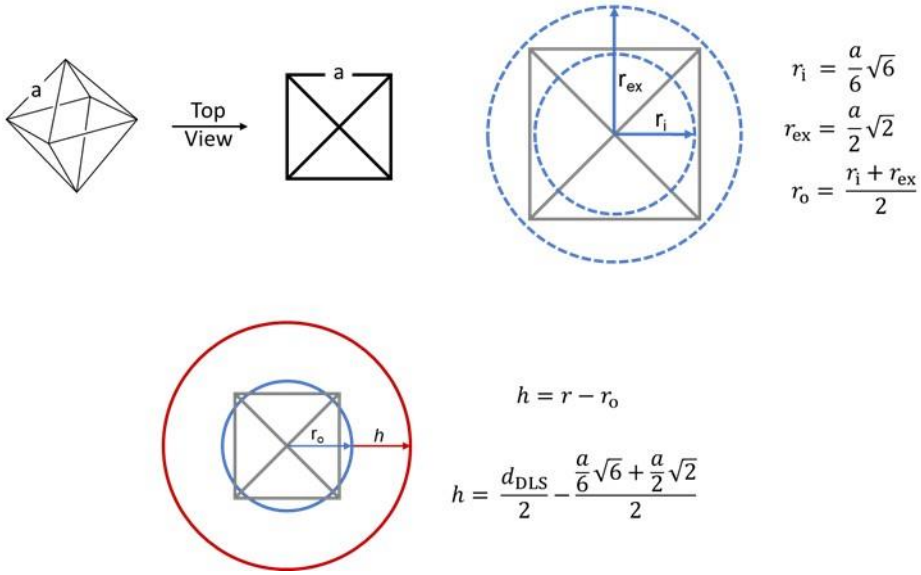

Figure 3S.5. Polymer brush height determination using an intermediate size sphere as an internal radius. DLS of polymer grafted MOF nanoparticles is based on the diameter of a sphere with the same diffusion constant as the particle in solution; therefore, a simplified model of the octahedral MOF was used to determine brush height. A sphere inside the MOF which contacts each face tangentially has a radius $r_i = (a/6)\times 6^{-1}$ and a sphere outside the octahedron in contact with each vertex has a radius $r_{ex} = (a/2)\times 2^{-1}$. The average of these two radii, termed r_o, was used to represent a sphere of average distance from the center of the MOF particle. The brush height was then determined by subtracting r_o from the radius given by DLS.

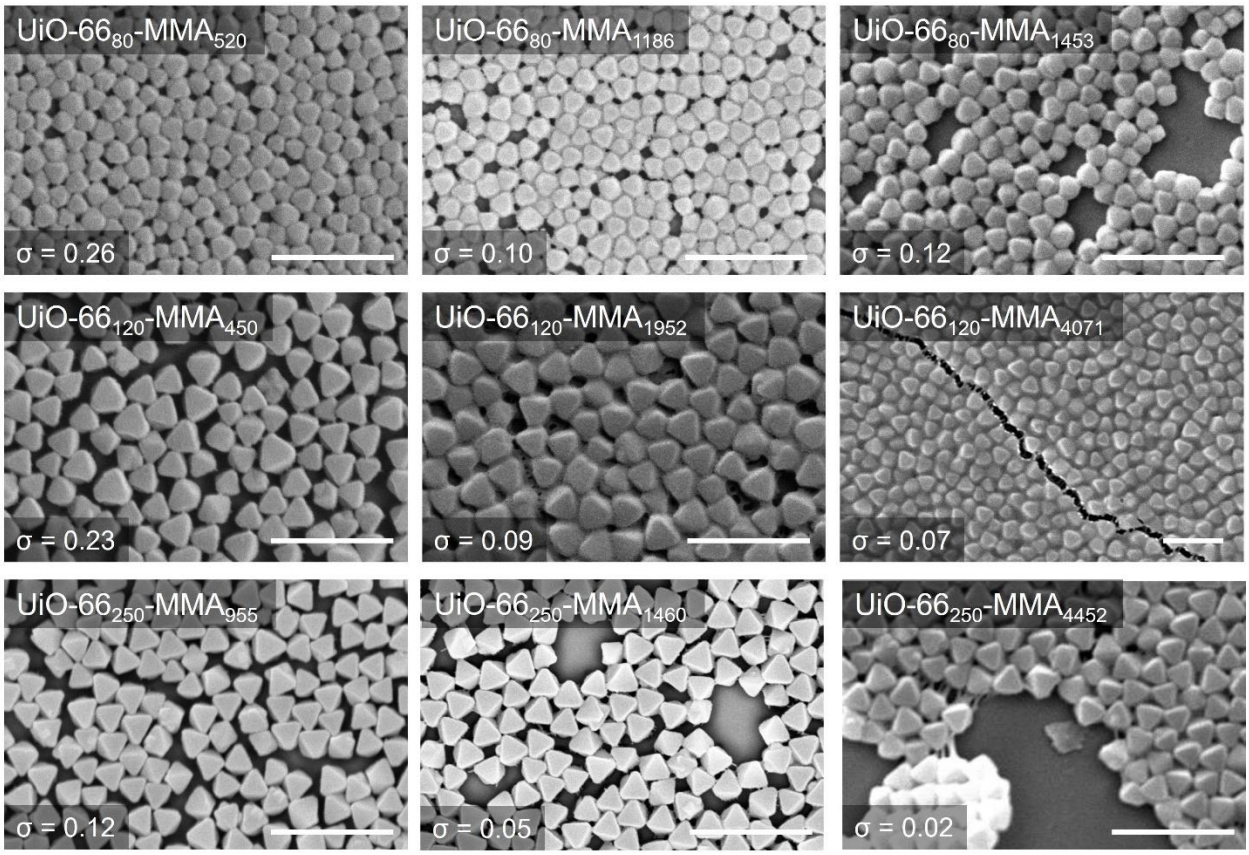

Figure 3S.6. SEM images of self-assembled films of UiO-66$_x$-MMA$_n$. Scale bars are 500 nm for the first two rows and 1 μm for the bottom row.

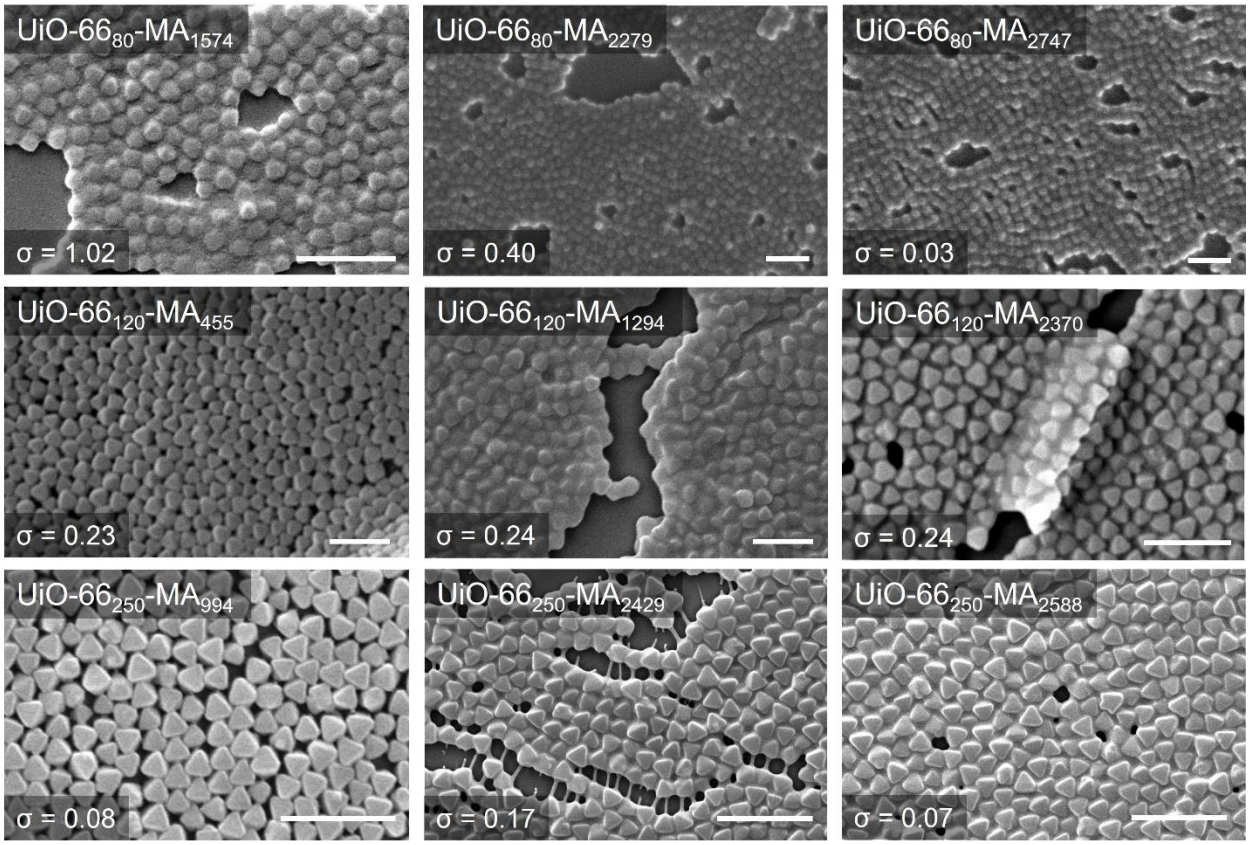

Figure 3S.7. SEM images of self-assembled films of UiO-66$_x$-MA$_n$. Scale bars are 500 nm for the first two rows and 1 μm for the bottom row.

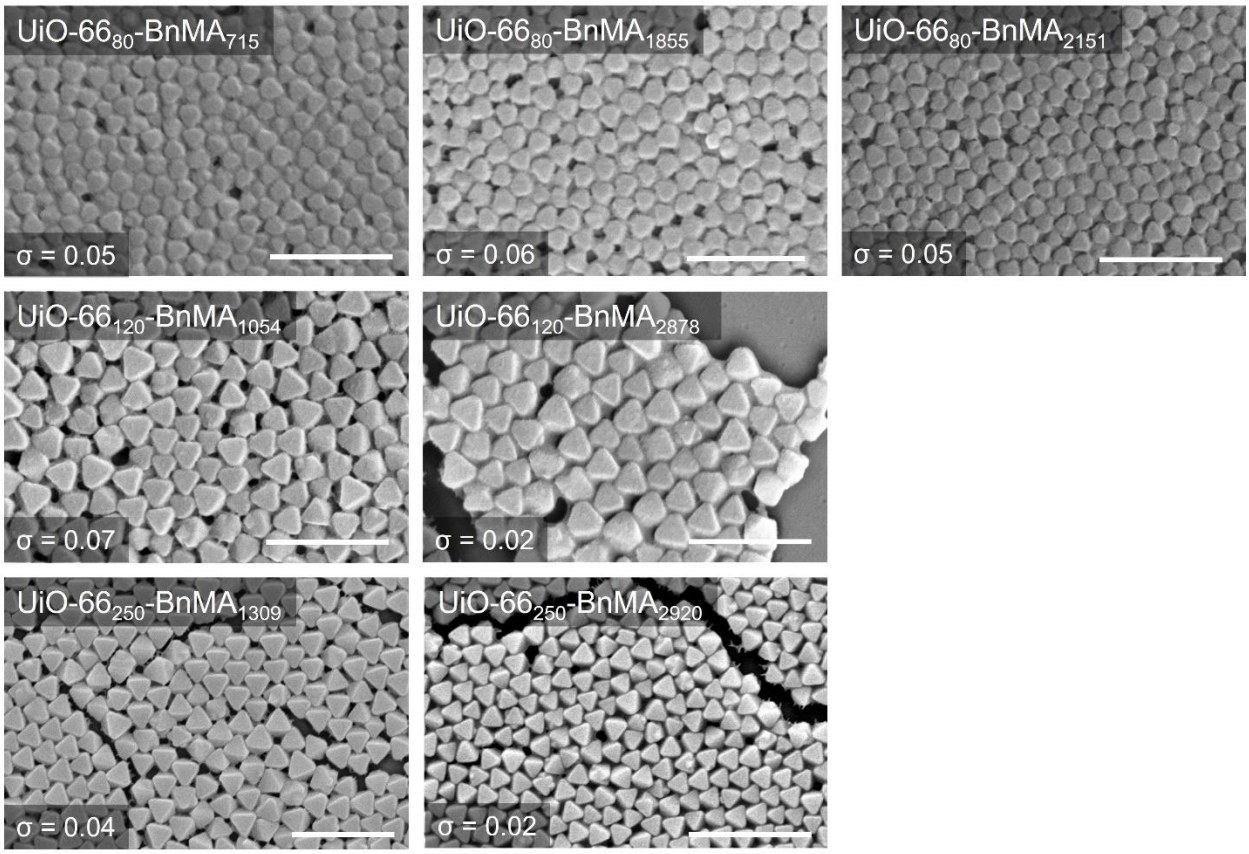

Figure 3S.8. SEM images of self-assembled films of UiO-66$_x$-BnMA$_n$. Scale bars are 500 nm for the first two rows and 1 μm for the bottom row.

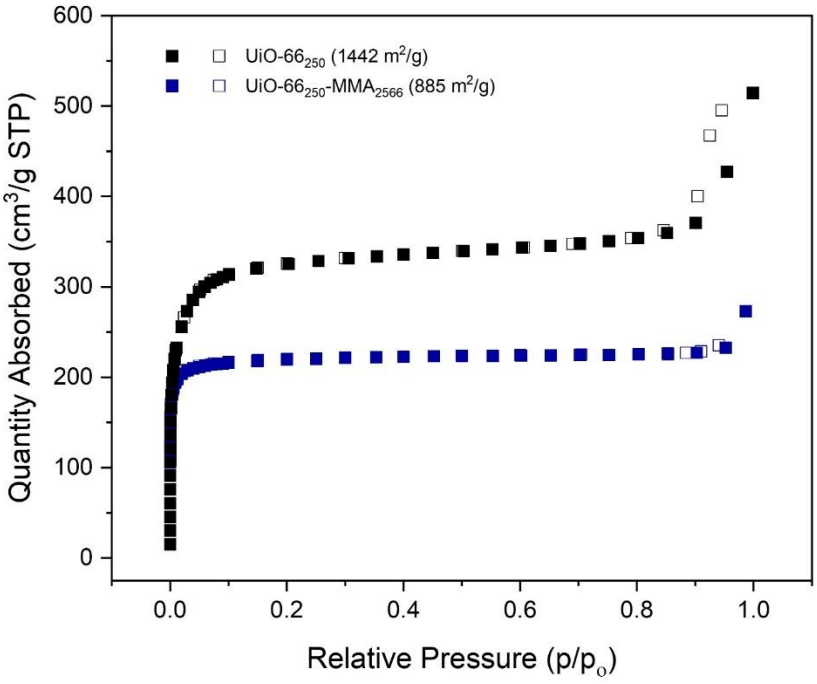

Figure 3S.9. N_2 sorption isotherm for UiO-66_{250} and UiO-66_{250}-MMA_{2566} with respective BET surface area.

Coarse-Grained Model

To investigate the dynamics of polymer-grafted MOFs at an air-water interface, we extended the coarse-grained model we previously developed for studying the assembly of polymer-grafted nanocubes at polymer interfaces. The MOFs were modeled as rigid bodies of regular octahedra geometry constructed out of coarse-grained beads, each of size σ_{CG}, where σ_{CG} corresponds to a length scale of ~10 nm. Three sets of MOFs were constructed with edge lengths of $L_{\mathrm{MOF}} = 9\sigma_{CG}$, $13\sigma_{CG}$, and $28\sigma_{CG}$ corresponding to the experimental MOFs with edge lengths 80, 120, and 250 nm.

Polymer grafts (denoted by "g") were attached to all eight facets of the MOFs at a grafting density of 0.3 chains/${\sigma_{CG}}^2$ to target the low grafting density regimes investigated in experiments. The grafts were treated as Kremer-Grest bead-chains, where short segments of the chain are described by coarse-grained beads of size σ_{CG} and mass m. We explored chain lengths of $L_{\mathrm{g}} = 1, 2, 4,$ and 6 beads to characterize the effect of degree of polymerization studied in the experiments. Adjacent beads in the chains, denoting *bonded segments*, interacted with each other through finitely extensible nonlinear elastic (FENE) spring and Weeks-Chandler-Anderson (WCA) potentials. The FENE spring potential, which ensures that bonded segments do not stretch beyond a cutoff distance, is given by:

$$U_{\mathrm{FENE}}(r; k, R_0) = -\frac{k}{2} R_0^2 \ln\left[1 - \left(\frac{r}{R_0}\right)^2\right] \quad (1)$$

where r is the separation distance between the segments, $k = 30\varepsilon/{\sigma_{CG}}^2$ is the spring constant, ε is the characteristic energy parameter, and $R_0 = 1.5\sigma_{CG}$ is the maximum possible length of the spring. The WCA potential, a short-range purely repulsive potential that models excluded-volume interactions between the bonded segments, can be conveniently presented in the form of a cut-and-shifted Lennard-Jones (LJ) potential:

$$U_{\mathrm{LJ}}(r;\sigma_{CG},\varepsilon,r_{\mathrm{c}})=\begin{cases}4\varepsilon\left[\left(\frac{\sigma_{CG}}{r}\right)^{12}-\left(\frac{\sigma_{CG}}{r}\right)^{6}-\left(\frac{\sigma_{CG}}{r_c}\right)^{12}+\left(\frac{\sigma_{CG}}{r_c}\right)^{6}\right] & r<r_c\\ 0 & r\geq r_c\end{cases} \quad (2)$$

with a cutoff distance of $r_c=2^{1/6}\sigma_{CG}$. The grafts were also attached to the surface beads of the MOFs via the combined FENE-WCA potential.

The water (w) and air (a) phases were also treated using coarse-grained beads. The water beads interact with each other via an attractive Lennard-Jones (LJ) potential $U_{\text{w-w}}=U_{\mathrm{LJ}}(r;\sigma_{CG},\varepsilon,r_{\mathrm{c}}=2.5\sigma_{CG})$, which accounts for both attractive and the excluded-volume interactions due to the larger cutoff of $r_c=2.5\sigma_{CG}$. The air beads interact with each other and with water beads *via* the excluded-volume WCA potential $U_{\text{a-a}}=U_{\text{w-a}}=U_{\mathrm{LJ}}\left(r;\sigma_{CG},\varepsilon,r_{\mathrm{c}}=2^{1/6}\sigma_{CG}\right)$. The two fluids were maintained at number densities of 0.4 and 0.02 beads/$\sigma_{CG}{}^3$, which together with the above interaction potentials led to stable liquid- and gas-like phases and a sufficiently large surface tension between them at the simulated temperature of $0.7\varepsilon/k_B$.

Pairs of *non-bonded* segments within a polymer chain or across chains interacted with each other *via* the LJ potential $U_{\mathrm{g-g}}=U_{\mathrm{LJ}}(r;\sigma_{CG},\varepsilon,r_c=2.5\sigma_{CG})$. The interactions between the grafts and the air phase were also treated by the LJ potential $U_{\mathrm{g-a}}=U_{\mathrm{LJ}}(r;\sigma_{CG},\varepsilon,r_{\mathrm{c}}=2.5\sigma_{CG})$. Depending on the hydrophobicity of the grafts being studied, the grafts were either partially miscible or fully miscible with the water phase: when partially miscible, the segments interacted *via* the LJ potential $U_{\text{g-w}}=U_{\mathrm{LJ}}(r;\sigma_{CG},\lambda\varepsilon,r_{\mathrm{c}}=2.5\sigma_{CG})$ with a reduced attraction strength of $\lambda\varepsilon$, where $0<\lambda<1$; and when fully miscible (strongly hydrophilic), they interacted *via* the original LJ potential $U_{\text{g-w}}=U_{\mathrm{LJ}}(r;\sigma_{CG},\varepsilon,r_{\mathrm{c}}=2.5\sigma_{CG})$. To account for the hydrophilic nature of the studied MOFs, the interactions between the MOFs and water beads were treated by the LJ potential $U_{\text{MOF-w}}=U_{\mathrm{LJ}}(r;\sigma_{CG},\varepsilon,r_{\mathrm{c}}=2.5\sigma_{CG})$. The interactions between the MOFs, the MOFs and air beads, and the

MOFs and polymer grafts were all treated using a excluded-volume WCA potential $U_{\text{MOF-MOF}} = U_{\text{MOF-a}} = U_{\text{MOF-g}} = U_{\text{LJ}}\left(r; \sigma_{CG}, \varepsilon, r_{\text{c}} = 2^{1/6}\sigma_{CG}\right)$.

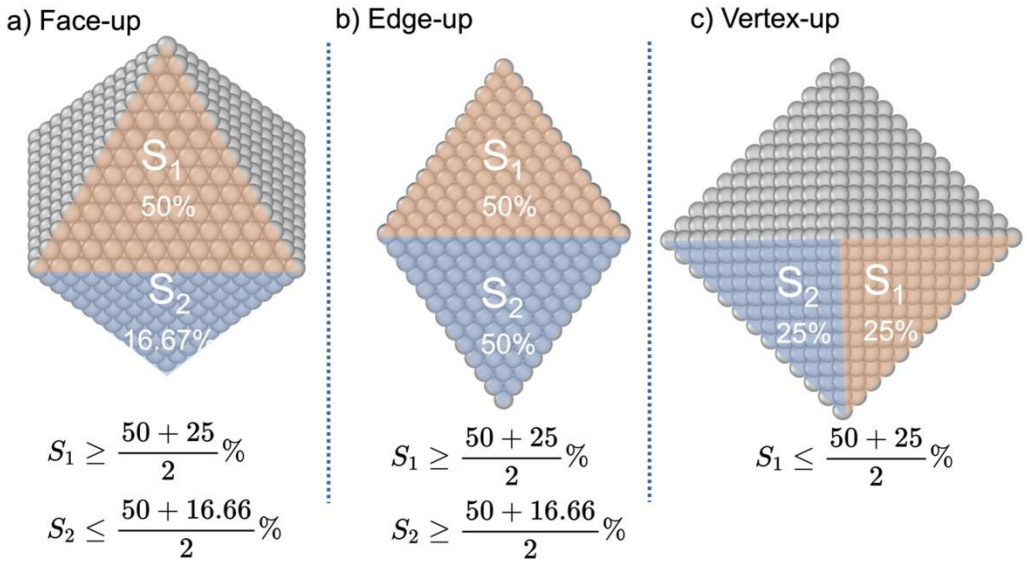

Figure 3S.10. Orientation classification method. S_1 and S_2 represent the % of the total interface-projected area contributed by the first- and second-most dominant facets of the octahedral MOF particle. (a) If $S_1 \geq 0.375\%$ and $S_2 \geq 0.333\%$, the particle exhibits 'face-up' orientation. (b) If $S_1 \geq 0.375\%$ and $S_2 \leq 0.333\%$, the particle exhibits 'edge-up' orientation. (c) If $S_1 \leq 0.375\%$, the particle exhibits 'vertex-up' orientation.

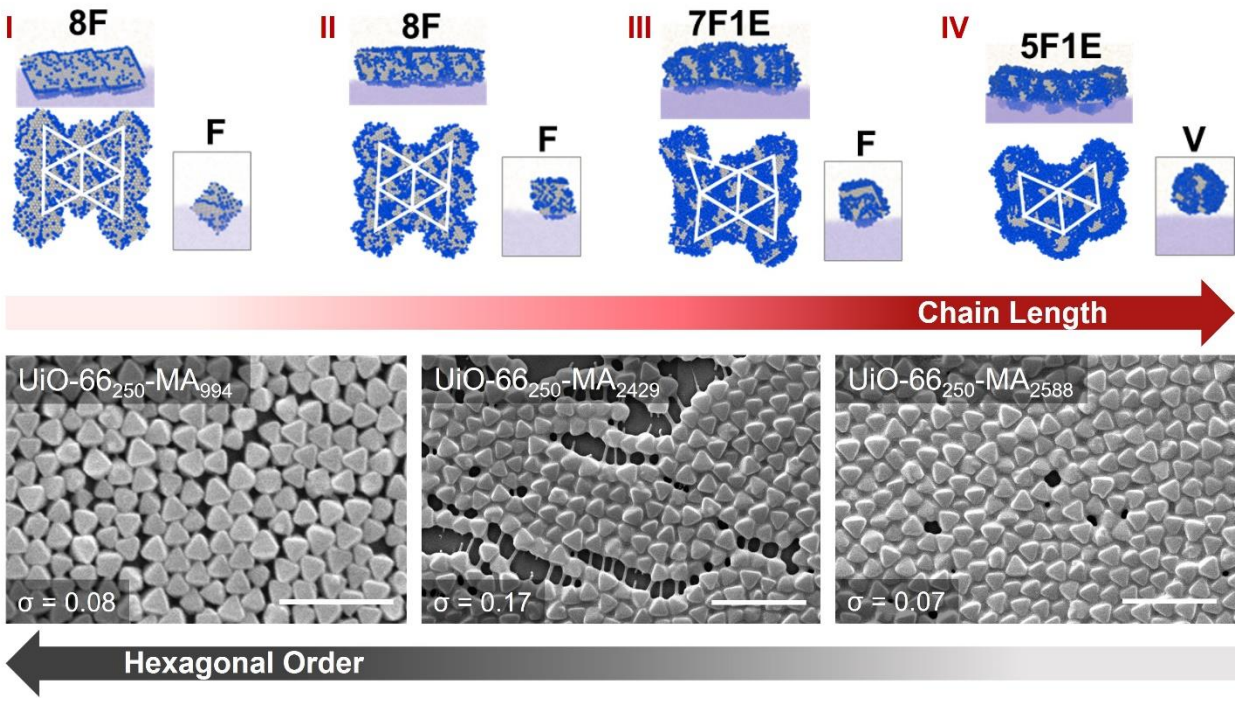

Figure 3S.11. Comparison of simulation and experimental self-assembly showing decreasing hexagonal order with increasing polymer length. Side and top view of structures assembled with MOFs of increasing: graft lengths $L_g = 1\sigma_{CG}$, $2\sigma_{CG}$, $4\sigma_{CG}$, and $6\sigma_{CG}$ for fixed MOF size $L_{MOF} = 13\sigma_{CG}$ and graft hydrophilicity $\lambda = 0.2$ (*top panel*); SEM images of self-assembled films of UiO-66_{250}-MA$_n$, scale bars are 1 μm (*bottom panel*).

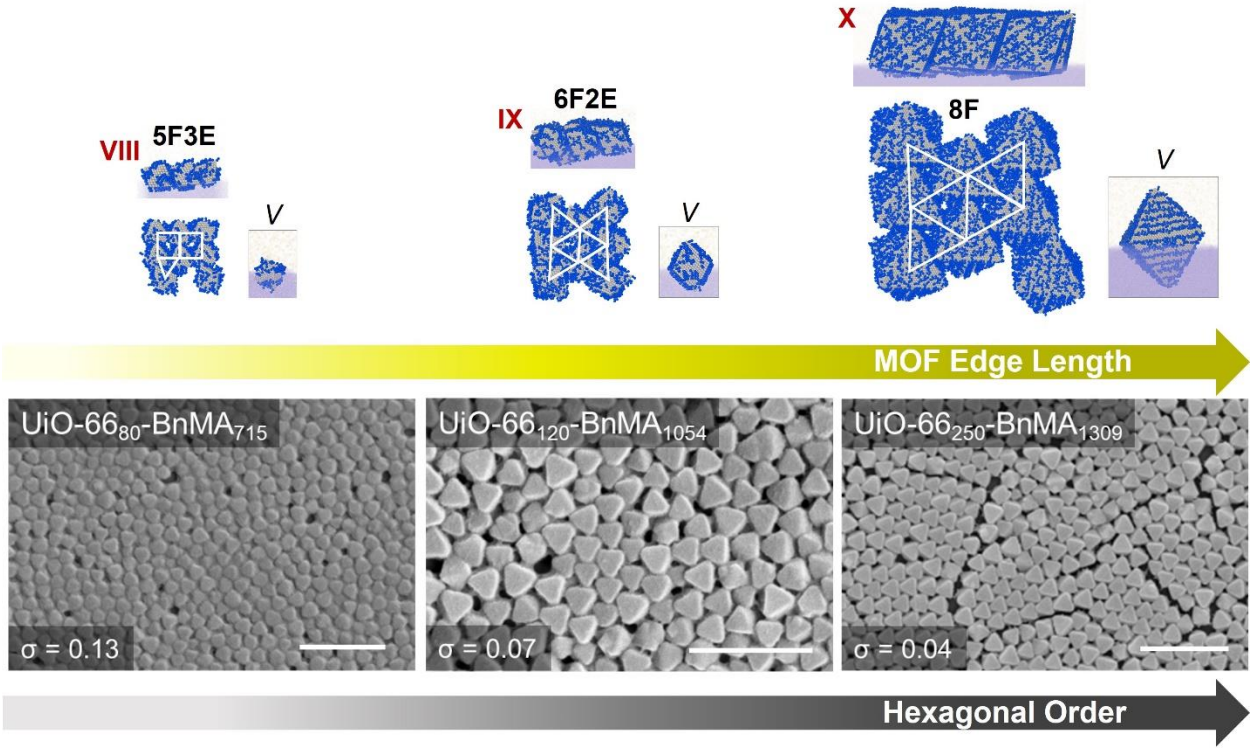

Figure 3S.12. Comparison of simulation and experimental self-assembly showing increasing hexagonal order with increasing particle size. Side and top view of structures assembled with MOFs of increasing edge length $L_{MOF} = 9\sigma_{CG}, 13\sigma_{CG}$, and $28\sigma_{CG}$ for fixed $L_g = 2\sigma_{CG}$, $\lambda = 0.4$ (*top panel*). Insets show the orientation adopted by a single, isolated MOF particle. SEM images of self-assembled films of UiO-66$_x$-BnMA$_n$, scale bars are 500 nm (left, middle) and 1 μm (right) (*bottom panel*).

3.5 Acknowledgements

Chapter 3, in part, is a reprint of the material "Influence of Polymer Characteristics on the Self-Assembly of Polymer-Grafted Metal–Organic Framework Particles" ACS Nano **2022**, *16*, 18168-18177. The dissertation author was the primary author of this manuscript and gratefully acknowledges the contributions of coauthors Po-An Lin, Yilong Zhou, Gaurav Arya, and Seth M. Cohen.

3.6 References

1. Wang, X.-G.; Cheng, Q.; Yu, Y.; Zhang, X.-Z., Controlled Nucleation and Controlled Growth for Size Predicable Synthesis of Nanoscale Metal–Organic Frameworks (MOFs): A General and Scalable Approach. *Angew. Chem. Int. Ed.* **2018,** *57*, 7836-7840.

2. Cavka, J. H.; Jakobsen, S.; Olsbye, U.; Guillou, N.; Lamberti, C.; Bordiga, S.; Lillerud, K. P., A New Zirconium Inorganic Building Brick Forming Metal Organic Frameworks with Exceptional Stability. *J. Am. Chem. Soc.* **2008,** *130*, 13850-13851.

3. Perrier, S., 50th Anniversary Perspective: RAFT Polymerization—A User Guide. *Macromolecules* **2017,** *50*, 7433-7447.

4. Barcus, K.; Cohen, S. M., Free-standing metal–organic framework (MOF) monolayers by self-assembly of polymer-grafted nanoparticles. *Chem. Sci.* **2020,** *11*, 8433-8437.

5. Zheng, Z.; Ling, J.; Müller, A. H. E., Revival of the R-Group Approach: A "CTA-shuttled" Grafting from Approach for Well-Defined Cylindrical Polymer Brushes via RAFT Polymerization. *Macromol. Rapid Commun.* **2014,** *35*, 234-241.

6. Michalek, L.; Barner, L.; Barner-Kowollik, C., Polymer on Top: Current Limits and Future Perspectives of Quantitatively Evaluating Surface Grafting. *Adv. Mater.* **2018,** *30*, 1706321.

7. Bhattacharjee, S., DLS and zeta potential – What they are and what they are not? *J. Controlled Release* **2016,** *235*, 337-351.

8. Favier, A.; Charreyre, M.-T., Experimental Requirements for an Efficient Control of Free-Radical Polymerizations via the Reversible Addition-Fragmentation Chain Transfer (RAFT) Process. *Macromol. Rapid Commun.* **2006,** *27*, 653-692.

9. Shi, W.; Lee, Y. H.; Ling, X. Y.; Li, S., Quantitative prediction of the position and orientation for an octahedral nanoparticle at liquid/liquid interfaces. *Nanoscale* **2017,** *9*, 11239-11248.

10. Lee, Y. H.; Shi, W.; Lee, H. K.; Jiang, R.; Phang, I. Y.; Cui, Y.; Isa, L.; Yang, Y.; Wang, J.; Li, S.; Ling, X. Y., Nanoscale surface chemistry directs the tunable assembly of silver octahedra into three two-dimensional plasmonic superlattices. *Nat. Comm.* **2015,** *6*, 6990.

11. Lee, B. H.-j.; Arya, G., Orientational phase behavior of polymer-grafted nanocubes. *Nanoscale* **2019,** *11*, 15939-15957.

12. Tang, T.-Y.; Zhou, Y.; Arya, G., Interfacial Assembly of Tunable Anisotropic Nanoparticle Architectures. *ACS Nano* **2019,** *13*, 4111-4123.

13. Zhou, Y.; Tang, T.-Y.; Lee, B. H.-j.; Arya, G., Tunable Orientation and Assembly of Polymer-Grafted Nanocubes at Fluid–Fluid Interfaces. *ACS Nano* **2022**.

14. Kremer, K.; Grest, G. S., Dynamics of entangled linear polymer melts: A molecular-dynamics simulation. *J. Chem. Phys.* **1990,** *92*, 5057-5086.

15. Weeks, J. D.; Chandler, D.; Andersen, H. C., Role of Repulsive Forces in Determining the Equilibrium Structure of Simple Liquids. *J. Chem. Phys.* **1971,** *54*, 5237-5247.

16. Plimpton, S., Fast Parallel Algorithms for Short-Range Molecular Dynamics. *J. Comput. Phys.* **1995,** *117*, 1-19.

Chapter 4: Quantifying Ligand Binding to the Surface of Metal-Organic Frameworks

4.1 Introduction

As demonstrated in Chapters 2 and 3, the grafting of polymer chains onto the surface of MOF nanoparticles has proven to be an effective method for creating polymer-MOF hybrid materials. Furthermore, Chapter 3 developed methodologies using a combination of TGA, GPC, DLS, and particle geometry to characterize the surface-bound polymer beyond molecular weight analysis (i.e., grafting density). While these techniques proved capable of estimating the overall structure of the polymer graft, it remained impossible to quantify the initial amount of CTA bound to the MOF surface after coordination. The weight percent of polymer relative to MOF was determined by TGA, but the low molecular weight and abundance of the CTA relative to the organic MOF linker prevented accurate analysis. To determine the amount of surface-bound ligands on MOFs, a method to quantify the surface analyte without interference by the MOF ligand is needed.

In general, the modification of the external surfaces of MOF via coordination chemistry is critical to many features of these materials, particularly the modulation of their nucleation/growth, as well as the immobilization of small-molecules or polymers for a variety of applications.[1-7] Despite many studies that rely on the surface chemistry of MOFs, few studies have quantified these interactions.[8-9] An early study to characterize the surface coordination of ligands to MOFs was described in Chapter 1, where a carboxylate-appended dye was ligated to the surface of a pillared MOF framework.[10] The selective coordination of the dye to carboxylate-terminated facets of the MOF crystal, as well as the lack of functionalization with dye molecules lacking a carboxylate group, showed unambiguously that the presence of the dye was a result of coordination. However, this study only used confocal microscopy to visualize the presence of dye and the amount of dye present was not quantified.

In another study, a method for modifying the external surfaces of Zr(IV)-based MOFs with 1,2-dioleoyl-*sn*-glycero-3-phosphate (DOPA) was described.[11] DOPA was selected because this phosphate-based ligand was expected to coordinate strongly to, but not degrade, the Zr(IV) secondary building units (SBUs) on the surface of $[Zr_6O_4(OH)_4(1,4\text{-bdc})_6]_n$ (UiO-66), $[(Zr_6O_4(OH)_4(1,4\text{-bpdc})_6]_n$ (UiO-67, 1,4-bpdc = 1,4-biphenyldicarboxylate), and $[(Zr_6O_4(OH)_4(4,4'\text{-eddb})_6]_n$ (BUT-30, 4,4'-eddb = 4,4'-(ethyne-1,2-diyl)dibenzoic acid). Upon surface functionalization with DOPA, these MOFs retained their high surface area (indicating only surface functionalization) and became dispersible as colloids in low polarity solvents. Importantly, inductively coupled plasma atomic emission spectroscopy (ICP-AES) and a dye-labeled version of DOPA were used to quantify the amount of DOPA on the surface of the MOFs. It was found that the amount of DOPA modification on the particles correlated with the surface density of the SBUs, with DOPA coverage following the trend UiO-66 > UiO-67 > BUT-30. Taken together, these excellent studies of ligand-directed surface modification of MOFs creates the foundation for evaluating the binding affinities of different ligands to the surface of MOFs.

Using these works as inspiration, Chapter 4 describes a simple and accurate methodology to measure the coordination of small molecule ligands to the surface of three MOFs: UiO-66, MIL-88B-NH_2, and ZIF-8. In these experiments, the MOF surface is treated as an extended coordination compound where the binding of ligands is directed to the metal ion nodes (i.e., SBUs, Figure 4.1). Carboxylate- or imidazole-appended BODIPY dyes were bound to the surface of the MOFs. By monitoring the displacement of these dyes by a range of small molecule ligands, apparent binding constants could be measured. Ligands showed clear differences in their ability to displace the bound dyes as a function of denticity, donor ability, and ligand compatibility with the SBU structure/composition. The observed trends suggest that the basic principles of

coordination chemistry provide a reasonable framework for conceptualizing the binding of these molecules to the surface of MOFs. Additionally, it provides a simple, accurate methodology to study the surface modification of MOFs which can be used for small molecules (such as the CTAs in Chapters 2 and 3) as well as synthetic polymers or other macromolecules.

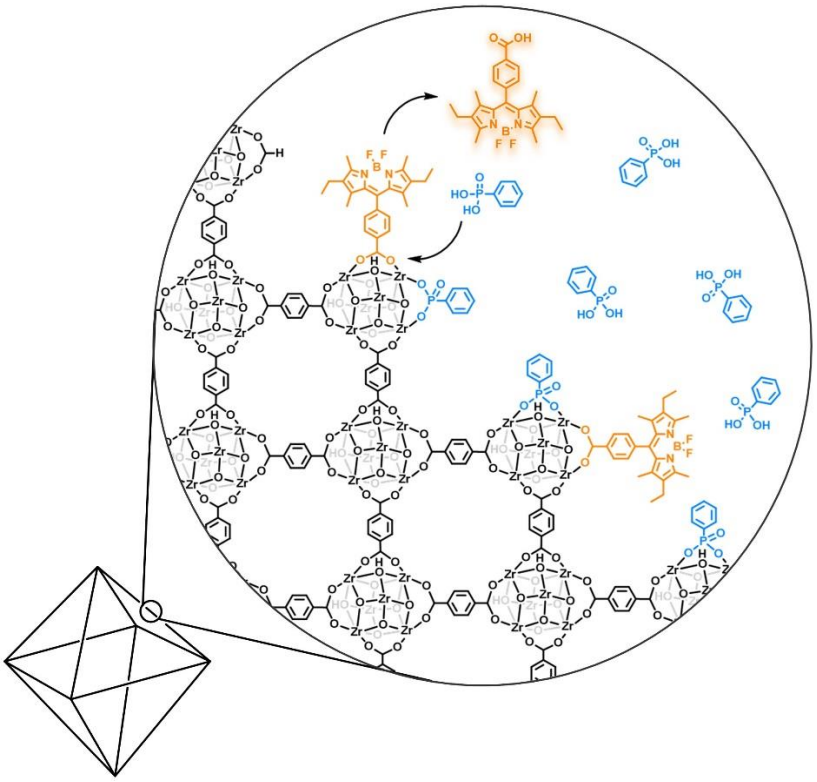

Figure 4.1. Conceptual illustration of surface exchange between coordinating ligands.

4.2 Results and Discussion

The initial investigation into surface functionalization was conducted with UiO-66. UiO-66 nanoparticles were prepared using a previously reported method to prepare multigram quantities of monodisperse particles with a uniform size distribution and octahedral morphology as imaged by scanning electron microscopy (SEM, Figure 4S.1).[12] Powder X-ray diffraction

(PXRD) of the recovered particles matched the simulated data of the crystal structure (Figure 4S.2) and surface area measurements are consistent with previously reported values (Figure 4S.3)

To probe the surface binding of UiO-66, two dyes were initially prepared, 4,4-difluoro-8-(4-carboxyphenyl)-1,3,5,7-tetramethyl-2,6-diethyl-4-boron-3a,4a-diaza-s-indacene ($BODIPY_{COOH}$), which contains a carboxylate group capable of coordinating the zirconium cluster of UiO-66, and 2,6-diethyl-4,4-difluoro-1,3,5,7-tetramethyl-8-(4-methylphenyl)-4-bora-3a,4a-diaza-s-indacene ($BODIPY_{Me}$), which was used as a non-coordinating control (Figure 4.2, Scheme 4S.1, see SI for details).[13] While many dyes could be used for MOF surface binding, $BODIPY_{COOH}$ provided several advantages, including: it is soluble in most non-polar organic solvents, it is amendable to further chemical modification (see below), it is not readily photobleached, it has a high molar absorptivity (ε = 69,094 $M^{-1}cm^{-1}$) that is easily measured at low concentrations, and the λ_{max} of 524 nm is well beyond the absorbance of solvents and the organic ligands that are used to construct the MOF (Figure 4S.4).

Stock solutions of $BODIPY_{COOH}$ and $BODIPY_{Me}$ were prepared in DMF at a concentration of 4 μM, and 1 mL of the dye stock solution was added to separate suspensions of 20 mg UiO-66 in 1 mL DMF (Figure 4.2). The solutions were vigorously mixed and left to stand overnight, after which the particles were collected by centrifugation and thoroughly washed with DMF to remove any residual dye. Photographs of the samples after the initial centrifugation show a clear difference between the two samples (Figure 4.2b-c). The supernatant of the particles treated with $BODIPY_{Me}$ was colored and the dye was easily removed from the MOF after washing with DMF. By contrast, the supernatant of the particles treated with $BODIPY_{COOH}$ was colorless while the UiO-66 particles became a bright orange color that persisted even after extensive washing. These results suggest dye coordination is occurring at the SBUs and that the dye was not bound to the MOF by weak,

non-covalent interactions to the crystal surfaces or trapping of the dye in the pores of the MOF. The kinetics of $BODIPY_{COOH}$ coordination to the surface of UiO-66 was also investigated. MOF particles were isolated, washed, and analyzed 10 min, 1 h, and 24 h after the addition of dye. Absorption measurements of the digested particles show that the surface modification is rapid, with ~80% of the maximum dye coordination (based on coverage at 24 h) occurs within the first 10 min (Figure 4S.5).

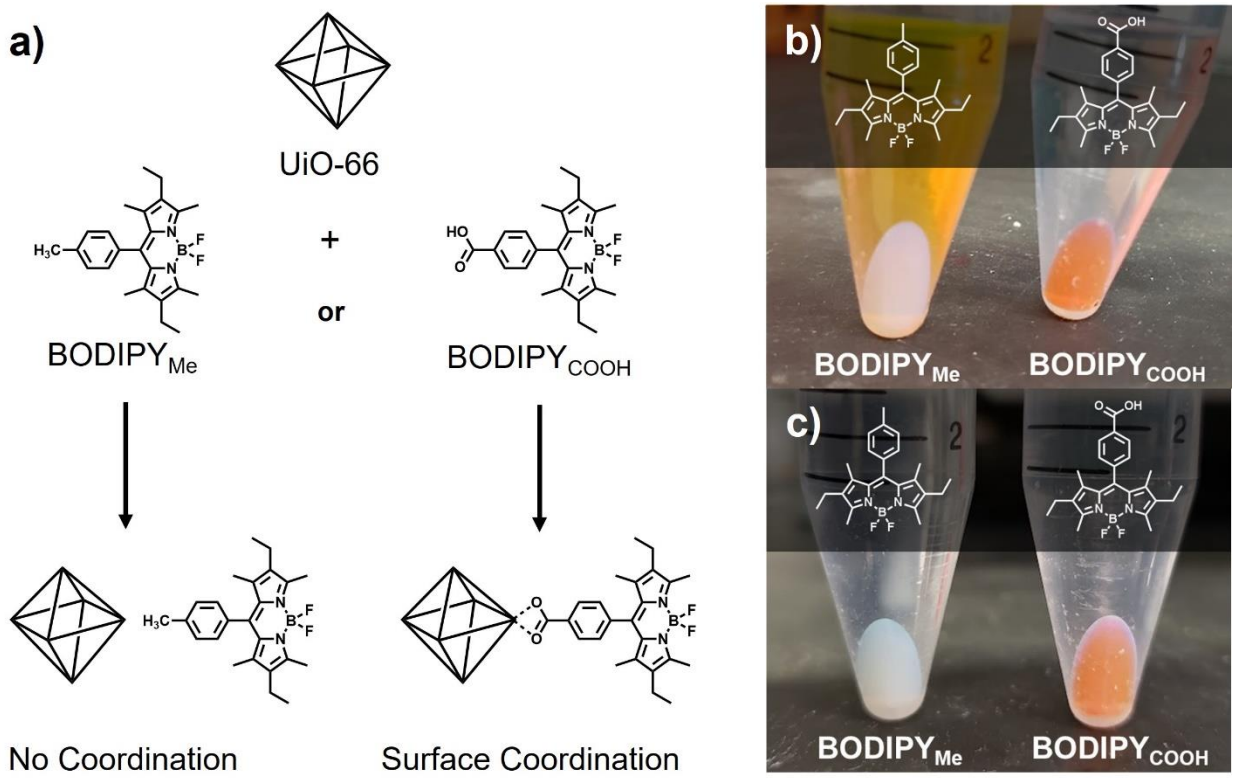

Figure 4.2. a) Scheme of proposed dye interaction with UiO-66. b) Image of UiO-66 particles 24 h after dye addition. c) Image of isolated UiO-66 particles after multiple wash cycles with DMF.

While the $BODIPY_{COOH}$ could not be easily washed from the MOF surface, it was observed that if UiO-66-$BODIPY_{COOH}$ was suspended in DMF for 24 h, the supernatant solution gradually became colored over time, indicating dissociation of the dye from the MOF surface. Having

observed this, the effect of different solvents on the stability of dye coordination and rate of dye removal was tested by examining the amount of dye present in the supernatant of UiO-66-$BODIPY_{COOH}$ particles after dispersion (Figure 4.3). The particles were first dispersed in different solvents, and then pelleted by centrifugation at different time points: immediately after dispersing (t = 0), 1 h, and 24 h, after which the supernatant was removed to determine the concentration of dye by UV-visible spectroscopy. It should be noted that all solvents were standard ACS grade, used as received, and no special precautions were taken to protect the solvents from atmosphere. The results show that solvent plays a significant role in the stability of dye coordination, with acetone, acetonitrile, and DMF resulting in the lowest degree of dye removal. Surprisingly, water, which many MOFs are not structurally stable in, was ineffective at removing the dye. This is most likely due to the low water solubility of the dye, which inhibits dissociation from the MOF surface.

For alcohol solvents, an initial, relatively large dye displacement was observed (at t = 0 and 1 h), but then the concentration of dye in solution decreased at 24 h (relative to the 1 h timepoint). With the exception of nBuOH, the concentration of dye in MeOH, EtOH, and iPrOH all equilibrated to nearly the same value. While the reason behind this phenomenon is not fully understood, MeOH is widely used as an activation solvent for UiO-66 due to its distinct ability to remove or exchange loosely coordinated ligands and modulator from the MOF interior.[14] One hypothesis is that MeOH, and to a lesser extent EtOH and iPrOH, facilitates reversible ligand-binding of both the monotopic dye and the ditopic framework ligands (i.e., 1,4-H_2bdc) near the surface. The initial rapid dissociation of dye is followed by a gradual dissociation of 1,4-H_2bdc. Both the dye and 1,4-H_2bdc compete for the newly exposed open metal sites, and the larger steric size and hydrophobicity of the dye may shift the surface coordination equilibrium favorably towards the dye.

Overall, the data in Figure 3 show that UiO-66-BODIPY$_{COOH}$ coordination is most stable in polar, aprotic solvents such as acetone, acetonitrile, and DMF, while nonpolar and polar protic solvents lead to dye loss over time. The higher stability of the coordination in polar aprotic solvents over polar protic solvents suggests that a proton source may facilitate ligand exchange via protonation of the carboxylic acid on the coordinating dye. A similar mechanism was proposed and verified computationally in a previously reported study.[15] As no attempt was made to rigorously exclude water from the solvents, ligand displacement could occur in aprotic solvents as well. However, the reason for the low dye stability in nonpolar, aprotic EtOAc and glyme is unclear. It may be that the weak metal-coordinating ability of these solvents could manifest as dye loss when present in high concentrations (i.e., as a solvent). Based on the solvent stability (Figure 4.3) acetonitrile and acetone were considered the best solvents for titration experiments. Acetonitrile proved ineffective at solubilizing several of the compounds used in subsequent experiments (see below); therefore, acetone was used for all further experiments to minimize solvent effects on dye coordination.

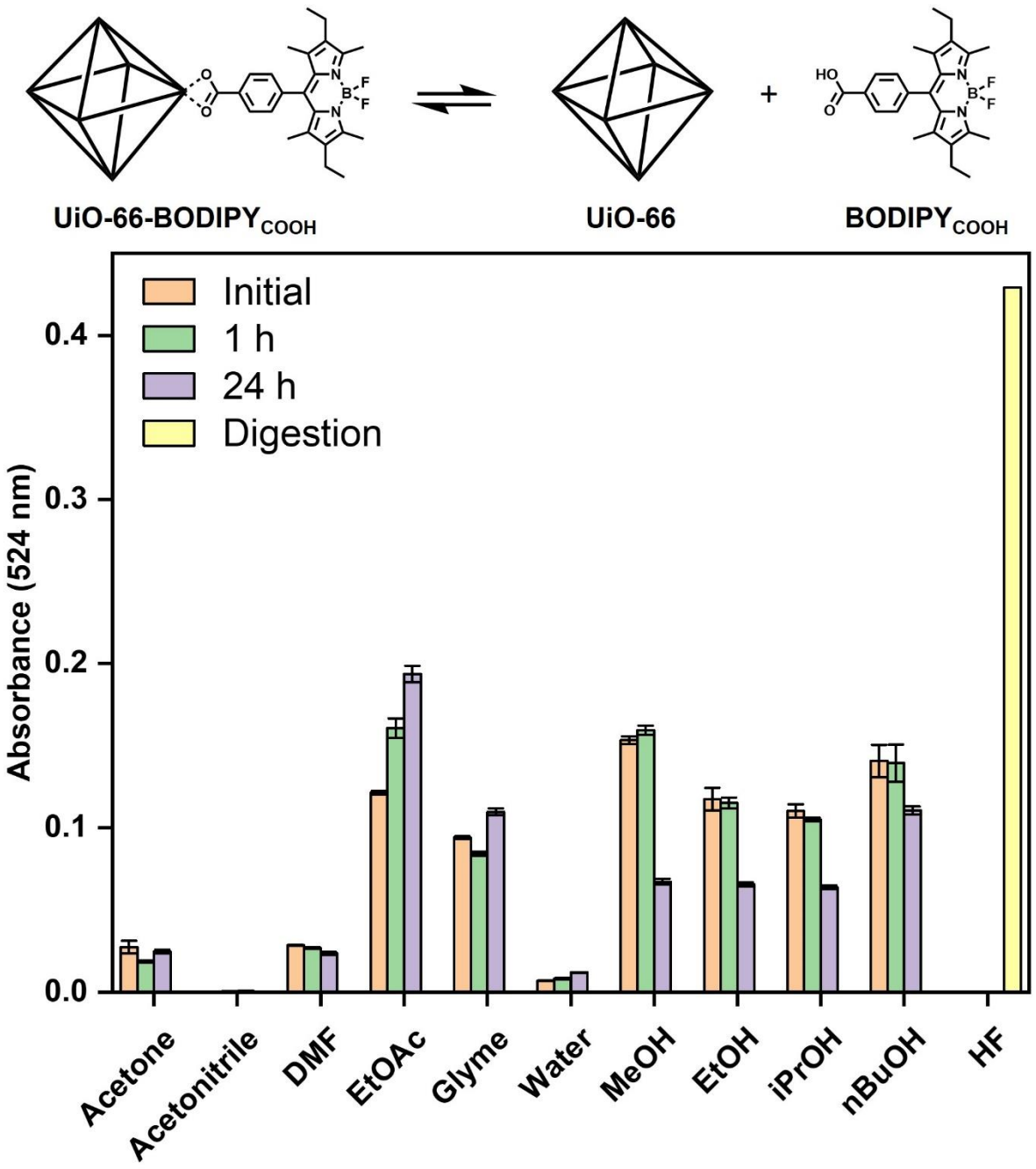

Figure 4.3. Solvent stability of BODIPY$_{COOH}$ coordination to UiO-66. After centrifugation at each time point, UV-visible spectroscopy measurements of the supernatant at 524 nm were used to determine the amount of dye removed from the MOF surface.

Having established a suitable solvent system to study ligand binding, the inherent reversibility of BODIPY$_{COOH}$ coordination to the surface of UiO-66 was used as a tool to measure

the relative binding affinity of a variety of ligands to UiO-66. To achieve this, an initial screening of ligands was performed to determine the general structural and chemical features that result in dye displacement (Figure 4.4). The initial examination was designed to evaluate ligand binding at a single concentration. UiO-66-BODIPY$_{COOH}$ in DMF was first solvent exchanged with acetone and diluted to a concentration of 4 mg/mL. Individual Eppendorf tubes were prepared with 1 mL of the MOF suspension to which 10 µL of ligand stock solutions (prepared at 10 mM in acetone) was added (approximately 62:1 ligand to surface dye ratio). The solutions were promptly mixed and left to equilibrate for 24 h, after which the particles were collected by centrifugation and the amount of dye displaced was determined by UV-visible spectroscopy measurements on the supernatant. The displacement by each ligand was then compared relative to two control samples of UiO-66-BODIPY$_{COOH}$ with either: no treatment (**NT**) or complete ligand displacement by digestion of the MOF using HF (labeled **HF**, Figure 4.4).

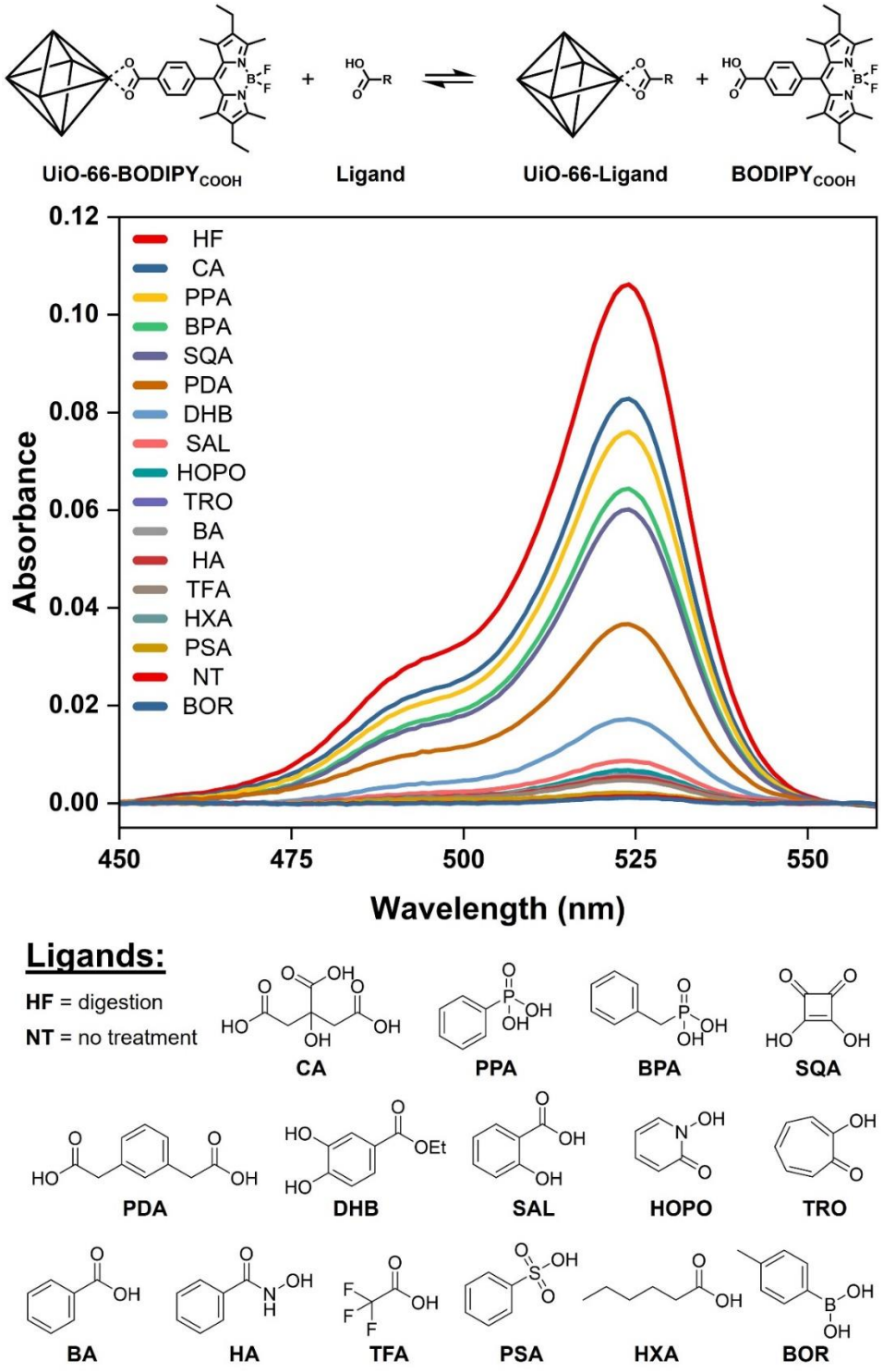

Figure 4.4. UV-visible spectra of UiO-66-BODIPY$_{COOH}$ solution supernatants after treating with various ligands. Greater absorbance corresponds to stronger ligand binding affinity (i.e., greater dye displacement).

Simple carboxylic acid ligands of different acidities (**BA**, **HXA**, **TFA**) showed only a small amount of dye displacement in the single concentration experiment. However, multitopic carboxylic acids showed a very high binding affinity, with the tritopic citric acid (**CA**) providing the highest relative dye displacement of all the ligands tested. Phosphonates and phosphates are well-known for their ability to form strong coordination bonds to metal oxides, which has led them to be widely used in the surface functionalization of many materials, including UiO-66 and zirconium oxide nanoparticles.[5, 11, 16] Their affinity was confirmed here as both the monofunctional phenylphosphonic acid (**PPA**) and benzylphosphonic acid (**BPA**) were comparable in binding strength to **CA** and stronger than ditopic carboxylic acid (**PDA**). In contrast, hydroxamic acid (**HA**), 2-hydroxypyridine *N*-oxide (**HOPO**), and catechol (**DHB**), all ligands also known for strong metal chelation to hard Lewis acids like Zr(IV), were relatively poor ligands, resulting in only slightly higher dye displacement than the monotopic carboxylic acids. The weak binding of these ligands when compared to the phosphonates demonstrates the value of this methodology, as it allows for the relative binding strength of different ligands to be quickly confirmed, and in doing so provide insight for the similarities and differences in MOF surface chemistry when compared to classical coordination complexes based on the same metal ions.

Interestingly, while ligand pK_a could contribute to dye displacement by simple protonation of the carboxylate ligand of the BODIPY dye, the results in Figure 4.4 indicate that the strength of the resulting metal-ligand bond is more important than acidity. This can be illustrated by comparing the high dye displacement of the phosphonic acids (**PPA** and **BPA**, pK_a = 1.2, 1.8, respectively) when compared to the negligible binding of phenylsulfonic acid (**PSA**, pK_a = 1.4). The negligible role of ligand acidity is further supported by the comparable dye displacement effect obtained with trifluoroacetic acid (**TFA**, pK_a = 0.3), benzoic acid (**BA**, pK_a = 4.2), and hexanoic

acid (**HXA**, pK_a = 5.0). However, it should be noted that these pK_a values are measured in water while the experiments performed here are reported in acetone. As such, the true pK_a of these ligands is unknown and the effect of acidity cannot be unambiguously confirmed by these results alone. While experiments in water would be of interest, the insolubility of the dye used in these studies prevents these titrations under the current experimental conditions.

To get a more refined comparison of the relative ligand affinities for UiO-66, a subset of the ligands (Figure 4.5) was selected for additional titration experiments where dye displacement was monitored as a function of ligand concentration.

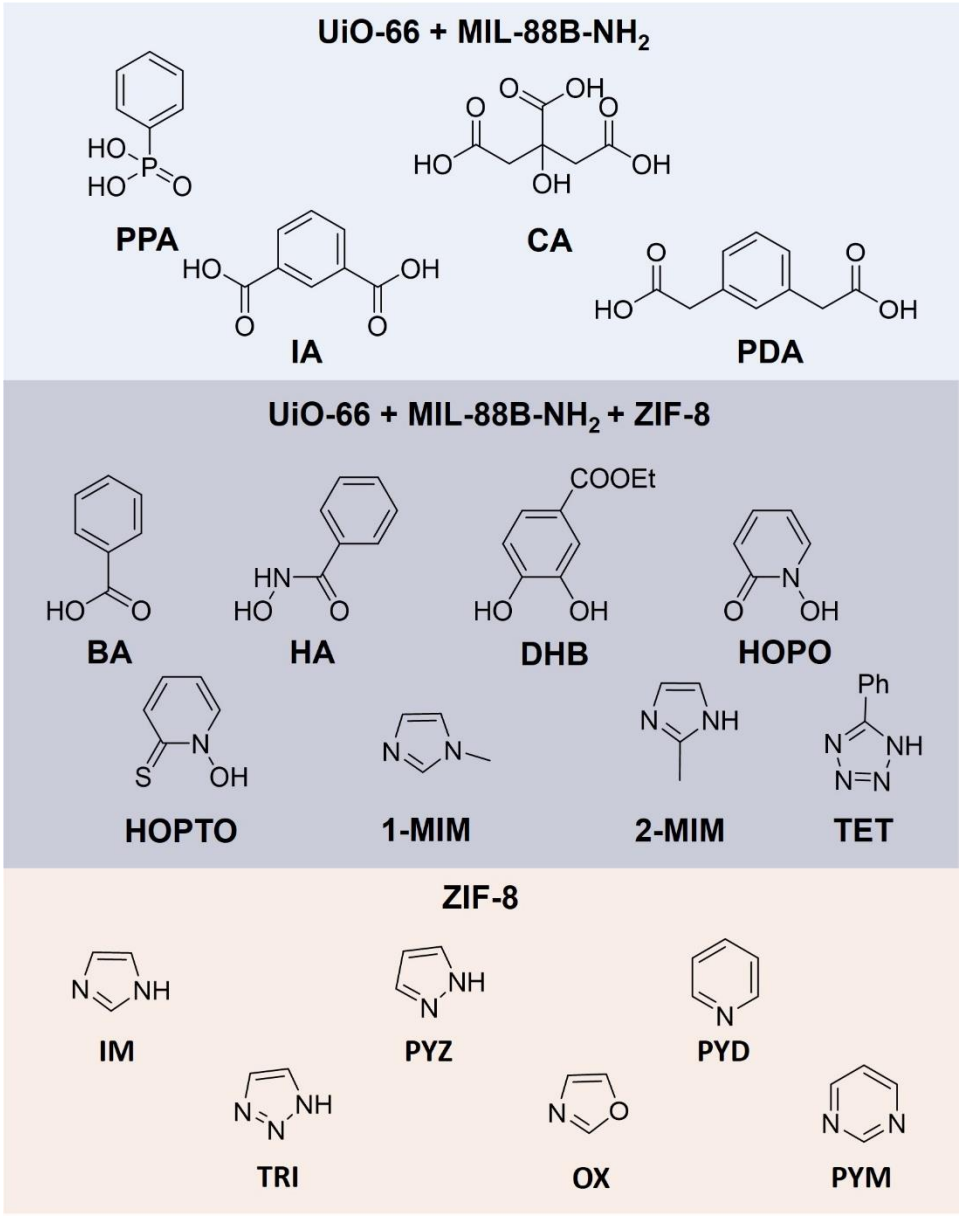

Figure 4.5. Ligands used for competitive binding titration experiments and the dye-coordinated MOFs they were tested with. Ligands in the middle box were used for all MOFs in the study for direct comparison.

To determine the apparent binding constants of each ligand, the same experimental setup as performed for the single-point screen was used. In this case, the concentration range studied was prepared by serial dilutions of ligand stock solutions and each concentration was measured in triplicate. The absorption of the supernatant at each concentration was then plotted as a function

of concentration and the points were fit with a sigmoidal curve (Figure 4S.6, 4S.7 see SI for details). The concentration at the inflection point of the curve for each ligand was found and the inverse of this concentration is taken as the apparent binding constant, (inset table, Figure 4.6). It should be stressed that, for ease of visual comparison the curves from the sigmoidal fits shown in Figure 4.6 have been normalized; however, the values for the apparent binding constant are taken directly from the original, raw titration data (Figure 4S.7). As expected, the titrations show that the trends in apparent ligand affinity follow the results of the single point experiments (Figure 4.4). Citric acid (**CA**) and phenylphosphonic acid (**PPA**) show apparent binding constants (K_{ap}) 4× and 3× larger than the next best ligand, respectively. However, the relative difference in affinity between benzoic acid (**BA**) and the ditopic carboxylic acids (e.g., **PDA**, **IA**) is modest, being slightly greater than 2× (see table inset in Figure 4.6). The amine heterocycles **2-MIM**, **1-MEM**, and **TET** were far weaker ligands, with estimated binding affinity values that are very poor and could only be estimated by the incomplete titration data (>1 M, Figure 4S.7). To ensure dye displacement was not a result of MOF degradation, SEM imaging was performed on particles post-treatment. Apart from **PPA** and **HOPO**, the structure of UiO-66 remained unchanged for all ligands throughout the concentration range tested (Figures 4S.8 and 4S.9). For **PPA** and **HOPO,** significant restructuring or total dissolution of the UiO-66 particles was observed at the highest concentrations (Figure 4S.10). However, no visible change to the MOF particles was observed at concentrations along the inflection points of the titration curves was noted (Figure 4.6), indicating that the structure of the MOF remains unchanged. Overall, these data are valuable for identifying ligands that might be best suited to functionalize a MOF particle or modulate MOF growth under select reaction conditions. To confirm this, $BODIPY_{COOH}$ was modified with a phosphonic acid group using standard amide coupling to form $BODIPY_{PHOS}$. Given the much higher binding

affinity of the phosphonate group over carboxylate, $BODIPY_{PHOS}$ was expected to show both greater solvent stability and require significantly higher concentrations of competitive ligands to displace from the MOF surface. Indeed, $BODIPY_{PHOS}$ coordination to UiO-66 was far more stable, with only small amounts of displacement occurring in alcohols and negligible displacement in all other solvents (Figure 4S.11). Competitive binding experiments were even more compelling, where examination of a subset of ligands showed that none of the ligands were capable of displacing the $BODIPY_{PHOS}$ except **PPA** and to a much lesser extent **CA** and **HA** (Figure 4S.12). In the case of **PPA**, the concentrations at which dye displacement was detected was above the point at which MOF degradation occurs. This highlights the role of coordination chemistry in MOF surface modification and that with the selection of a strong ligand functionalization of the MOF can be considered extremely stable (on par with MOF stability).

The same methodology described for UiO-66 was applied to study ligand binding to MIL-88B-NH_2, a MOF comprised of trimeric Fe(III) SBUs and amino-terephthalic acid linkers (H_2bdc-NH_2) with a hexagonal rod morphology (Figures 4S.13 and 4S.14).[17] After functionalization with $BODIPY_{COOH}$, the solvent stability procedure was repeated using the same solvents as were used for UiO-66 (Figure 4S.16) and concentration-dependent ligand binding (Figure 4.7) was performed using the same ligand set as UiO-66 (Figure 4.5) in acetone. The ligands 2-mercaptpyridine *N*-oxide (**HOPTO**) and hydroxamic acid (**HA**) partially dissolved this MOF at high concentrations forming brightly colored complexes (i.e., resulting in the deeply colored Fe(**HOPTO**)$_3$ complex when the titration was attempted with **HOPTO**), making determination of apparent binding affinities impossible with these compounds. When comparing the results of the MIL-88B-NH_2 to UiO-66, the order of ligand strength is similar, with both **CA** and **PPA** remaining the tightest binding ligands. However, the absolute values for the apparent binding constant of the ligands are

much higher in the case of MIL-88B-NH_2. This is possibly due to the weaker coordination of carboxylates to Fe(III) over Zr(IV). SEM images of the particles after ligand treatment showed that MIL-88B-NH_2 was similarly stable to ligand treatment at relevant concentrations (Figure 4S.18). Degradation was most apparent with **DHB** and **HOPO**, but only at concentrations well above complete dye displacement (Figure 4S.19).

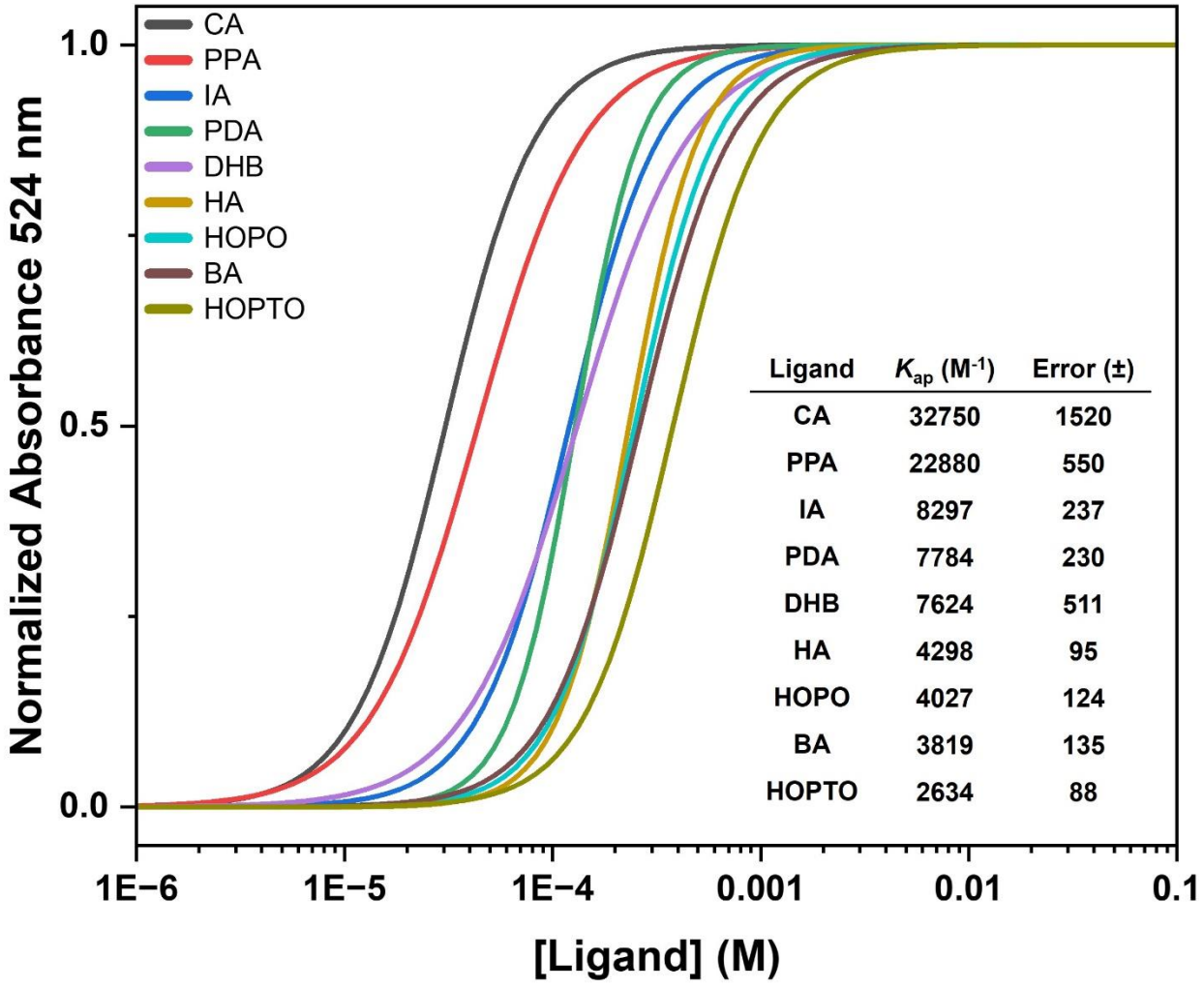

Figure 4.6. Normalized titration curves of UiO-66-$BODIPY_{COOH}$ with increasing concentrations of select ligands (Figure 4.5, top and middle). Inset table gives the ligand, apparent binding constant (K_{ap}), and error values.

Finally, zeolitic imidazolate framework 8 (ZIF-8) was examined for dye displacement. ZIF-8 is comprised of individual Zn(II) ions bridged by 2-methylimidazole ligands. The binding

strength of carboxylate ligands to the mononuclear Zn(II) SBUs is weaker than imidazole ligands, as reasoned by hard-soft Lewis acid-base theory. As the purpose of this study was to determine the strength of ligand binding to the surface of the native MOF, the $BODIPY_{COOH}$ dye was modified with histamine using standard amide coupling methods to form $BODIPY_{Im}$. The same process for dye coordination, solvent stability, ligand screening, and ligand titrations was performed on ZIF-8 (Figures 4S.23 and 4S.24).

Six heterocycles were chosen for the titration experiments, including eight that were used for UiO-66 (Figure 4.5, middle and bottom). The curve fittings from the titration and the corresponding K_{ap} values are shown in Figure 4S.24 and Table 4S.1. Unlike UiO-66 and MIL-88B-NH_2, most of the ligands showed very weak binding to ZIF-8. Additionally, SEM imaging of the particles after titration with the two strongest ligands **HOPO** and **TET** clearly show that the observed dye displacement is a result of particle degradation, although the particles were remarkably stable to more basic ligands such as 2-methylimidazole (**2-MIM**) and imidazole (**IM**) (Figure 4S.25). As a result of the weak binding, none of the ligands tested displaced the dye to a significant value within the concentration range tested. While this precludes the determination of accurate apparent binding constants (values in Table 4S.1 are best fits based on incomplete titrations), many of the titration curves show sufficient differences that some general observations can be made for ZIF-8. The binding of ligands to ZIF-8 shows a clear preference for 5-membered heterocycles when compared to similar 6-membered rings. This is clearly demonstrated by the strongly binding imidazoles (**IM**, **2-MIM**) by comparison to pyrimidine (**PYM**), despite having the same 1,3-*N*,*N* donor arrangement. In addition, the ability of the heterocycle to act as a bidentate, bridging ligand also appears important. 5-Membered rings with only a single amine available for binding, such as *N*-methyl imidazole (**1-MIM**) and oxazole (**OX**), are among the

weakest ligands for ZIF-8 (Figure 4S.24 and Table 4S.1). These results suggest that the binding by $BODIPY_{Im}$ to the ZIF-8 surface likely occurs via a bridging coordination mode using both nitrogen donor atoms, and as such dye displacement requires a similarly strong binding mode to displace the dye from the surface. SEM imaging of the particles after treatment with many ligands also shows large changes in ZIF-8 morphology, indicative of MOF degradation (Figure 4S.25). In the case of **TET** at 14.3 mM, the images show the formation of much larger particles with a distinctly hollow, intergrown morphology. While extensive characterization was not performed, PXRD of recovered solid indicates the particles remain crystalline but are not ZIF-8 (Figure 4S.26).

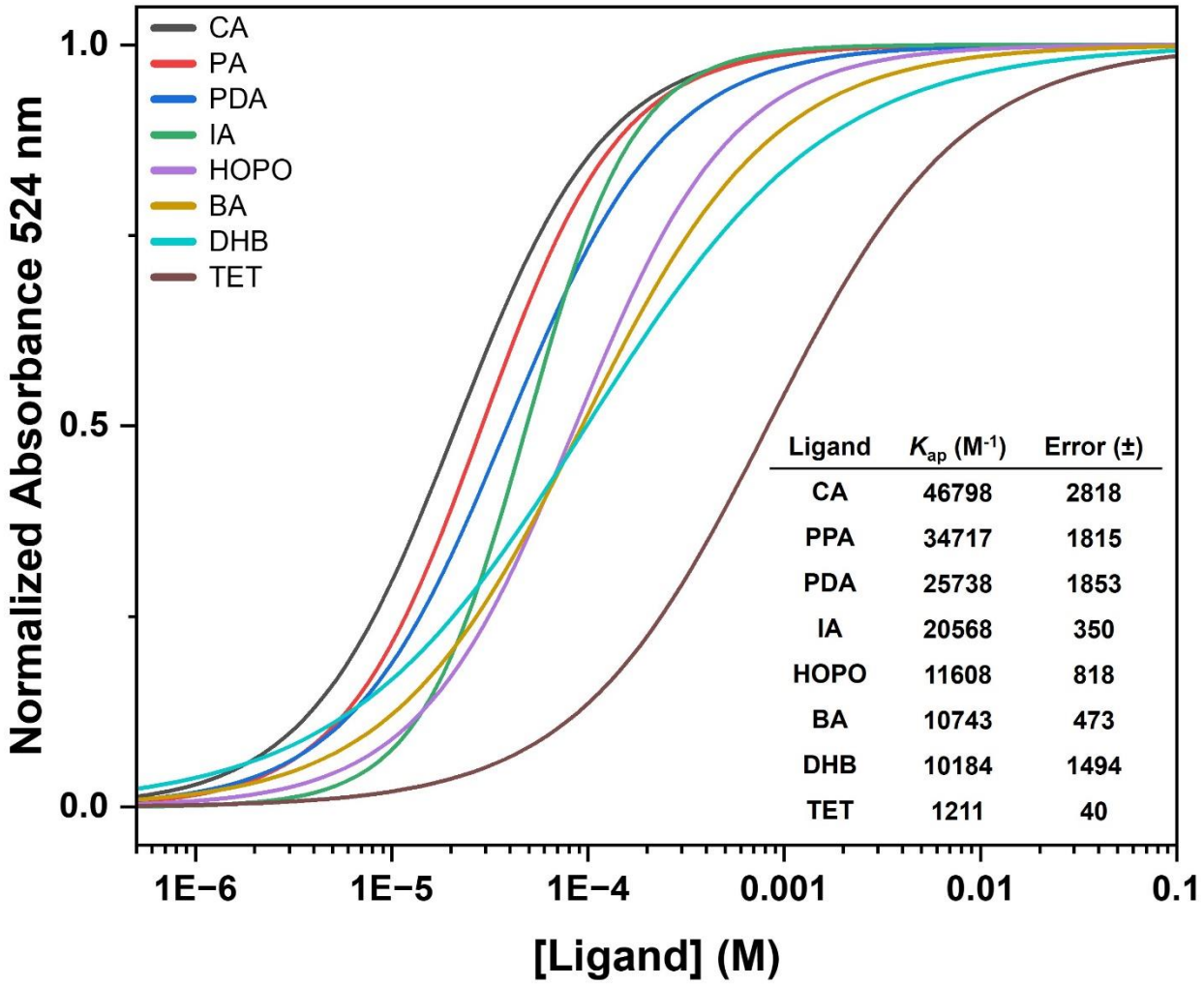

Figure 4.7. Normalized titration curves of MIL-88B-NH_2-$BODIPY_{COOH}$ with increasing concentrations of select ligands (Figure 4.5, middle and bottom). Inset table gives the ligand, apparent binding constant (K_{ap}), and error values.

4.3 Conclusion

In conclusion, a simple methodology to measure and quantify the relative binding strength and apparent binding constant of ligands to the surface of MOFs has been developed. By first coordinating a BODIPY dye to the surface of the MOF, the addition of exogenous ligands to compete with the dye for coordination at the MOF surface allows for a means to measure relative binding constants. In this first report, UiO-66, MIL-88B-NH_2, and ZIF-8 were examined as test cases with more than a dozen ligands. With the surface modification of MOFs becoming

increasingly important for the field, the methods described here should help advance the understanding and manipulation of MOF surfaces, and aid in efforts to optimize conditions for MOF surface modulation and functionalization. Importantly, the findings here suggest that the MOF surface can be considered much as an extended coordination compound, which lends itself to rational design and selection of surface modifying groups.

In Chapter 2, surface-initiated controlled radical polymerization was demonstrated to be a practical methodology to prepare polymer-grafted MOFs, while the self-assembly of these materials allows for the preparation of monolayer thin-films. Chapter 3 explored the full characterization of these materials as a way to understand and explain the self-assembly and physical properties of the self-assembled monolayers through the structure of the polymer brush. In Chapter 4, the surface coordination of MOFs by various ligands is quantified, which had been overlooked in the previous Chapters. In doing so, the process of MOF PSP using SI-CRP from coordinating initiators can be understood in detail, from the precise amount of the initial surface modification with the catechol-CTA to the structure of the grafted polymer brush and its effect on interfacial self-assembly. The methodologies developed throughout this work are intended to serve as a guide for future research in the field of MOF-polymer composites. They provide both the analytical framework and practical tools necessary to prepare and thoroughly characterize these intricate materials. Using these strategies, future researchers will be better equipped to create the next generation of advanced, multifunctional materials.

4.4 Appendix: Supporting Information

Materials

All solvents were purchased from either Millipore Sigma or Fisher Scientific of ACS Grade (< 0.2% H_2O minimum) and used as received. No special precautions were taken to prevent exposure to atmospheric moisture. 3-Ethyl-2,4-dimethylpyrrole (97%) was purchased from TCI and monomethyl terephthalate was purchased from Combi-Blocks and used as received.

Characterization

Nuclear Magnetic Resonance. Proton nuclear magnetic resonance spectra (^{1}H NMR) were recorded on a JEOL ECA 500 spectrometer (500 MHz). Chemical shifts are reported in parts per million (ppm) referenced to the appropriate solvent peak.

Powder X-Ray Diffraction (PXRD). Dry MOF powder (~50 mg) was loaded into a small-well steel sample holder. PXRD was collected at ambient temperature on a Bruker D8 Advance diffractometer at 40 kV, 40 mA for Cu *K*a (l = 1.5418 Å), with a scan speed of 2 sec/step, a step size of 0.05° in 2θ, and a 2θ range of 2-50°.

Scanning Electron Microscopy (SEM). MOF particles were suspended in acetone (~1 mg/mL) and spotted onto silicon wafers using a thin glass capillary. The silicon wafers were mounted on an aluminum sample holder disk with carbon tape and coated using an Ir-sputter coating. A FEI Apreo SEM instrument was used for acquiring images using an accelerating voltage of 5 kV under vacuum at a working distance at 10.0 mm.

BET Surface Area Analysis. Samples for analysis were evacuated on a vacuum line overnight at room temperature prior to analysis. Samples (~50 mg) were then transferred to pre-weighed

sample tubes and degassed at 105 °C on a Micromeritics ASAP 2020 Adsorption Analyzer for a minimum of 12 h or until the outgas rate was <5 mmHg. After degassing, the sample tubes were re-weighed to obtain a consistent mass for the samples. BET surface area (m^2/g) measurements were collected at 77 K with N_2 on a Micromeritics ASAP 2020 Adsorption Analyzer using volumetric techniques.

UV-visible Spectroscopy. Solutions were prepared in the indicated solvent and 1 mL was transferred to a 1.5 mL semi-micro cuvette with a 1 cm path length. An Agilent Cary 60 was used to acquire spectra with a scan rate 2400 nm/s. Molar absorption coefficients were determined from serial dilutions of a stock solution and repeated in triplicate. Cuvettes were purchased from Brandtech Scientific (cat. no. 759165) to ensure compatibility with organic solvents such as acetone and DMF.

Experimental.

Synthesis of BODIPY$_{COOH}$

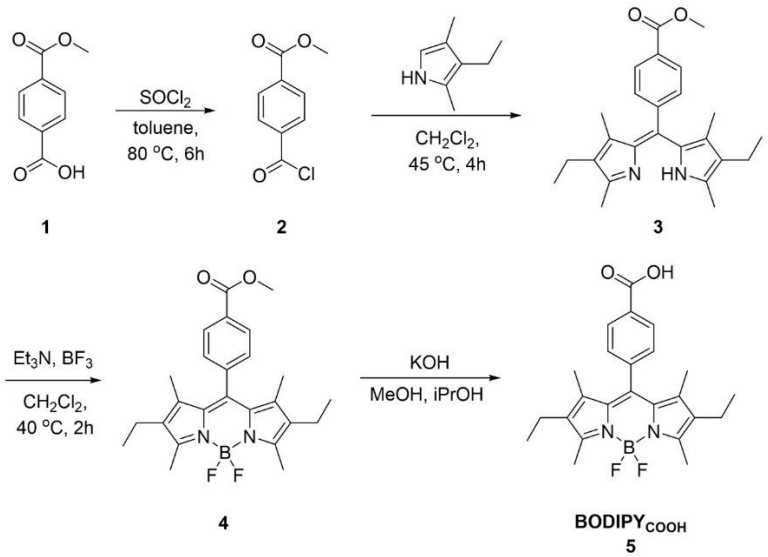

Scheme 4S.1. Synthesis of 4-(4,4-difluoro-1,3,5,7-tetramethyl-3a,4a-diaza-4-bora-*s*-indacen-8-yl)benzoic acid **(5)**.

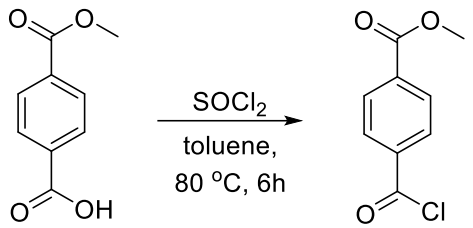

1 **2**

Methyl 4-(chlorocarbonyl)benzoate (2). A 500 mL round bottom flask was charged with monomethyl terephthalic acid (**1**, 25.0 g, 139 mmol, 1 eq.) and 100 mL of toluene. Thionyl chloride (12.2 mL, 167 mmol, 1.2 eq.) and 100 µL DMF was added and the suspension was stirred for 6 h at 80 °C during which the material completely dissolved. The reaction was evaporated to dryness under vacuum and residual thionyl chloride was removed by co-evaporation with dry toluene (2×50 ml) to yield a white solid. The crude product was used for the next reaction without further purification.

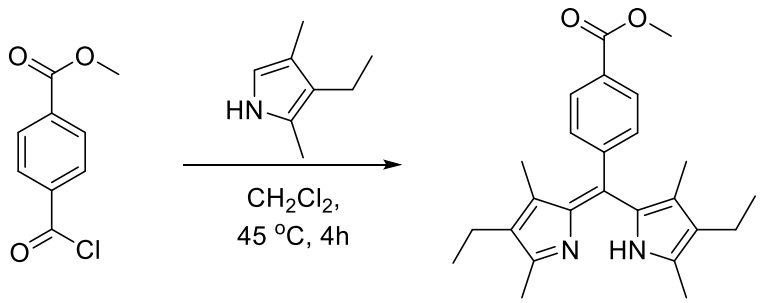

2 **3**

Methyl (*Z*)-4-((4-ethyl-3,5-dimethyl-1*H*-pyrrol-2-yl)(4-ethyl-3,5-dimethyl-2H-pyrrol-2-ylidene)methyl)benzoate (3). The crude acid chloride (**2**) from the previous step (19.0 g, 96 mmol, 2.4 eq.) was directly transferred to a 500 mL round bottom under Ar and 200 mL of dry CH_2Cl_2 was added via cannula. 3-Ethyl-2,4-dimethyl pyrrole (5.48 mL, 41 mmol, 1 eq.) from a

fresh ampule was added via gas-tight syringe dropwise. The reaction mixture was heated to 45 °C for 4 h, after which the reaction mixture was evaporated to dryness under vacuum. The crude product was dry loaded on silica and purified by column chromatography (EtOAc:Hexane 0-70%, elutes at 30%) to yield a red solid. Yield: 5.30 g (67%).

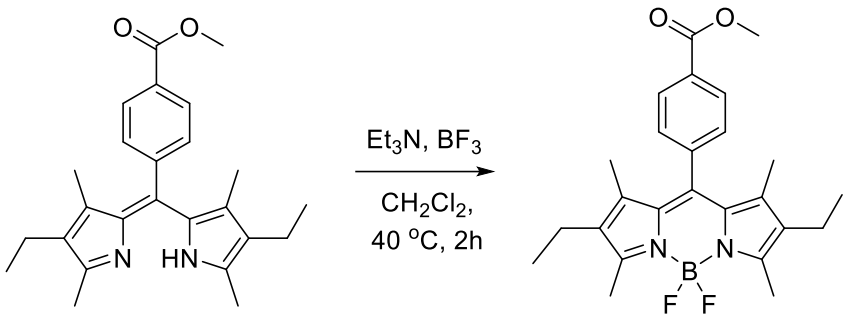

3 4

Methyl 4-(4,4-difluoro-1,3,5,7-tetramethyl-3a,4a-diaza-4-bora-*s*-indacen-8-yl)benzoate (4). The dipyrromethene **(4**, 5.00 g, 12.8 mmol, 1 eq.) was dissolved in anhydrous CH_2Cl_2 and freshly distilled Et_3N (8.92 mL, 64 mmol, 5 eq.) was added under argon. After stirring for 30 min at room temperature $BF_3{\cdot}Et_2O$ (16.2 mL, 128 mmol, 10 eq.) was added dropwise via syringe. The reaction mixture was then stirred at 40 °C until TLC showed complete conversion (~2 h). The reaction was cooled to room temperature and quenched with water. The CH_2Cl_2 layer was washed repeatedly with water (3×100ml), saturated sodium bicarbonate (1×100 ml), and brine then dried with sodium sulfate, filtered, and evaporated under vacuum. The crude material was dry loaded on silica and purified by column chromatography (EtOAc:Hexane 0-100%) and the product fractions were combined, evaporated under vacuum, and recrystallized from MeOH to give (**4**) as large red crystals. Yield: 3.28 g (59%). ^{1}H NMR (500 MHz, $CDCl_3$): δ 8.17 (d, J = 8.2 Hz, 2H), 7.40 (d,

J = 8.0 Hz, 2H), 3.98 (s, 3H), 2.53 (s, 6H), 2.30 (q, *J* = 7.5 Hz, 4H), 1.27 (s, 6H), 0.98 (t, *J* = 7.5 Hz, 6H) ppm. ESI-MS(+) *m*/*z* calculated for: $[C_{25}H_{29}BF_2N_2O_2+H]^+$: 439.24, found: 439.35.

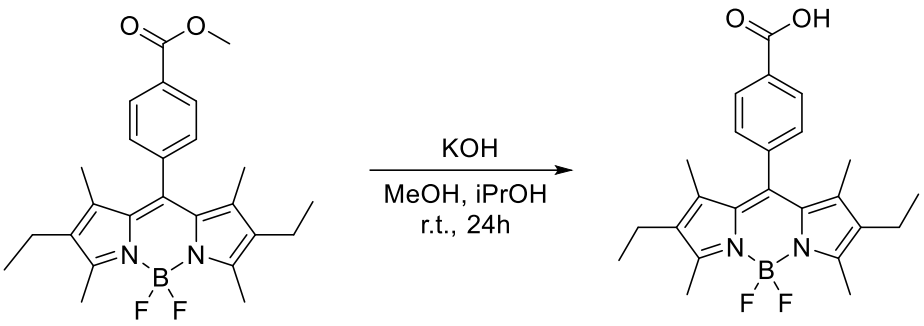

4 **BODIPY$_{COOH}$ 5**

4-(4,4-Difluoro-1,3,5,7-tetramethyl-3a,4a-diaza-4-bora-*s*-indacen-8-yl)benzoic acid (5). BODIPY$_{COOMe}$ **(4)** (500 mg, 1.14 mmol, 1 eq.) was first dissolved in minimal THF. After complete dissolution 50 mL of iPrOH was added and fully mixed. An aqueous solution of KOH (256 mg, 4.56 mmol, 4 eq.) dissolved in 50 mL of water was added. The suspension was monitored until TLC confirmed disappearance of the starting material. The reaction mixture was then concentrated under vacuum to remove iPrOH and the mixture was acidified by the addition of 0.1 M HCl until a pH of 3 was reached. The water layer was evaporated under vacuum and the crude product was purified by column chromatography (EtOAc-Hexane 0-100%, then DCM-MeOH 0-3%). Yield: 447 mg (92%). ^{1}H NMR (500 MHz, $CDCl_3$): δ 8.24 (d, *J* = 8.0 Hz, 2H), 7.45 (d, *J* = 8.1 Hz, 2H), 2.54 (s, 6H), 2.30 (q, *J* = 7.5 Hz, 4H), 1.27 (s, 6H), 0.98 (t, *J* = 7.5 Hz, 6H). ESI-MS(-) *m*/*z* calculated for: $[C_{24}H_{27}BF_2N_2O_2-H]^-$: 423.21, found: 423.23.

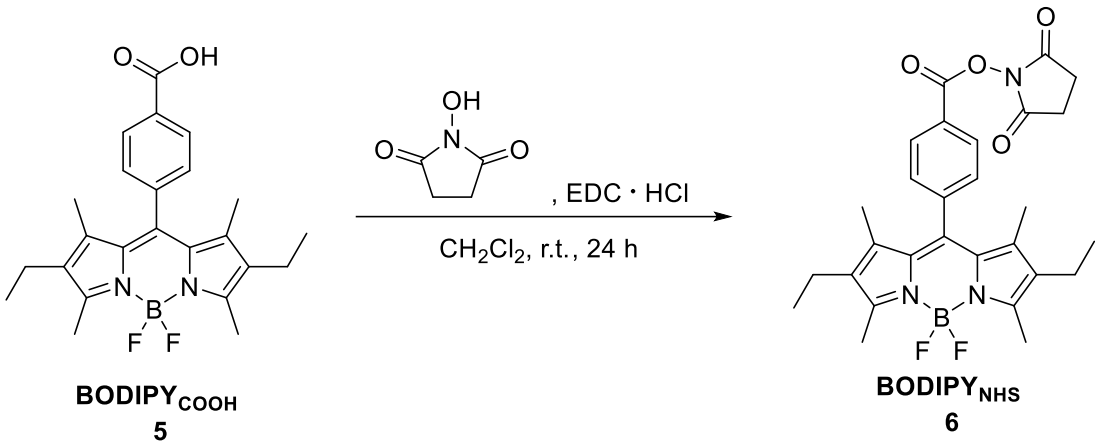

2,5-Dioxopyrrolidin-1-yl 4-(2,8-diethyl-5,5-difluoro-1,3,7,9-tetramethyl-5H-5H-4λ^4,5λ^4-dipyrrolo[1,2-c:2',1'-f][1,3,2]diazaborinin-10-yl)benzoate (BODIPY$_{NHS}$ 6).

A 25 mL round bottom was charged with BODIPY$_{COOH}$ (150 mg, 1 eq., 0.35 mmol), *N*-hydroxysuccinimide (122 mg, 3 eq., 1.06 mmol) and 50 mL of CH_2Cl_2 and cooled to 0 °C in an ice bath. 1-(3-Dimethylaminopropyl)-3-ethylcarbodiimide hydrochloride (136 mg, 2.0 eq., 0.71 mmol) was added and the reaction was left to stir overnight at room temperature. The reaction poured into a separatory funnel and washed with water (2x, 50 mL), brine (50 mL), dried with Na_2SO_4, filtered, and dry loaded onto silica. The crude product was purified by column chromatography (EtOAc-hexane 0-50%) to yield an orange-red solid. Yield: 154 mg (83%). ^{1}H NMR (500 MHz, $CDCl_3$): δ 8.26 (d, J = 8.3 Hz, 2H), 7.49 (d, J = 8.3 Hz, 2H), 2.95 (s, 4H), 2.53 (s, 6H), 2.30 (q, J = 7.6 Hz, 4H), 1.27 (s, 6H), 0.98 (t, J = 7.6 Hz, 6H). ESI-MS(+) *m*/*z* calculated for: $[C_{28}H_{30}BF_2N_3O_4 + H]^+$: 522.23, found: 522.29.

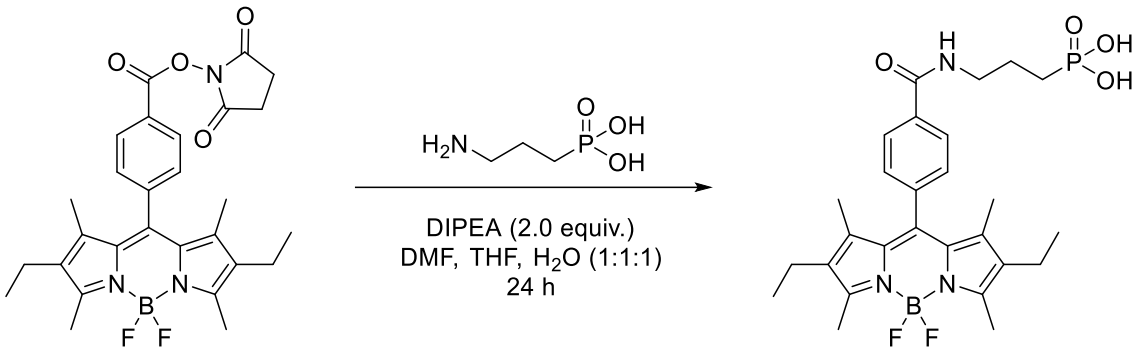

BODIPY$_{NHS}$
6

BODIPY$_{PHOS}$
7

(3-(4-(2,8-Diethyl-5,5-difluoro-1,3,7,9-tetramethyl-5H-5H-4λ^4,5λ^4-dipyrrolo[1,2-c:2',1'-f][1,3,2]diazaborinin-10-yl)benzamido)propyl)phosphonic acid (BODIPY$_{PHOS}$ 7). A 25 mL round bottom was charged with BODIPY$_{NHS}$ (6) (37 mg, 1 eq., 71 µmol) and dissolved in 2 mL of dry DMF and 2 mL of THF and cooled to 0 °C in an ice bath. Separately, 3-aminopropylphosphonic acid (15 mg. 1.5 eq., 0.11 mmol) was dissolved in 2 mL of water and DIPEA (25 µL, 2.0 eq., 0.14 mmol) was added. After briefly mixing, the aqueous solution was added dropwise to the DMF/THF solution via syringe and left to stir for 24 h at room temperature. To purify the ligated dye, the reaction was first concentrated under rotary evaporation, then dried under high vacuum with heating at 40 °C for several hours. The residue was then dissolved in DMF, filtered through a plug of celite to remove salts, and purified by reverse phase column chromatography (ACN:H_2O 0.1% formic acid, 20-100%, elutes at 58%) to give the phosphonate dye as a red powder upon removal of solvent. Yield: 33 mg (85%). ^{1}H NMR (500 MHz, DMSO-D_6): δ 8.76 (s, 1H), 8.01 (d, J = 6.9 Hz, 2H), 7.43 (d, J = 8.1 Hz, 2H), 3.30 (d, J = 6.5 Hz, 2H), 2.40 (s, 6H), 2.24 (q, J = 7.8 Hz, 4H), 1.78 – 1.67 (m, 2H), 1.61 – 1.51 (m, 2H), 1.20 (d, J = 2.2 Hz, 6H), 0.89 (t, J = 2.1 Hz, 6H). ^{31}P NMR (202 MHz, DMSO-D_6): δ 26.98. ESI-MS(+) *m/z* calculated for: $[C_{27}H_{35}BF_2N_3O_4P+H]^+$: 546.25, found: 546.25.

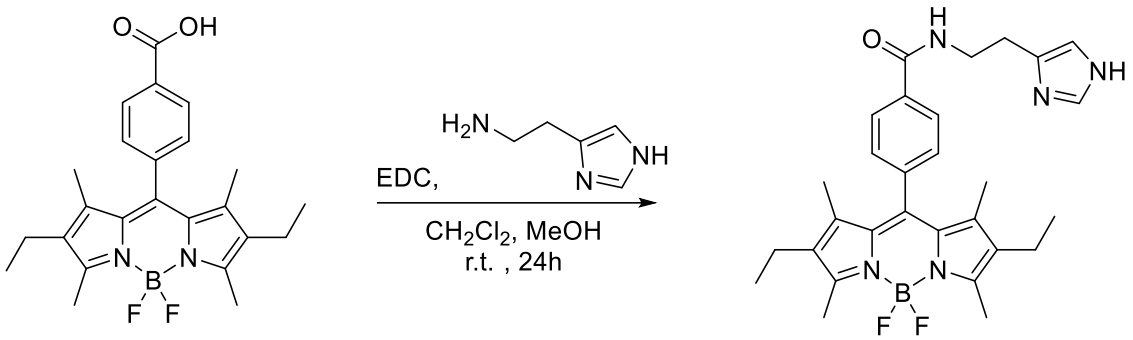

$BODIPY_{COOH}$
5

$BODIPY_{Im}$
6

***N*-(2-(1H-Imidazol-4-yl)ethyl)-4-(2,8-diethyl-5,5-difluoro-1,3,7,9-tetramethyl-5H-4λ^4,5 λ^4-dipyrrolo[1,2-c:2',1'-f][1,3,2]diazaborinin-10-yl)benzamide ($BODIPY_{Im}$ 8).** $BODIPY_{COOH}$ (**5**, 20 mg, 0.15 mmol, 1 eq.) was dissolved in 1 mL CH_2Cl_2. Histamine (15 mg, 0.30 mmol, 2 eq.) was dissolved in 500 µL MeOH and added to the CH_2Cl_2 solution, after which EDC (22 mg, 0.30 mmol, 2 eq.) was added and the reaction was left to stir overnight. The reaction mixture was diluted with CH_2Cl_2, dry loaded on silica, and purified by column chromatography (CH_2Cl_2:MeOH 0-6%). Yield: 12 mg (64%). ^{1}H NMR (500 MHz, Methanol-D_4) δ 7.94 (d, J = 8.3 Hz, 2H), 7.59 (s, 1H), 7.35 (d, J = 8.3 Hz, 2H), 6.85 (s, 1H), 3.62 (t, J = 7.3 Hz, 2H), 2.90 (t, J = 7.3 Hz, 2H), 2.47 (s, 6H), 2.26 (q, J = 7.5 Hz, 4H), 1.23 (s, 6H), 0.94 (t, J = 7.6 Hz, 6H). ESI-MS(+) *m*/*z* calculated for: $[C_{29}H_{34}BF_2N_5O+H]^+$: 518.43, found: 518.46.

MOF Synthesis

UiO-66. UiO-66 was prepared using a continuous addition method as previously reported (*Angew. Chem. Int. Ed.* **2018**, *57*, 7836-7840). The synthesis of UiO-66_x (x = the particle edge length in nm measured by SEM) at 5 L scale was carried out at 120 °C under atmospheric pressure in DMF using formic acid as a modulator. Two separate 30 mM stock solutions were prepared in 5 L jars. The terephthalic acid (H_2bdc) solution was prepared using 22.5 g of H_2bdc, 4.05 L of DMF, and

450 mL of formic acid, while the $ZrOCl_2 \cdot 8H_2O$ was prepared using 45 g of $ZrOCl_2 \cdot 8H_2O$ in 4.5 L of DMF. The reaction procedure was as follows: 100 mL of the $ZrOCl_2 \cdot 8H_2O$ solution was added to a 5 L round bottom flask at 120 °C, followed by both the $ZrOCl_2 \cdot 8H_2O$ and H_2bdc stock solution delivered separately by peristaltic pump with a feed rate of 12 mL/min for 5 min. The feed rate was accelerated to 32 mL/min for 55 min. After this first addition, 2.5 L of the reaction solution was removed from the reactor to obtain the first product, UiO-66_{80}. Another 1.5 L of metal stock solution and 1.5 L of ligand stock solution were further added to the remaining reaction mixture at 30 mL/min for 50 min. Then 3 L of reaction mixture was collected form the reactor to obtain the second product, UiO-66_{120}. Finally, 1.55 L of metal stock solution and 1.55 L of ligand stock solution were added into the reactor within 1 h at 25.8 mL/min, and the remaining reaction solution (3.7 L) was collected as the third product UiO-66_{250}. All products were first centrifuged (8000 rpm, 30-60 min) and washed with 40 mL DMF twice, and then solvent exchange was performed with by washing 3 times in 40 mL of MeOH. The MOFs were left suspended in MeOH at ~20 mg/mL until further use. Before any experiment, a fraction of the sample was removed and dried to determine the exact weight percent of the suspended particles. For this study, only the last fraction of UiO-66 particles (UiO-66_{250}) were used. For PXRD and N_2 sorption experiments the samples were dried in vacuum at 120 °C for 24 h. BET surface area: 981 m^2/g.

ZIF-8. ZIF-8 was prepared as previously reported (*J. Am. Chem. Soc.* **2019**, *141*, 51, 20000–20003). Zinc acetate dihydrate (1.50 g, 6.8 mmol) dissolved in 25 mL water was added to 2-methylimidazole (5.30 g, 65 mmol) dissolved in 25 mL of 0.54 mM cetyltrimethylammonium bromide (CTAB) aqueous solution with gentle stirring for 1 min. The mixture turned white after 15 sec and was left undisturbed at room temperature for 2 h. The resulting ZIF-8 particles were collected by centrifugation (fixed-angle rotor, 9,000 rpm, 10 min), washed with 3×40 mL portions

of MeOH. To prevent aggregation, the particles were kept suspended in methanol without drying. BET surface area: 1260 m^2/g.

MIL-88B-NH_2. MIL-88B-NH_2 was prepared as previously reported (*Chem. Sci.* **2020**, *11*, 8433-8437). A 150 mL flask with a stir bar was charged with 640 mg of Pluronic F127 surfactant dissolved in 60 mL of deionized water. Iron(III) chloride hexahydrate (716 mg, 2.6 mmol, 2 eq.) was added and the solution was stirred for 1 h, after which acetic acid (2.4 mL, 42 mmol, 32 eq.) was added. After stirring 1 h, 2-aminoterephthalic acid (240 mg, 1.3 mmol, 1 eq.) was added and the suspension was stirred for 2 h. The reaction mixture was transferred to a 100 mL autoclave and placed in a preheated oven at 110 °C oven for 24 h. The solution was cooled to room temperature and the dark brown particles were washed through repeated dispersion/centrifugation cycles with ethanol (4×30 mL, 30 min) and DMF (2×30 mL, 30 min) and left suspended in DMF to prevent particle aggregation. BET surface area: 13 m^2/g. The low surface area of MIL-88B-NH_2 is a result of the flexibility of this framework, which is in the closed form when dry (*Cryst. Growth Des.* **2013**, *13*, 2286-2291).

Dye Functionalization of MOF Particles

UiO-66 with BODIPY$_{COOH}$. A 100 mL round bottom flask was charged with a stir bar, 400 mg UiO-66, and 50 mL of DMF. Under rapid stirring, 10 mL of a 1 mg/mL solution of BODIPY$_{COOH}$ dissolved in DMF was added dropwise to the UiO-66 suspension and the solution was left to stir for 24 h. The particles were collected by centrifugation (10,000 rpm, 10 min) and washed with acetone (1×80 mL) by repeated centrifugation and resuspension steps (10,000 rpm, 10 min) and left suspended in 80 mL acetone at a concentration of 5 mg/mL for the next experiments.

Functionalization of MIL-88B-NH_2 with $BODIPY_{COOH}$. A 100 mL round bottom flask was charged with a stir bar, 400 mg of MIL-88B-NH_2 and 50 mL of DMF. Under rapid stirring, 10 mL of a 1 mg/mL solution of $BODIPY_{COOH}$ dissolved in DMF was added dropwise to the MIL-88B-NH_2 suspension and the solution was left to stir for 24 h. The particles were collected by centrifugation (10,000 rpm, 10 min.) and washed with acetone by repeated centrifugation and resuspension steps (40 mL, 10,000 rpm, 10 min) and left suspended in 80 mL acetone at a concentration of 5 mg/mL for the next experiments.

Functionalization of ZIF-8 with $BODIPY_{Im}$. A 100 mL round bottom flask was charged with stir bar, 400 mg ZIF-8, and 40 mL of DMF. Under rapid stirring, 25 mg of $BODIPY_{Im}$ was added to the ZIF-8 suspension and the solution was left to stir for 24 h. The particles were collected by centrifugation (10,000 rpm, 10 min.) and washed with acetone (1x80 mL) by repeated centrifugation and resuspension steps (10,000 rpm, 10 min) and left suspended in 80 mL acetone at a concentration of 5 mg/mL for the next experiments.

Solvent Stability

1.7 mL Eppendorf tubes were charged with 1 mL of solvent and 0.2 mL of a 5 mg/mL suspension of BODIPY-functionalized MOF particles in acetone. Separate tubes were made for each time point: t = 0, 1 h, 24 h. After the specified waiting time, tubes were centrifuged at 13,000 RPM for 10 min and the supernatant was removed for UV-visible spectroscopy. Each time point was performed in triplicate.

Competitive Binding

Stock solutions were prepared by dissolution of each ligand in acetone and serial dilution. Eppendorf tubes (1.7 mL) were charged with 1 mL of ligand solution and 0.2 mL of a 5 mg/mL suspension of BODIPY-functionalized MOF particles in acetone. Points between serial dilutions were created by adding 0.5 mL of ligand solution and 0.5 mL of acetone or 0.25 mL of ligand solution and 0.75 mL of acetone instead of 1 mL of ligand solution. The tubes were allowed to sit for 24 h, followed by centrifugation at 13,000 RPM for 15 min. The supernatant was removed for UV-visible spectroscopy. Each data point was performed in triplicate.

Curve Fitting and Normalization

The sigmoidal binding curves were fit to the logistic equation using the OriginLab logistic fitting function:

$$y = A_{max} + \frac{A_{min} - A_{max}}{1 + \left(\frac{x}{x_0}\right)^p}$$

A_{max} denotes the maximum absorbance, A_{min} denotes the minimum absorbance, x_0 is the concentration at the center of the curve, and p is the slope. To normalize the curves for visualization, the maximum and minimum values were set to 1 and 0, respectively, while keeping x_0 and p the same.

Supporting Figures and Tables

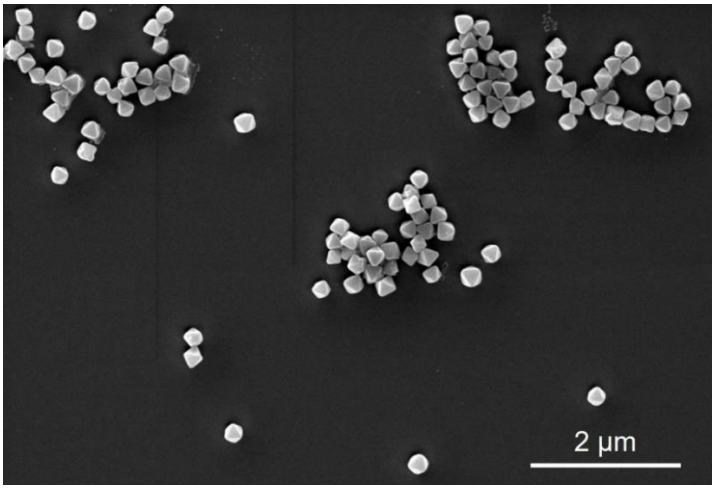

Figure 4S.1. Scanning electron microscopy (SEM) images of UiO-66 particles. The average edge length measured by SEM was 220 nm.

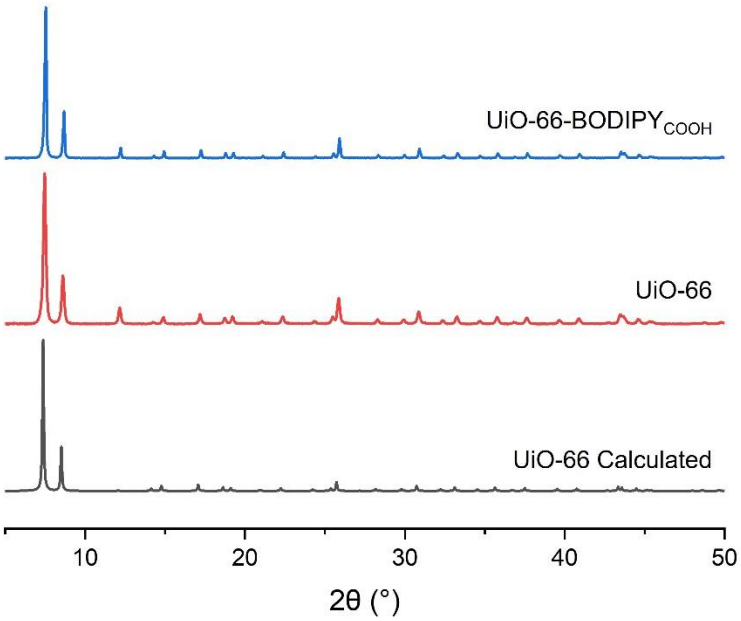

Figure 4S.2. Powder X-ray diffraction (PXRD) of UiO-66 before and after functionalization with BODIPY$_{COOH}$.

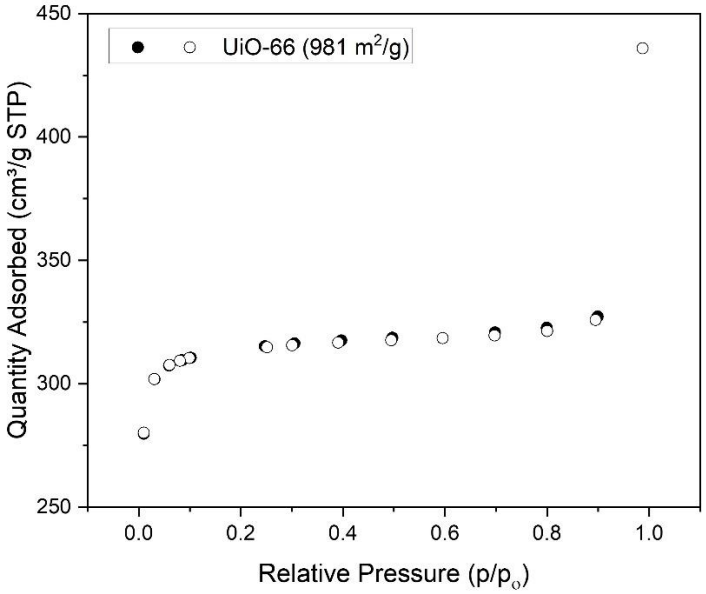

Figure 4S.3. N_2 sorption isotherm for UiO-66 with respective BET surface area.

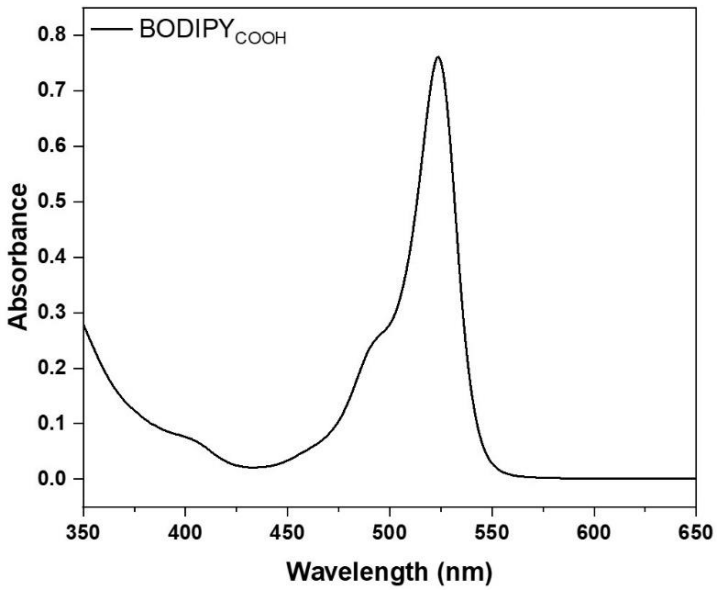

Figure 4S.4. UV-visible spectrum of $BODIPY_{COOH}$ in acetone (λ_{max} = 524 nm).

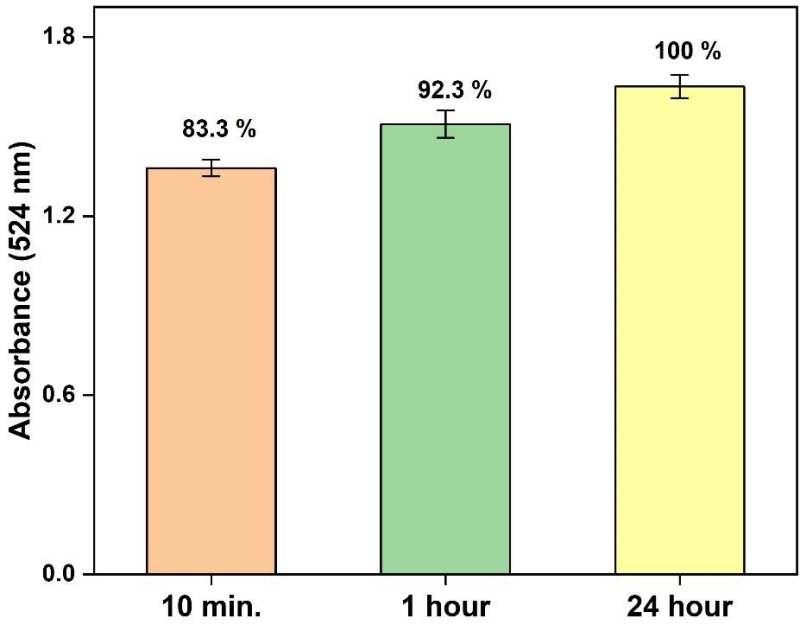

Figure 4S.5. Absorption intensity (524 nm) of the supernatant of digested UiO-66-BODIPY$_{COOH}$ particles isolated at 10 min, 1 h, and 24 h after addition of BODIPY$_{COOH}$. Percentage labels are relative to the absorbance of the 24 h sample representing maximum functionalization.

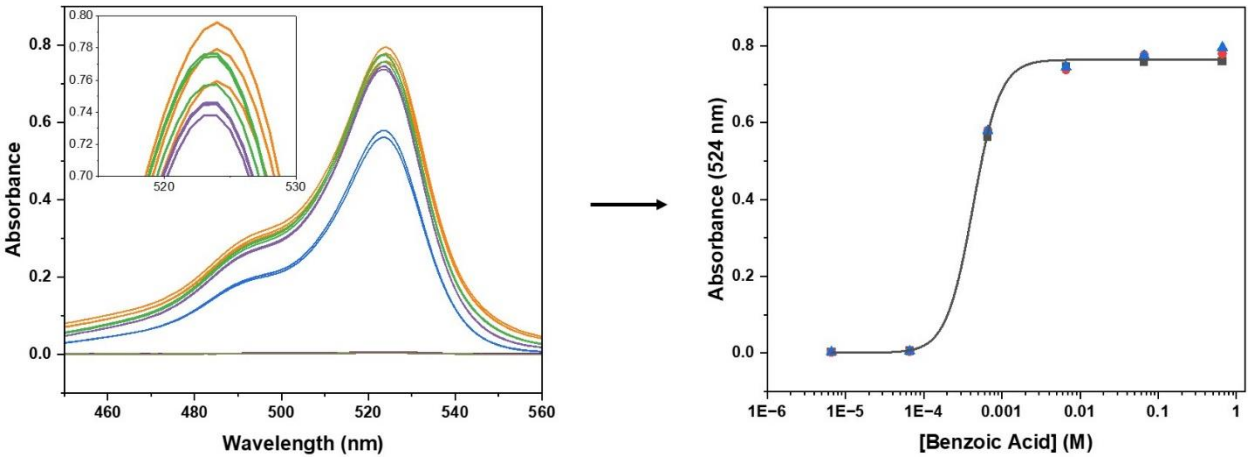

Figure 4S.6. Absorbance (*left*) and sigmoidal curve fitting (*right*) after treating UiO-66-BODIPY$_{COOH}$ with increasing concentrations of benzoic acid (**BA**).

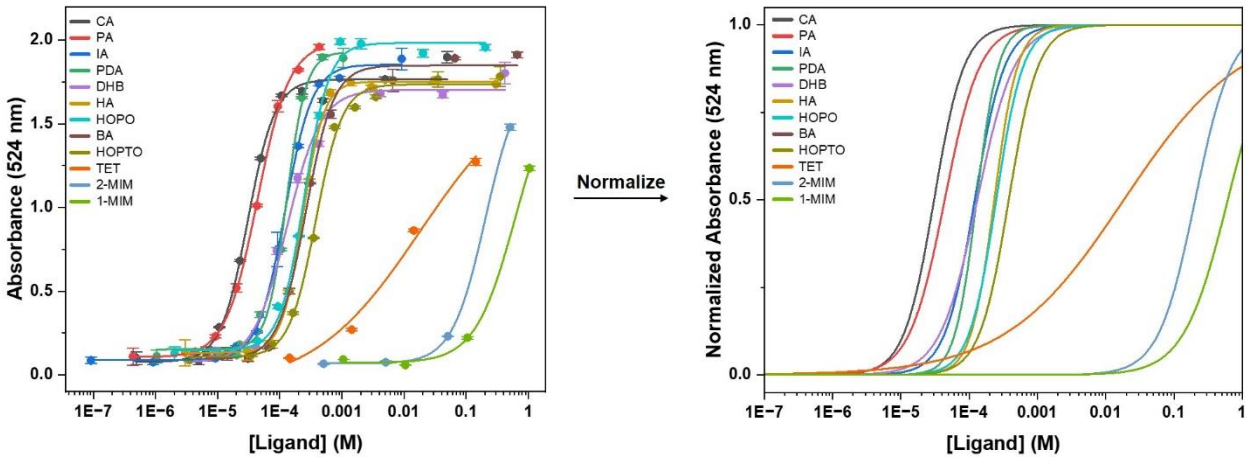

Figure 4S.7. Titration of UiO-66-BODIPY$_{COOH}$ with various ligands. Raw sigmoidal curve fittings with data points (*left*) and normalized curves (*right*).

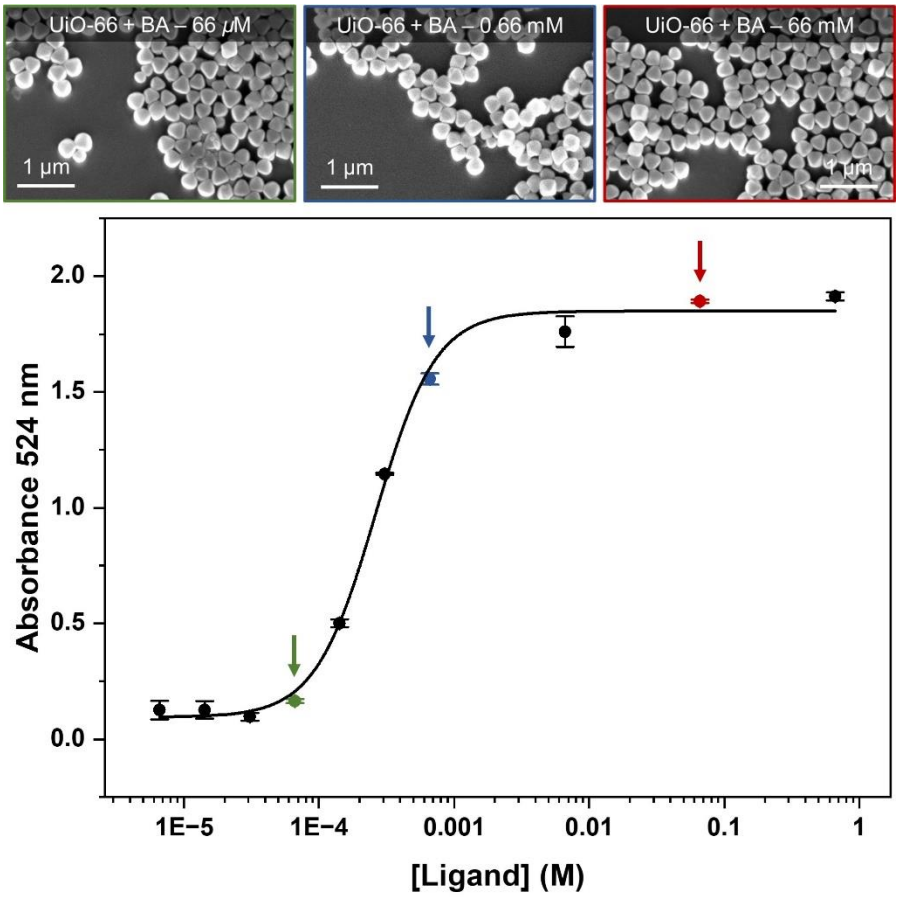

Figure 4S.8. SEM images of UiO-66-BODIPY$_{COOH}$ (*top*) showing no change in particle morphology after titration with benzoic acid (**BA**) at three different concentrations (*bottom*).

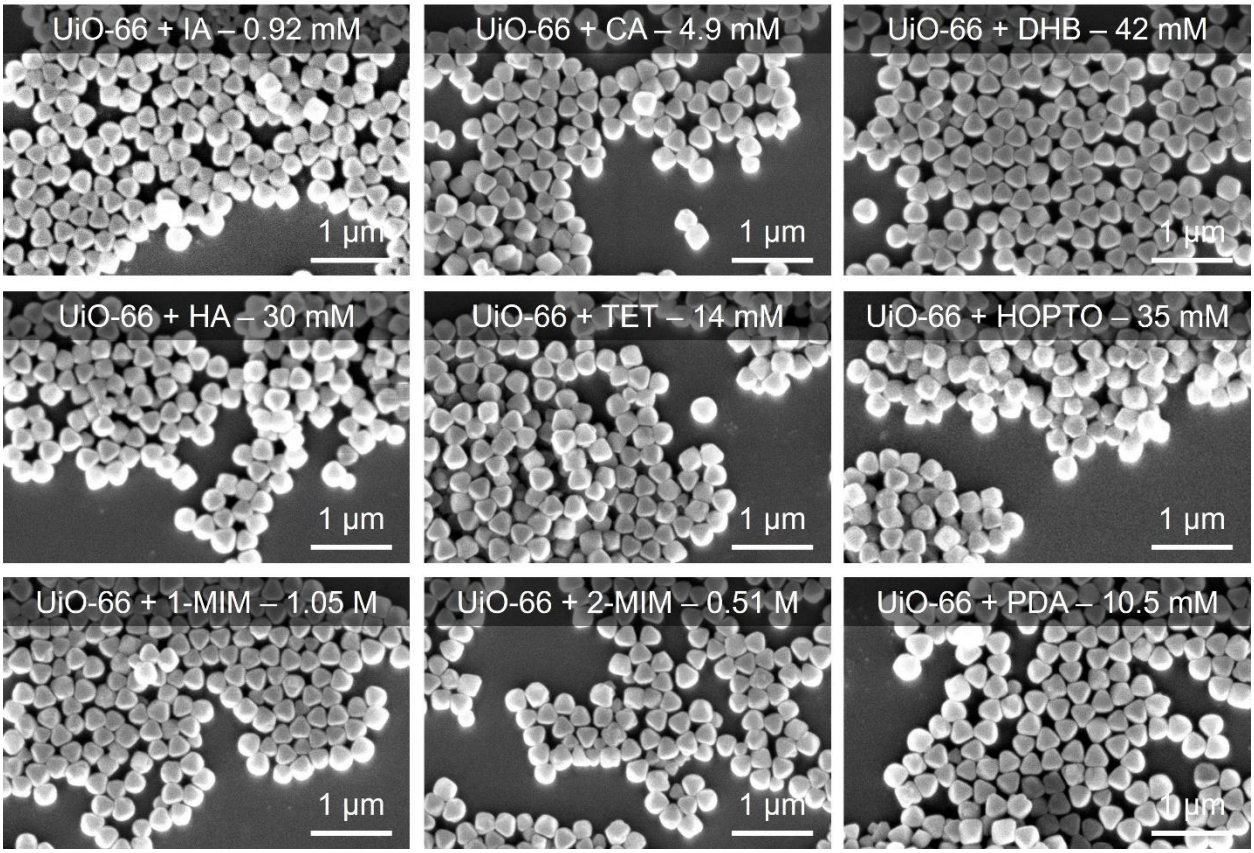

Figure 4S.9. SEM images of UiO-66-BODIPY$_{COOH}$ showing no change in appearance after titration experiments with various ligands. For each ligand, the concentrations listed are above the dye displacement region in Figure 4S.7.

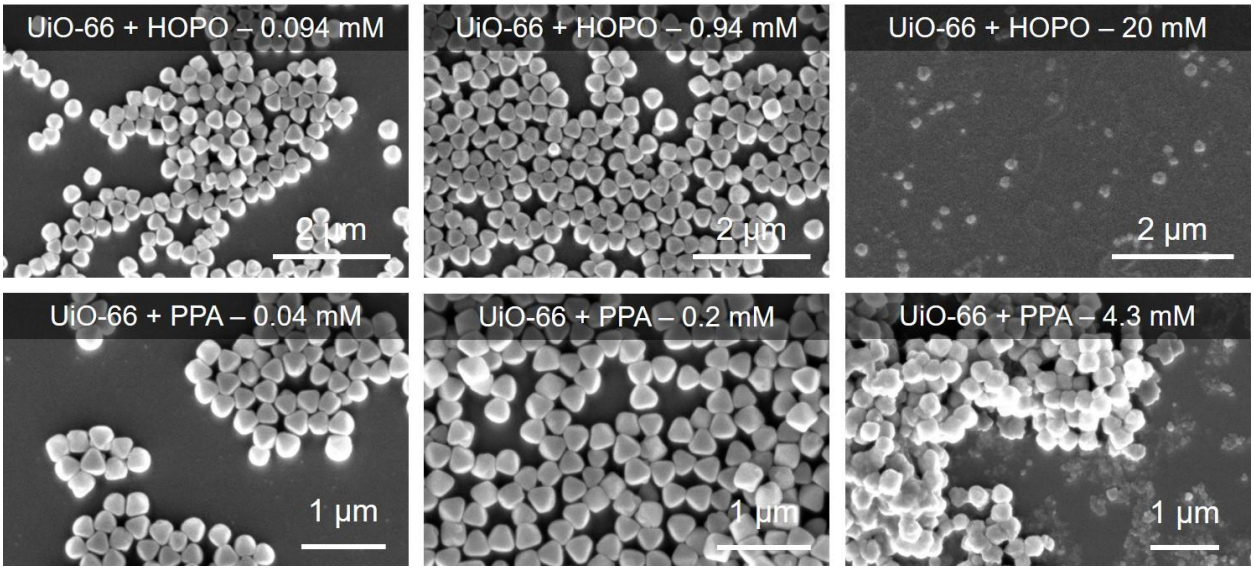

Figure 4S.10. SEM images of UiO-66-BODIPY$_{COOH}$ at various points in the titration with HOPO and PPA showing: particle stability at intermediate dye displacement concentrations of ligand (*left*), concentrations near complete dye displacement (*middle*), and particle degradation at very high concentrations of ligand (*right*). See Figure 4S.7 for highlighted data points along the titration curve.

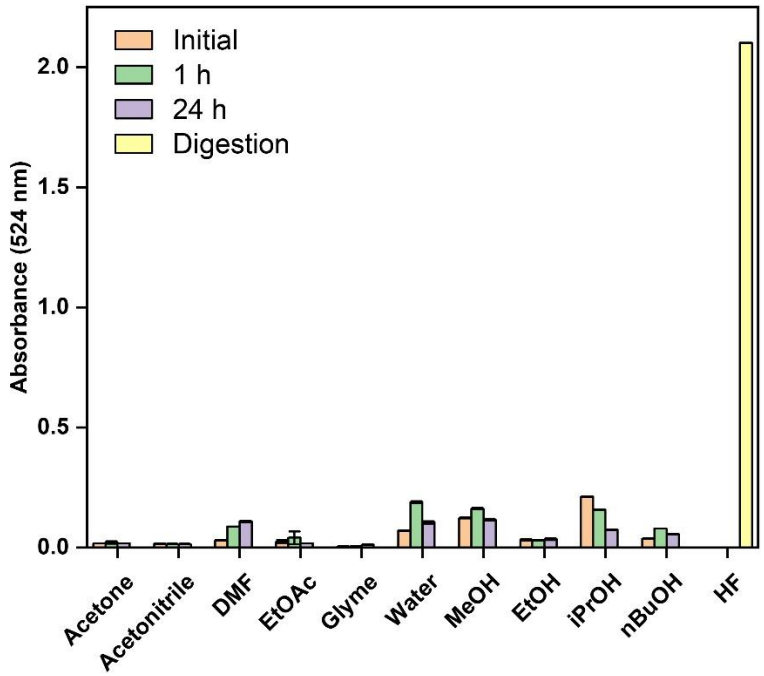

Figure 4S.11. Absorption intensity (524 nm) of the supernatant at three time points from UiO-66-BODIPY$_{PHOS}$ suspended in various solvents.

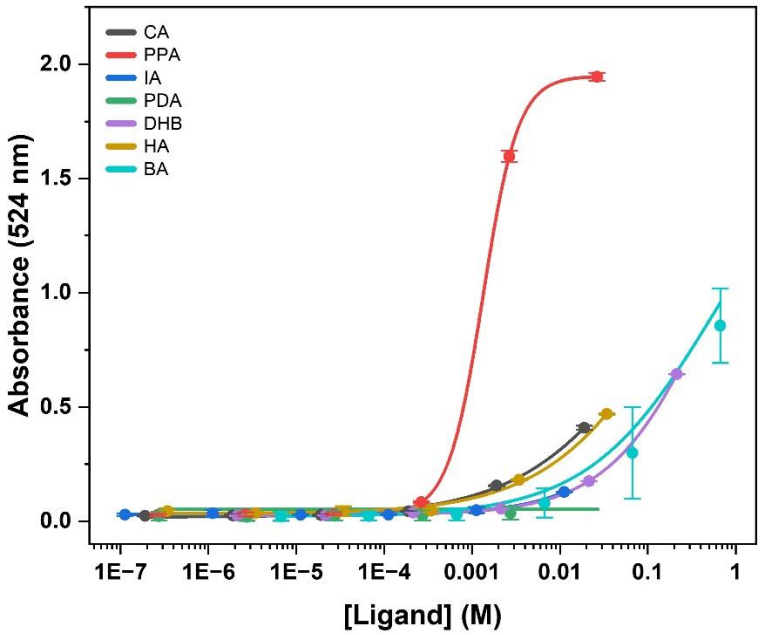

Figure 4S.12. Titration of UiO-66-BODIPY$_{PHOS}$ with select ligands. In the case of **PPA**, the concentrations at which absorbance is detected results in degraded of the UiO-66 particles.

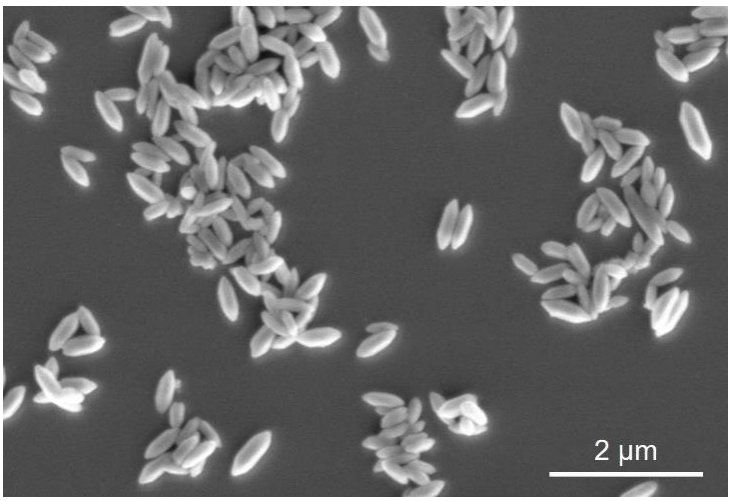

Figure 4S.13. SEM images of MIL-88B-NH_2 particles after synthesis.

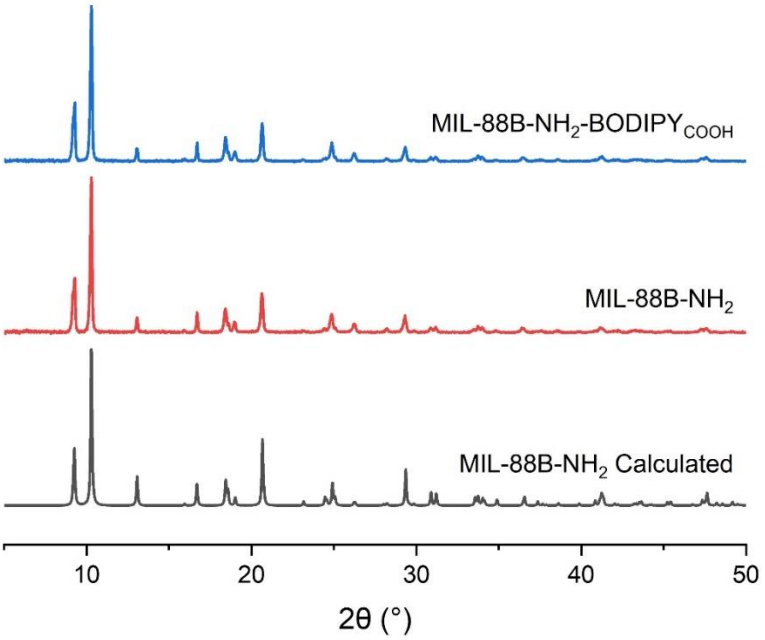

Figure 4S.14. PXRD of MIL-88B-NH_2 before and after functionalization with $BODIPY_{COOH}$.

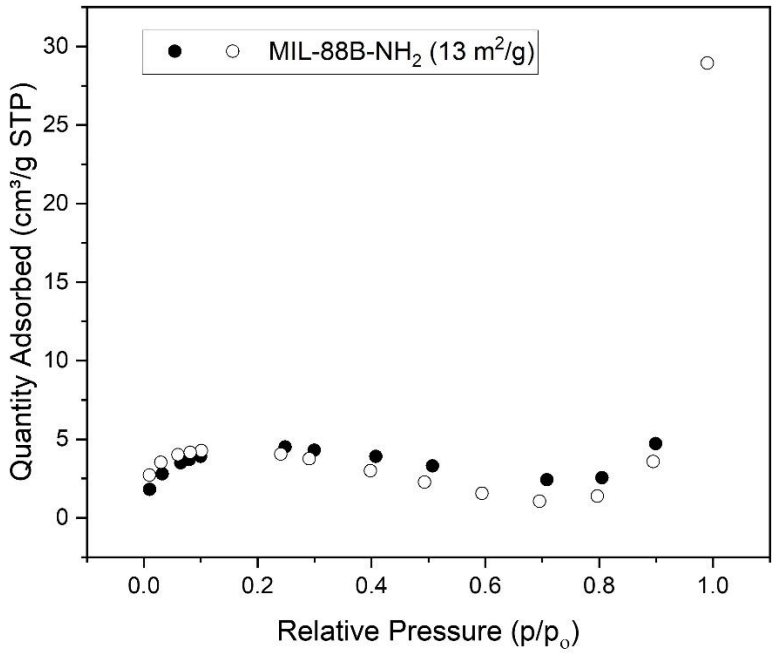

Figure 4S.15. N_2 sorption isotherm for MIL-88B-NH_2 with respective BET surface area.

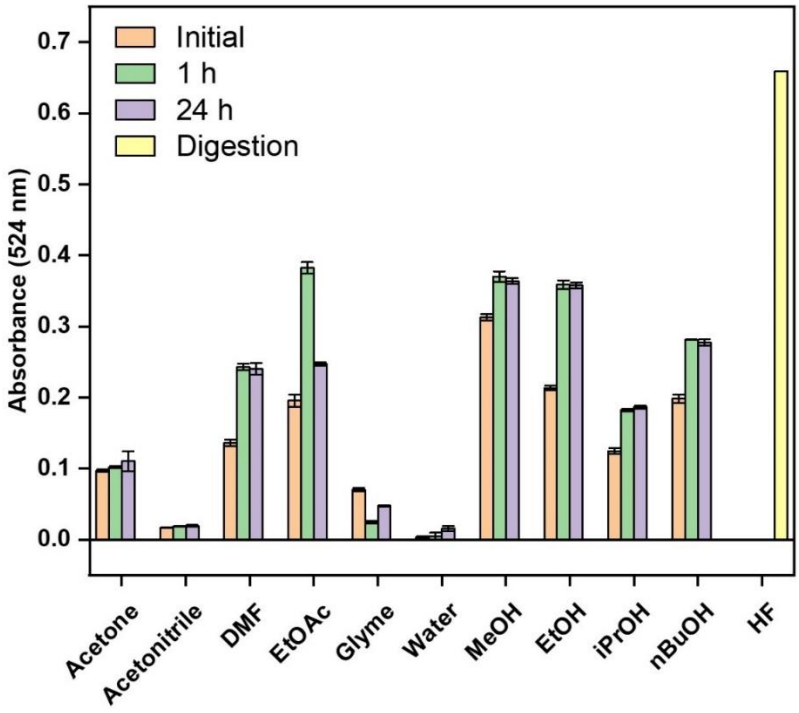

Figure 4S.16. Absorption intensity (524 nm) of the supernatant at three time points from MIL-88B-NH_2-$BODIPY_{COOH}$ suspended in various solvents.

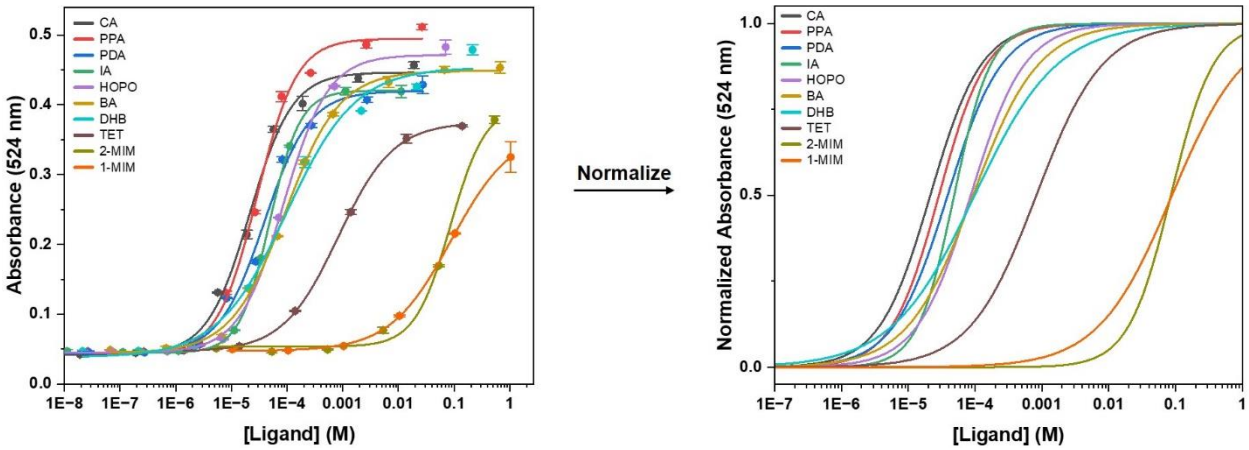

Figure 4S.17. Titration of MIL-88B-NH_2-$BODIPY_{COOH}$ with various ligands. Raw sigmoidal curve fittings with data points (*left*) and normalized curves (*right*).

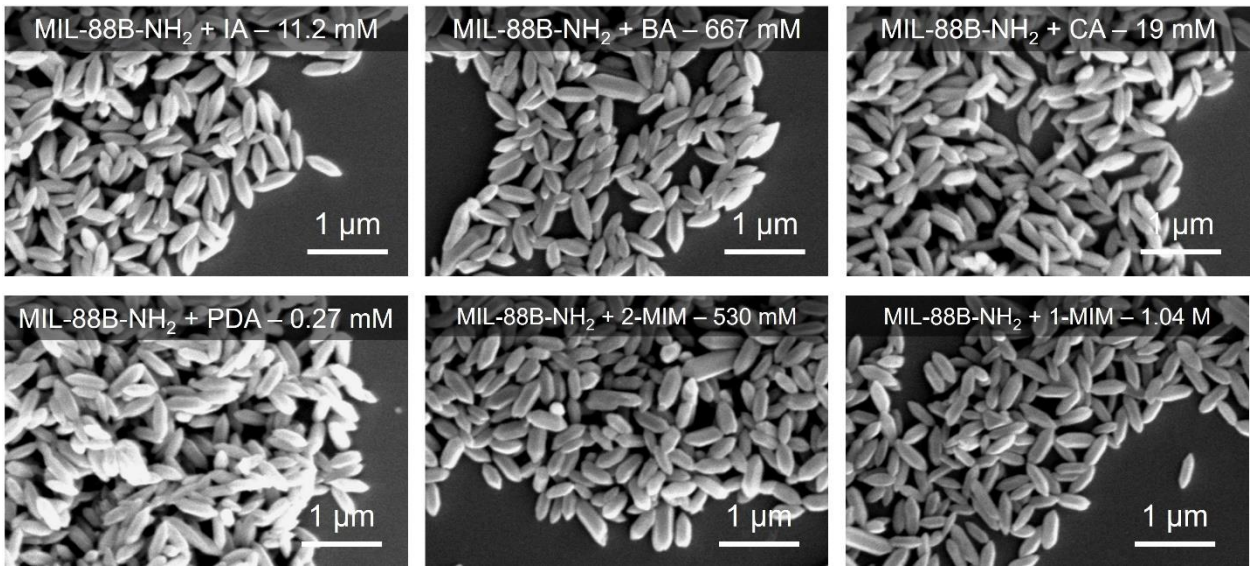

Figure 4S.18. SEM images of MIL-88B-NH_2-$BODIPY_{COOH}$ showing no change in morphology after titration experiments with various ligands. For each ligand, the concentrations listed are above the dye displacement region in Figure 4S.17.

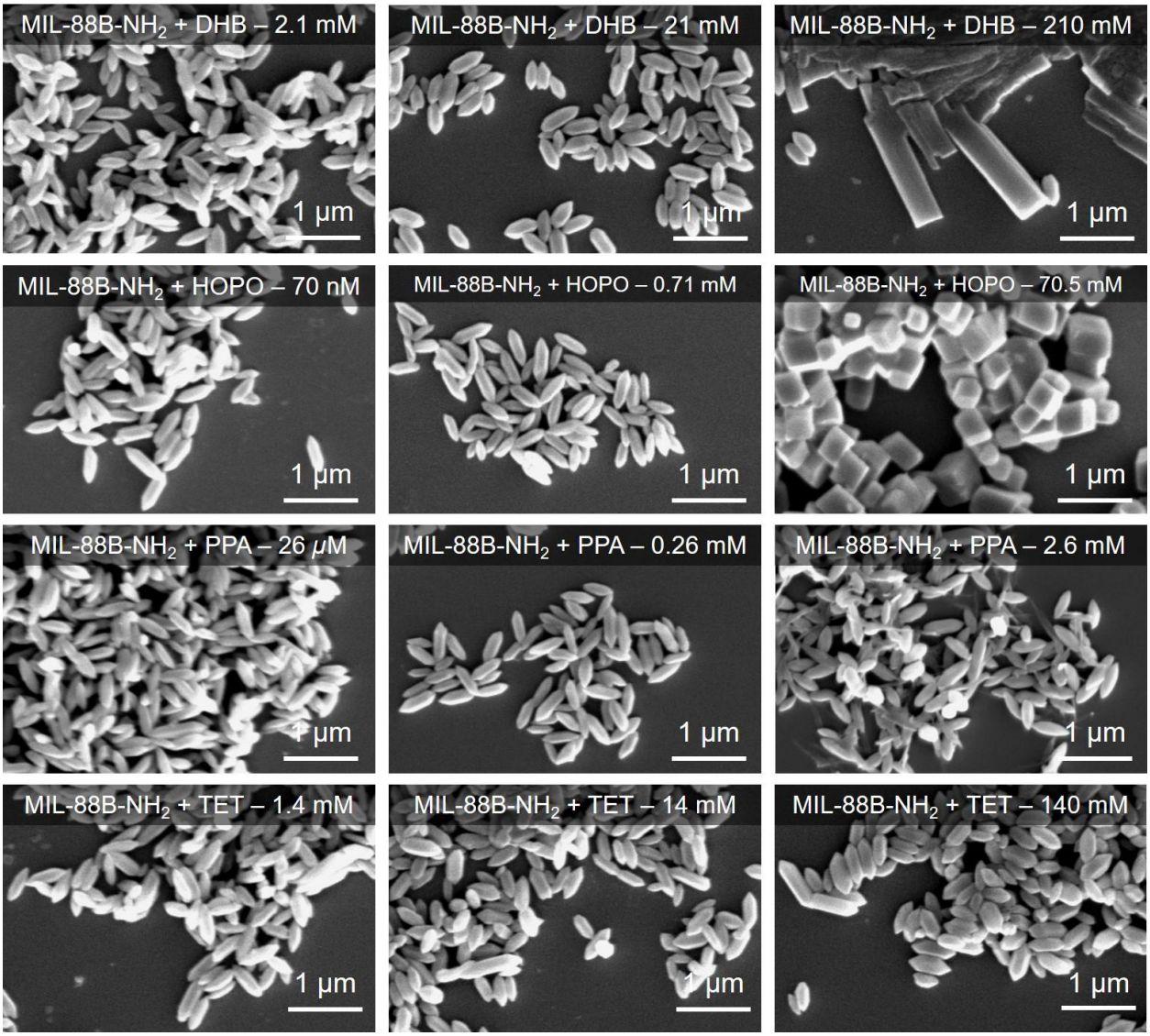

Figure 4S.19. SEM images of MIL-88B-NH_2-$BODIPY_{COOH}$ at various points in the titration with different ligands showing: particle stability at intermediate dye displacement concentrations of ligand (*left*), concentrations near complete dye displacement (*middle*), and particle degradation at very high concentrations of ligand (*right*). See Figure 4S.17 for highlighted data points along the titration curve.

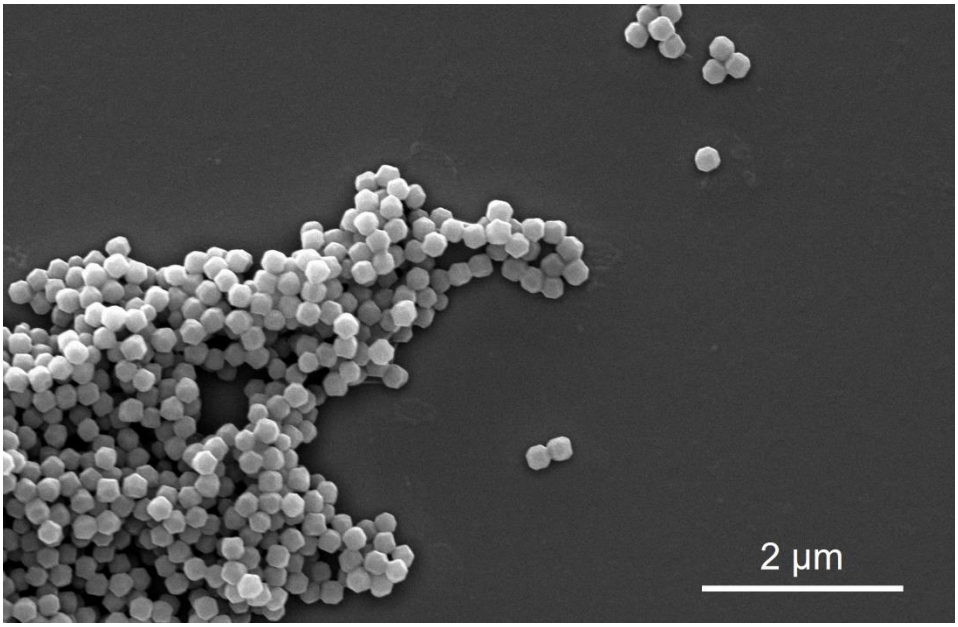

Figure 4S.20. SEM images of ZIF-8 particles after synthesis.

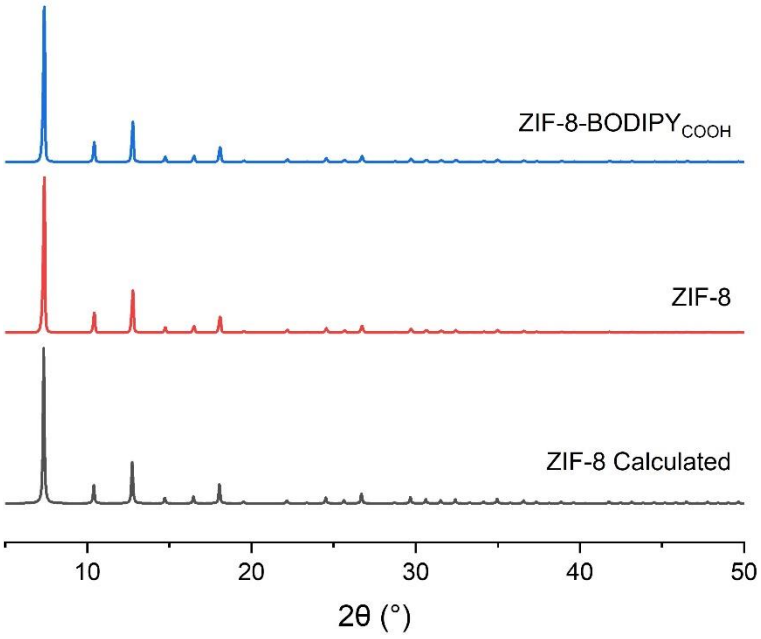

Figure 4S.21. PXRD of ZIF-8 before and after functionalization with BODIPY$_{Im}$.

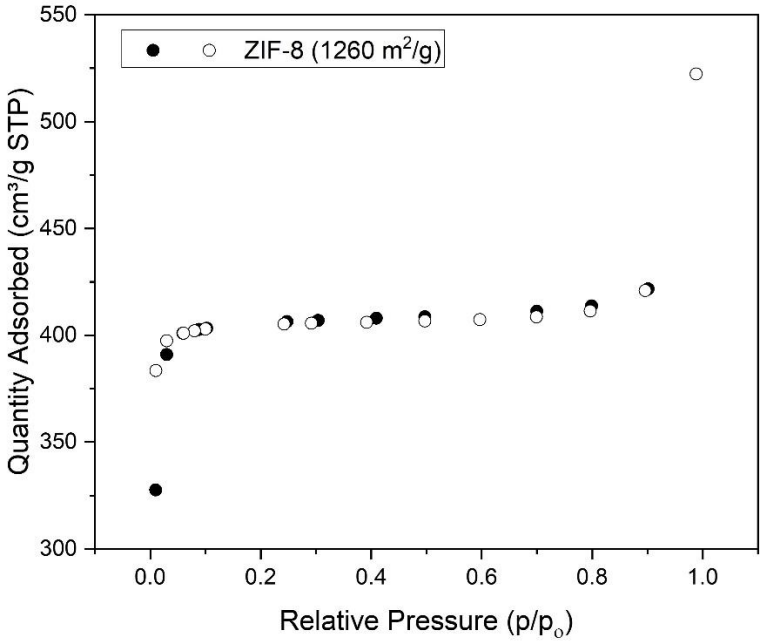

Figure 4S.22. N_2 sorption isotherm for ZIF-8 with respective BET surface area.

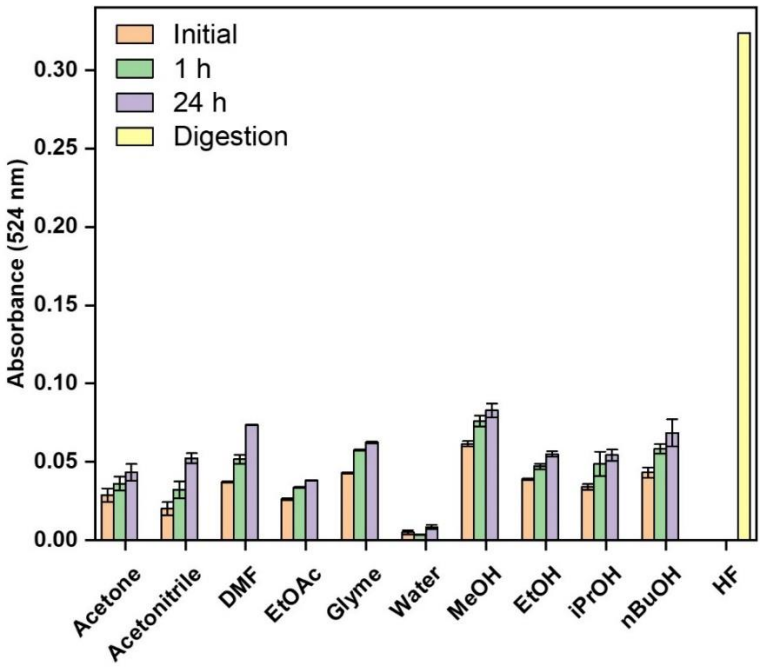

Figure 4S.23. Absorption intensity (524 nm) of supernatant at three time points from ZIF-8-BODIPY$_{Im}$ suspended in various solvents.

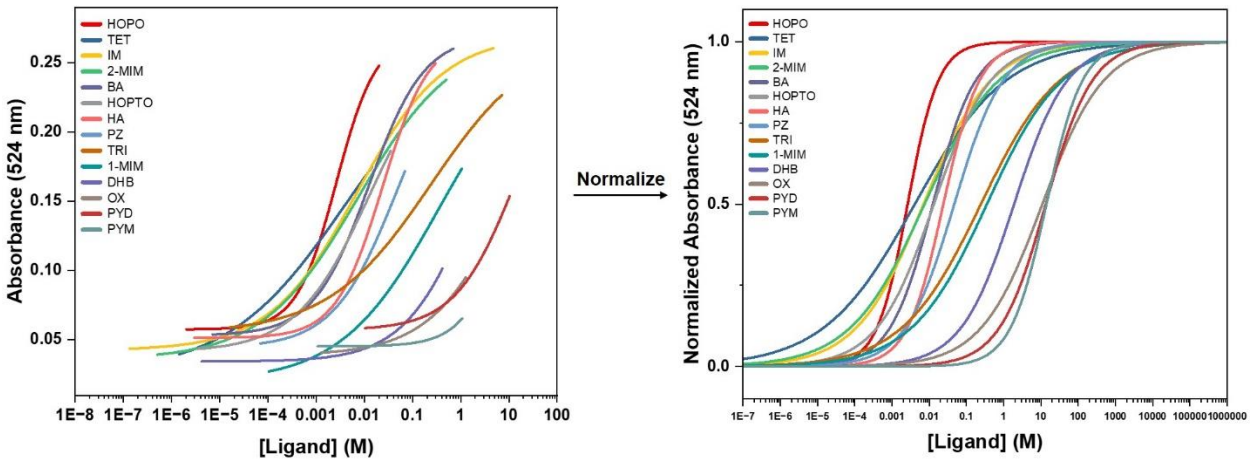

Figure 4S.24. Titration of ZIF-8-BODIPY$_{Im}$ with various ligands. Raw sigmoidal curve fittings with data points (*left*) and normalized curves (*right*).

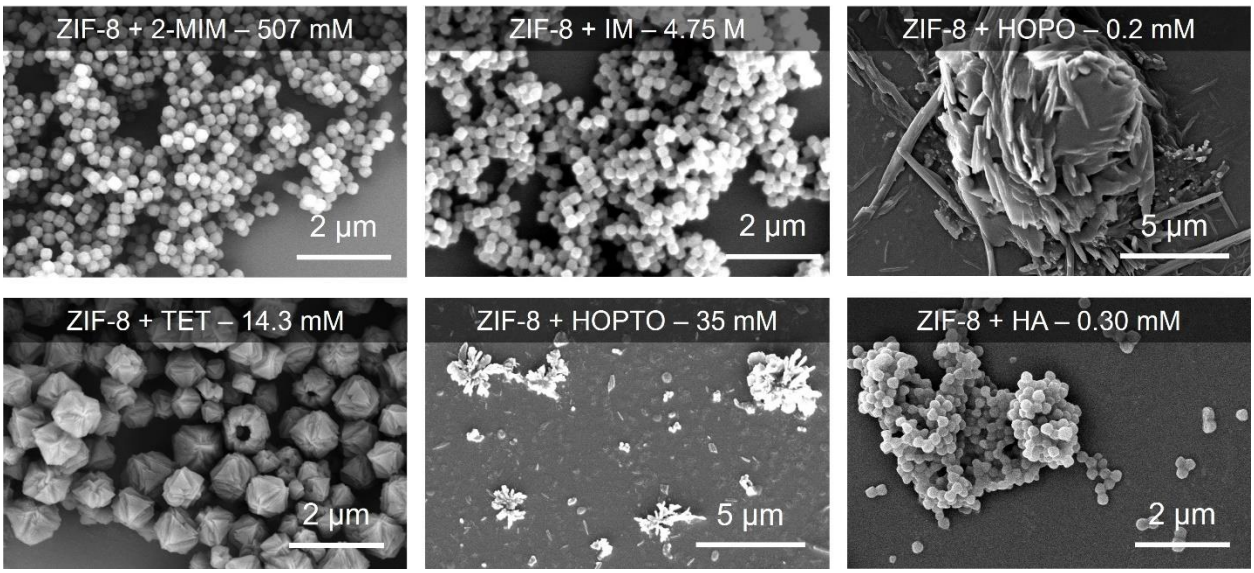

Figure 4S.25. SEM images of ZIF-8 after titration with select ligands showing stability with **2-MIM** and **IM** and degradation with **HOPO**, **TET**, **HOPTO**, and **HA**.

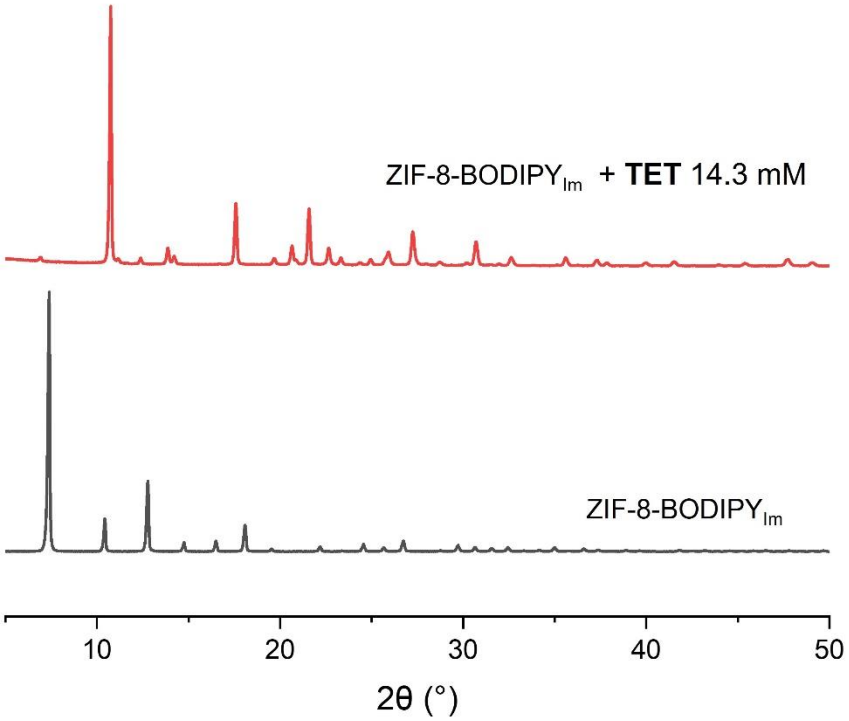

Figure 4S.26. PXRD of ZIF-8-BODIPY$_{Im}$ before and after treatment with 14.3 mM **TET** in acetone.

Table 4S.1. Table showing ligand abbreviation, apparent binding constant (K_{ap}), and error values from Figure S24. Because the titration curves in Figure S24 were largely incomplete, the values listed here should only be considered useful for relative comparison of affinity.

Ligand	K_{ap} (M^{-1})	Error (±)
HOPO	380	54
TET	245	28
IM	143	18
2-MIM	134	16
BA	80	6
HOPTO	75	8
HA	42	7
PZ	21	1
TRI	4.1	0.8
1-MIM	2.8	0.7
DHB	<1	-
OX	<1	-
PYD	<1	-
PYM	<1	-

4.5 Acknowledgements

Chapter 4, in part, has been submitted for publication of the material titled “Quantifying Ligand Binding to the Surface of Metal-Organic Frameworks” as it may appear in *J. Am. Chem. Soc. 2023.* The dissertation author was the primary author of this manuscript and gratefully acknowledges the contributions of coauthors Austin Wang and Seth M. Cohen.

4.6 References

1. Abánades Lázaro, I.; Haddad, S.; Sacca, S.; Orellana-Tavra, C.; Fairen-Jimenez, D.; Forgan, R. S., Selective Surface PEGylation of UiO-66 Nanoparticles for Enhanced Stability, Cell Uptake, and pH-Responsive Drug Delivery. *Chem* **2017,** *2*, 561-578.

2. Chen, X.; Zhuang, Y.; Rampal, N.; Hewitt, R.; Divitini, G.; O'Keefe, C. A.; Liu, X.; Whitaker, D. J.; Wills, J. W.; Jugdaohsingh, R.; Powell, J. J.; Yu, H.; Grey, C. P.; Scherman, O. A.; Fairen-Jimenez, D., Formulation of Metal–Organic Framework-Based Drug Carriers by Controlled Coordination of Methoxy PEG Phosphate: Boosting Colloidal Stability and Redispersibility. *J. Am. Chem. Soc.* **2021,** *143*, 13557-13572.

3. Röder, R.; Preiß, T.; Hirschle, P.; Steinborn, B.; Zimpel, A.; Höhn, M.; Rädler, J. O.; Bein, T.; Wagner, E.; Wuttke, S.; Lächelt, U., Multifunctional Nanoparticles by Coordinative Self-Assembly of His-Tagged Units with Metal–Organic Frameworks. *J. Am. Chem. Soc.* **2017,** *139*, 2359-2368.

4. Wang, S.; Chen, Y.; Wang, S.; Li, P.; Mirkin, C. A.; Farha, O. K., DNA-Functionalized Metal–Organic Framework Nanoparticles for Intracellular Delivery of Proteins. *J. Am. Chem. Soc.* **2019,** *141*, 2215-2219.

5. Wang, S.; McGuirk, C. M.; Ross, M. B.; Wang, S.; Chen, P.; Xing, H.; Liu, Y.; Mirkin, C. A., General and Direct Method for Preparing Oligonucleotide-Functionalized Metal–Organic Framework Nanoparticles. *J. Am. Chem. Soc.* **2017,** *139*, 9827-9830.

6. Suresh, K.; Kalenak, A. P.; Sotuyo, A.; Matzger, A. J., Metal-Organic Framework (MOF) Morphology Control by Design. *Chem. Eur. J.* **2022,** *28*, e202200334.

7. Desai, A. V.; Vornholt, S. M.; Major, L. L.; Ettlinger, R.; Jansen, C.; Rainer, D. N.; de Rome, R.; So, V.; Wheatley, P. S.; Edward, A. K.; Elliott, C. G.; Pramanik, A.; Karmakar, A.; Armstrong, A. R.; Janiak, C.; Smith, T. K.; Morris, R. E., Surface-Functionalized Metal–Organic Frameworks for Binding Coronavirus Proteins. *ACS Appl. Mater. Interfaces* **2023,** *15*, 9058-9065.

8. Sheridan, T. R.; Gaidimas, M. A.; Kramar, B. V.; Goswami, S.; Chen, L. X.; Farha, O. K.; Hupp, J. T., Noncovalent Surface Modification of Metal–Organic Frameworks: Unscrambling Adsorption Properties via Isothermal Titration Calorimetry. *Langmuir* **2022,** *38*, 11199-11209.

9. Spiegel, S.; Wagner, I.; Begum, S.; Schwotzer, M.; Wessely, I.; Bräse, S.; Tsotsalas, M., Dynamic Surface Modification of Metal–Organic Framework Nanoparticles via Alkoxyamine Functional Groups. *Langmuir* **2022,** *38*, 6531-6538.

10. Kondo, M.; Furukawa, S.; Hirai, K.; Kitagawa, S., Coordinatively Immobilized Monolayers on Porous Coordination Polymer Crystals. *Angew. Chem. Int. Ed.* **2010,** *49*, 5327-5330.

11. Wang, S.; Morris, W.; Liu, Y.; McGuirk, C. M.; Zhou, Y.; Hupp, J. T.; Farha, O. K.; Mirkin, C. A., Surface-Specific Functionalization of Nanoscale Metal–Organic Frameworks. *Angew. Chem. Int. Ed.* **2015,** *54*, 14738-14742.

12. Wang, X.-G.; Cheng, Q.; Yu, Y.; Zhang, X.-Z., Controlled Nucleation and Controlled Growth for Size Predicable Synthesis of Nanoscale Metal–Organic Frameworks (MOFs): A General and Scalable Approach. *Angew. Chem. Int. Ed.* **2018,** *57*, 7836-7840.

13. Cheng, J. M. H.; Chee, S. H.; Dölen, Y.; Verdoes, M.; Timmer, M. S. M.; Stocker, B. L., An efficient synthesis of a 6″-BODIPY-α-Galactosylceramide probe for monitoring α-Galactosylceramide uptake by cells. *Carbohydr. Res.* **2019,** *486*, 107840.

14. Marreiros, J.; Caratelli, C.; Hajek, J.; Krajnc, A.; Fleury, G.; Bueken, B.; De Vos, D. E.; Mali, G.; Roeffaers, M. B. J.; Van Speybroeck, V.; Ameloot, R., Active Role of Methanol in Post-Synthetic Linker Exchange in the Metal–Organic Framework UiO-66. *Chem. Mater.* **2019,** *31*, 1359-1369.

15. Chiu, C.-C.; Shieh, F.-K.; Tsai, H.-H. G., Ligand Exchange in the Synthesis of Metal–Organic Frameworks Occurs Through Acid-Catalyzed Associative Substitution. *Inorg. Chem.* **2019,** *58*, 14457-14466.

16. Bellezza, F.; Cipiciani, A.; Quotadamo, M. A., Immobilization of Myoglobin on Phosphate and Phosphonate Grafted-Zirconia Nanoparticles. *Langmuir* **2005,** *21*, 11099-11104.

17. Pham, M.-H.; Vuong, G.-T.; Vu, A.-T.; Do, T.-O., Novel Route to Size-Controlled Fe–MIL-88B–NH2 Metal–Organic Framework Nanocrystals. *Langmuir* **2011,** *27*, 15261-15267.